# Durham E-Theses

## *Temperature and strain scaling laws for the critical current density in Nb(_3)Sn and Nb(_3)Al conductors in high magnetic fields*

Keys, Simon Alastair

**How to cite:**

Keys, Simon Alastair (2001) *Temperature and strain scaling laws for the critical current density in Nb(_3)Sn and Nb(_3)Al conductors in high magnetic fields*, Durham theses, Durham University. Available at Durham E-Theses Online: http://etheses.dur.ac.uk/3951/

# Temperature and strain scaling laws for the critical current density in Nb$_3$Sn and Nb$_3$Al conductors in high magnetic fields

## Simon Alastair Keys

A thesis submitted in partial fulfilment of the requirements for the degree of Doctor of Philosophy

# Temperature and strain scaling laws for the critical current density in Nb₃Sn and Nb₃Al conductors in high magnetic fields

## Simon Alastair Keys

## Abstract

Detailed, accurate measurements of critical current density and resistivity to determine the upper critical field have been made on a technological Nb₃Al conductor in magnetic fields up to 15 T, temperatures from 4.2 K up to the critical temperature and in the strain range from -1.8% to 0.7%. The uncertainty in temperature above 4.2 K was equivalent to ± 100 mK with a stability during the measurements of < 5 mK up to a limiting current of 80 A and a typical noise level of 1 $\mu Vm^{-1}$.

When $B_{C2}(T,\varepsilon)$ is defined at 5%$\rho_N$, 50%$\rho_N$ or 95%$\rho_N$, an empirical relation is found where $B_{C2}^{\rho_N}(T,\varepsilon) = B_{C2}^{\rho_N}(0,\varepsilon)\left[1-\left(T/T_C^{\rho_N}(\varepsilon)\right)^{\nu}\right]$ and an approximate relation, $B_{C2}^{\rho_N}(0,\varepsilon) = 3.60 \times T_C^{\rho_N}(\varepsilon) - 29.86$, holds. The $J_E$ data were parameterised using $F_P = J_E B = A(\varepsilon)\left[B_{C2}\right]^n b^p (1-b)^q$ where $b = B/B_{C2}(T,\varepsilon)$. When $B_{C2}(T,\varepsilon)$ is constrained to be the value at 50%$\rho_N$ or 95%$\rho_N$, the scaling law for $F_P$ breaks down such that $p$ and $q$ are strong functions of temperature and $q$ is also a strong function of strain. However, when $B_{C2}(T,\varepsilon)$ is defined at 5%$\rho_N$, there is good scaling where $p$ and $q$ are constants – independent of temperature and strain. $F_P$ can also be approximated by a Kramer form $F_P = \frac{1}{249}\frac{\left[B_{C2}(T,\varepsilon)\right]^{\frac{5}{2}}}{(2\pi\Phi_0)^{\frac{1}{2}}\mu_0\kappa^2(T,\varepsilon)}b^{\frac{1}{2}}(1-b)^2$, where the Ginzburg-Landau constant is $\kappa(T,\varepsilon) = 924\frac{B_{C2}(T,\varepsilon)}{\gamma^{\frac{1}{2}}(\varepsilon)T_C(\varepsilon)(1-t^2)} \approx \kappa(T_C,\varepsilon)\frac{2}{\nu}\frac{(1-t^\nu)}{(1-t^2)}$, $\gamma$ is the electronic density of states and $t = T/T_C(\varepsilon)$. $B_{C2}^{5\%\rho_N}$ is interpreted as the average $B_{C2}$ for the bulk where percolative current flow occurs.

The critical current density of Hot Isostatic Pressed (HIP'ed) and unHIP'ed Nb₃Sn Modified Jelly Roll wires has also been measured at 4.2 K. The critical current and upper critical field were decreased for the HIP'ed sample. The reduced upper critical field of the HIP'ed wire was found to be less sensitive to strain than the unHIP'ed wire. The exponent of $B_{C2}$ in the flux pinning scaling law increased from 0.86 to 2.14 as a result of the HIP processing.

# Declaration and Copyright

I hereby declare that the work contained within this thesis is my own original work and nothing that is the result of collaboration unless otherwise stated. No part of this thesis has been submitted for a degree or other qualification at this or any other university.

The copyright of this thesis rests with the author. No quotation from it should be published without their prior written consent and information derived from it should be acknowledged.

S. A. Keys
September 2001.

# Acknowledgements

# Contents

# Variables

| | |
|---|---|
| $\mathbf{A}$ | vector potential |
| $A_{cs}$ | cross sectional area |
| $A$ | prefactor in Fietz-Webb scaling law |
| $A^*$ | prefactor in technological parameterisation of $Nb_3Al$ data |
| $a$ | constant in the strain scaling law |
| $\alpha_{GL}$ | constant in Ginzburg-Landau equation |
| $\alpha$ | constant in power law description of a $E$-$J$ transition equation |
| | |
| $B$, $\mathbf{B}$ | magnetic field |
| $B_C$ | thermodynamic critical field |
| $B_{C1}$ | lower critical field |
| $B_{C2}$ | upper critical field |
| $B_{C2}^{\rho}$ | upper critical field obtained by resistivity measurement |
| $B_{C2}^*$ | upper critical field in technological parameterisation of $Nb_3Al$ data |
| $B_{C2}^{Kramer}$ | upper critical field obtained from Kramer analysis |
| $B_{C2M}^{Kramer}$ | maximum upper critical field obtained from Kramer analysis as a function of strain |
| $B_e$ | external magnetic field |
| $B_i$ | internal magnetic field |
| $b$ | reduced magnetic field |
| $\beta_{GL}$ | constant in Ginzburg-Landau equation |
| $\beta$ | variation coefficient in the numerical analysis of $J_C$ data |
| | |
| $c_{0\to4}$ | polynomial constants in technological parameterisation of $Nb_3Al$ data |
| $C$ | prefactor in Fietz-Webb scaling law |
| $C_M$ | maximum value of the prefactor, $C$ |
| | |
| $d$ | diameter |
| $\Delta$ | superconducting energy gap |

| $E$, $\mathbf{E}$ | electric field strength |
| --- | --- |
| $E_0$ | constant in exponential description of $E\text{-}J$ transition |
| $E_C$ | electric field criterion |
| $e$ | charge on an electron |
| $e_S$ | charge on a superelectron |
| $\varepsilon$ | strain |
| $\varepsilon_I$ | intrinsic strain |
| $\varepsilon_M$ | strain at which critical parameters ($J_C$, $T_C$ and $B_{C2}$) are maximum |
| | |
| $F_L$ | Lorentz force per unit length |
| $F_P$ | volume pinning force |
| $F_{PM}$ | maximum pinning force |
| $f_n$ | free energy of normal state |
| $f_S$ | free energy of superconducting state |
| | |
| $G$ | prefactor in the unified temperature-strain scaling law |
| $\gamma$ | electronic density of states (Sommerfeld constant) |
| | |
| $h$ | Planck's constant |
| | |
| $I$, $\mathbf{I}$ | current |
| $I_C$ | critical current |
| $I_{CM}$ | maximum critical current |
| | |
| $J$, $\mathbf{J}$ | current density |
| $J_0$, $J_I$ | constants in the exponential description of a $E\text{-}J$ transition |
| $J_C$ | critical current density (for the superconductor alone) |
| $J_E$, $J_C^E$ | engineering critical current density |
| $J_{C(Non\text{-}Cu)}$ | critical current density for area of strand that is not matrix material |
| | |
| $\kappa$ | Ginzburg-Landau parameter |

| | |
|---|---|
| $L$ | length |
| $\lambda$ | penetration depth |
| $\lambda_L$ | London penetration depth |
| | |
| $m$ | strain index in Fietz-Webb $F_P$ scaling law |
| $M$ | atomic mass |
| $m_e$ | mass of an electron |
| $m_S$ | mass of a superelectron |
| $\mu_0$ | permeability of free space |
| | |
| $n$ | temperature index in Fietz-Webb $F_P$ scaling law |
| $N$ | index of transition (from power law description of a $E$-$J$ transition) |
| $n_S$ | number density of superelectrons |
| $\nu$ | reduced temperature exponent in upper critical field scaling law |
| | |
| $\phi_0$ | quantum of magnetic flux |
| | |
| $p$ | reduced field exponent in Fietz-Webb scaling law |
| $P_C$ | power criterion |
| | |
| $q$ | reduced field exponent in Fietz-Webb scaling law |
| $Q$ | heat load |
| | |
| $\rho$ | resistivity |
| $\rho_m$ | matrix resistivity |
| $\rho_N$ | normal state resistivity |
| $\rho_C$ | resistivity criterion |
| $\rho_{ff}$ | flux flow resistivity |

| | |
|---|---|
| $t$ | time |
| $t$ | reduced temperature |
| $T$ | temperature |
| $T_0$ | temperature of thermometer in zero magnetic field |
| $T_C$ | critical temperature |
| $T_C^\rho$ | critical temperature obtained from the resistivity measurement |
| $T_C^*$ | critical temperature in technological parameterisation of the Nb$_3$Al data |
| | |
| $\theta$ | angular displacement |
| | |
| $u$ | exponent of strain in the strain scaling law |
| | |
| $V$ | voltage |
| | |
| $\xi$ | coherence length |
| $\xi_0$ | BCS coherence length |
| | |
| $\Psi(\mathbf{r})$ | Ginzburg Landau order parameter |

# Chapter 1

# Introduction

Superconductivity is an exciting area of physics. As well as exhibiting many interesting phenomena, the fundamental properties of zero electrical resistance and perfect diamagnetism mean that superconductors have a wide range of potential technological use. Such applications range from superconducting electronics to magnetic energy storage and levitation. This potential has been realised in superconducting magnet systems. The ability of a superconducting wire to carry resistance free current up to a maximum value, the critical current density ($J_C$), allows the fabrication of high field magnets that achieve high stability with low power consumption. Magnetic Resonance Imaging (MRI) and Nuclear Magnetic Resonance (NMR) are two established examples of superconducting magnet technology.

At the present moment in time, $Nb_3Sn$ and $Nb_3Al$ multifilamentary strands are essential for high field applications above 12 T. It is known that voids are present in the microstructure of $Nb_3Sn$ and $Nb_3Al$ strands, and have been shown to be deleterious to strand performance. High-pressure reactions such as Hot Isostatic Pressing (HIP'ing) have been used on other superconducting materials to close up the voids and improve their properties, and have also previously been successfully used on $Nb_3Sn$.

To optimise the engineering of high field magnet systems, $J_C$ must be known as a function of magnetic field, temperature, and strain. The strands operate under strain due to Lorentz forces during the energising of such coils and the differential thermal contraction between component parts of the conductor on cooling to cryogenic temperatures. Recently introduced technology such as cryocoolers and cable-in-conduit conductor systems that are cooled by the forced flow of liquid helium along the length of the conductor mean that the strands operate over a range of temperatures.

In order to obtain a complete description of $J_C$, the determining mechanism must be identified. The mechanism is still unknown for $Nb_3Sn$ and $Nb_3Al$, but semi-empirical

scaling laws with different forms have been successfully used to model the data. There is also a correlation in the data fitting procedure due to the number of free parameters involved. Accurate measurements of $J_C$ across as wide a range of magnetic field, temperature and strain phase space are required so that these inconsistencies can be resolved.

This thesis studies the dependence of $J_C$ on magnetic field, temperature and strain for state-of-the-art commercial $Nb_3Sn$ and $Nb_3Al$ conductors and is structured as follows. Chapter 2 presents an introduction to superconductivity and a historical development of some of the fundamental theories used to describe it. A review of experimental techniques necessary for accurate $J_C$ measurements is presented in chapter 3. Methods of analysing the data are also discussed along with case studies for current technological materials and specialist measurement techniques.

Chapters 4 and 5 detail the experimental work performed. An investigation into whether the strain tolerance of $J_C$ in optimised $Nb_3Sn$ strands can be further improved by HIP'ing is presented in chapter 4. These measurements are preliminary but yield an interesting result that requires further exploration. Chapter 5 presents comprehensive $J_C$ measurements on a $Nb_3Al$ strand as a function of magnetic field, temperature and strain. Improvements to the existing probe are described that allow data to be measured over a broader experimental range. Complementary measurements have also been performed in order to break the correlation in fitting the $J_C$ data. These $J_C$ data have been analysed in terms of the semi-empirical scaling laws, and one unified scaling law is proposed to describe the mechanism of $J_C$ in these $Nb_3Al$ strands. The results of this analysis are then discussed with reference to a technological parameterisation of the data. Finally, some suggestions for future work are presented in chapter 6.

# Chapter 2

# Introduction to Superconductivity

## 2.1 Introduction

This chapter presents an introduction to superconductivity, and gives a historical development of some of the fundamental theories used to describe it. In sections 2.2 to 2.5, the basic features of superconductivity will be described. This will detail how superconductivity was discovered in section 2.2. The intrinsic properties, i.e. zero resistance and the Meissner effect, will be presented in section 2.3 and the associated critical parameters in section 2.4. Finally, the different types of superconductivity (type I and type II) will be discussed in section 2.5.

Sections 2.6 and 2.7 will present the two phenomenological theories of superconductivity, namely London theory and Ginzburg Landau theory. The flux line lattice as predicted by Ginzburg-Landau theory is introduced in section 2.8. The microscopic theory of superconductivity, BCS theory, is finally presented in section 2.9. An overview of the fundamental results and parameters generated by these theories is given in the relevant sections.

## 2.2 Discovery of superconductivity

In 1908 H. Kamerlingh Onnes successfully liquefied helium [1]. Subsequently in 1911, he observed that the dc electrical resistance of mercury discontinuously dropped to zero when the temperature was reduced below 4.15 K [2]. The resulting state was later named the superconducting state. A year later, it was shown that the application of a sufficiently large magnetic field could destroy the superconductivity.
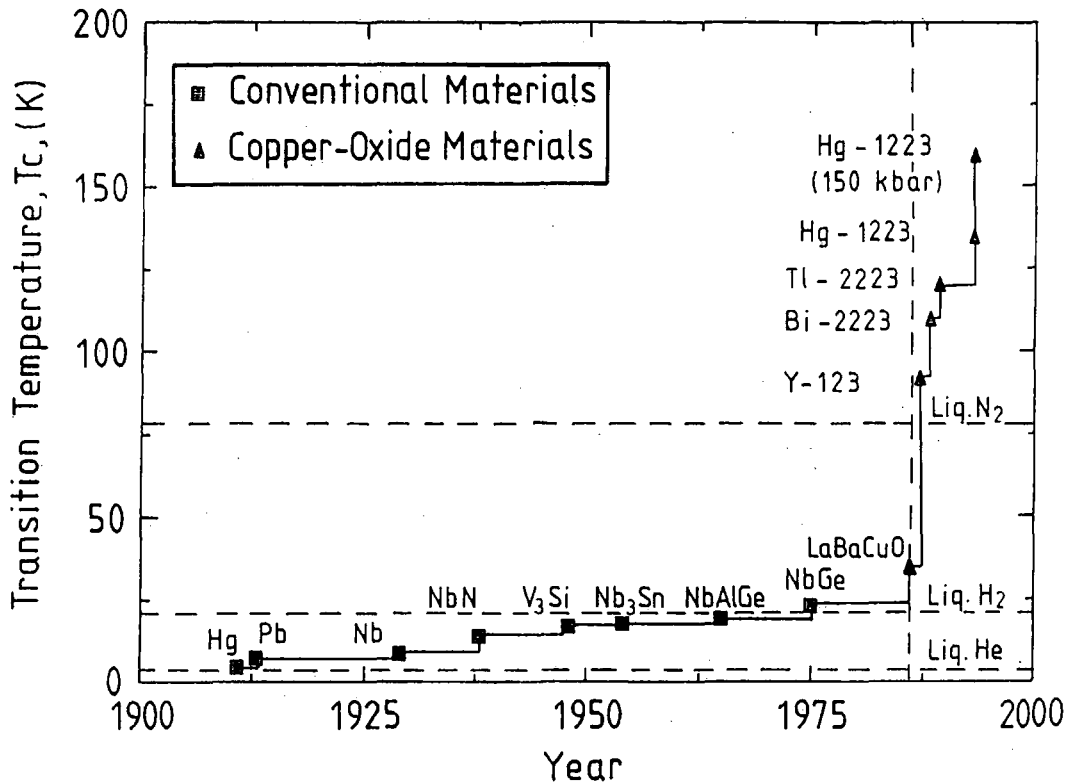
**Figure 2.1** The chronological development of superconducting materials (data from [3]).

After this initial discovery, many elements and compounds have been shown to be superconducting. Figure 2.1 shows the chronological development of some superconducting materials. An important landmark was in 1987, when $YBa_2Cu_3O_{7-\delta}$ (YBCO) was discovered [4]. This compound becomes superconducting at approximately 95 K and so can be used in liquid nitrogen.

## 2.3 Intrinsic properties

Superconducting materials have two fundamental properties. The first of these is *zero resistance*. Here the dc electrical resistance of the material drops to zero when its temperature drops below the critical temperature, $T_C$. Experiments on persistent currents in superconducting rings have estimated the decay times for such currents to be at least $10^5$ years. This places an upper limit on the resistivity of a superconductor to be

of order $10^{-24}$ $\Omega$cm, which is at least 11 orders of magnitude smaller than that of copper [5].

The second fundamental property is *perfect diamagnetism*. This was discovered in 1933 by Meissner and Oschenfeld [6]. If a superconductor is placed in a magnetic field, the field is excluded from entering the superconductor. Although this can be explained by perfect conductivity, when a material in its normal state in a small magnetic field is cooled below $T_C$ there is complete expulsion of flux (Meissner effect) which cannot be explained by perfect conductivity.

## 2.4    Critical parameters

Superconductors have three critical parameters. As described above, there is the critical temperature, $T_C$, above which all superconductivity is destroyed. Secondly there is a critical field ($B_C$ for type I superconductors and $B_{C2}$ for type II superconductors). The material must be in a magnetic field lower than this value for it to be superconducting. Finally, the maximum amount of current that can flow in a superconductor is the critical current density, $J_C$.

## 2.5    Type I and type II superconductors

There are two types of superconductor, type I and type II. The two types can be described by considering a superconductor at a temperature below $T_C$ in an increasing magnetic field so that it goes through its transition from superconducting state to the normal state.

Type I superconductors exclude magnetic flux completely (i.e. are in the Meissner state) up to the thermodynamic critical field, $B_C$. For fields above $B_C$ magnetic flux completely penetrates the sample. The sample is completely in its normal state, its resistance returns, and the internal field is the same as the external field (i.e. its magnetic moment is zero). $B_C$ is related to the free-energy difference between the normal and superconducting states in zero field. Most elemental superconductors are type I superconductors. (Notable exceptions are Nb, V and Mo which are all type II.)

Type II superconductors are in the Meissner state up to the lower critical field, $B_{C1}$. At $B_{C1}$ magnetic flux penetrates the sample in the form of quantised flux lines. This produces a mixed state with superconducting and normal regions in the bulk of the sample. The superconductivity is only destroyed and the normal state resistance restored when the applied magnetic field is greater than an upper critical field, $B_{C2}$. Most alloys and compounds are type II superconductors. Most commercially useful superconductors are type II.

## 2.6 The London theory

In the Meissner effect, a persistent current will be induced to oppose the effect of the external field. However this current cannot flow in an infinitely thin surface layer otherwise the critical current density for the material would be exceeded. The induced current therefore must flow in a layer of finite depth, and the internal field in the superconductor will be non-zero in this layer. This effect cannot be deduced from Maxwell's equations alone.

In 1935 Fritz and Heinz London introduced two further equations to account for the magnetic properties in a superconductor [7]. These equations are phenomenological – they were introduced so the behaviour deduced from these equations agrees with that observed experimentally. The first of these equations is:

$$\mathbf{E} = \frac{m_S}{n_S e_S^2} \frac{\partial \mathbf{J}}{\partial t} \tag{2.1}$$

where $m_S$, $e_S$ and $n_S$ are the mass, charge and number density of superelectrons, respectively. $\mathbf{E}$ and $\mathbf{J}$ are the electric field and current density in the superconductor. This equation describes a conductor with zero resistance and is an equation of motion. The second equation is given by:

$$\mathbf{B} = -\frac{m_S}{n_S e_S^2} \nabla \times \mathbf{J} \tag{2.2}$$

This equation describes the Meissner effect in the conductor and the penetration of magnetic field. Using two of Maxwell's equations ($\nabla \times \mathbf{B} = \mu_0 \mathbf{J}$ and $\nabla.\mathbf{B} = 0$), the second equation can be rewritten as:

$$\nabla^2 \mathbf{B} = \frac{1}{\lambda_L^2} \mathbf{B} \tag{2.3}$$

where $\lambda_L$ is the London penetration depth and is defined by:

$$\lambda_L = \left( \frac{m}{\mu_0 n_s e^2} \right)^{\frac{1}{2}} \tag{2.4}$$

Solving Eqn. (2.3) it can be seen that the magnetic field decays exponentially upon penetrating a sample with the London penetration depth being the characteristic length scale.

## 2.7 Ginzburg-Landau theory

In 1950 Ginzburg and Landau developed a phenomenological theory based on the Landau theory of second order phase transitions [8]. This theory is an extension of the London theory, but uses quantum mechanics to predict the effect of magnetic field in a superconductor.

The main difference between London theory and Ginzburg-Landau theory is the introduction of a complex wavefunction, $\Psi$, as an order parameter to describe the superconducting electrons. This allows the spatial variation of superelectrons and nonlinear effects in the superconductor to be treated. The order parameter is defined to be zero in the normal state. The density of superconducting electrons related to the order parameter by:

$$n_S = |\Psi(\mathbf{r})|^2 \tag{2.5}$$

Assuming a second order phase transition, the free energy density of a superconductor can be expressed in terms of a power series of $|\Psi(\mathbf{r})|^2$.

$$f_S = f_N + \alpha_{GL}|\Psi(\mathbf{r})|^2 + \frac{\beta_{GL}}{2}|\Psi(\mathbf{r})|^4 + \frac{1}{2m_S}\left|(i\hbar\nabla + 2e\mathbf{A})\Psi\right|^2 + \frac{(B_e - B_i)^2}{2\mu_0} \quad (2.6)$$

where $\mathbf{A}$ is the vector potential, $\alpha$ and $\beta$ are constants, $B_e$ and $B_i$ are the external and internal fields respectively. Assuming the order parameter is small ($T$ is near $T_C$), higher order terms of $|\Psi(\mathbf{r})|^2$ can be neglected. The fourth term details the energy density arising from variations in the superelectron density and kinetic energy associated with supercurrents. The final term gives the energy required changing the magnetic field from the external field without superconductor, $B_e$, to $B_i$, the internal field. From Eqn. (2.6), the value of the order parameter infinitely deep inside the superconductor can be calculated to be $|\psi_\infty|^2 = -\alpha_{GL}/\beta_{GL}$.

The two Ginzburg-Landau equations are obtained by integrating Eqn. (2.6) to get the free energy of a superconductor and minimising with respect to $\Psi$ and $\mathbf{A}$.

$$\alpha\Psi + \beta|\Psi|^2\Psi + \frac{1}{2m_S}(-i\hbar\nabla - 2e\mathbf{A})^2\Psi = 0 \quad (2.7)$$

$$\mu_0\mathbf{J}_S = -\frac{i\hbar e_S}{2m_S}\left(\Psi^*\nabla\Psi - \Psi\nabla\Psi^*\right) - \frac{e_S^2}{m_S}|\Psi|^2\mathbf{A} \quad (2.8)$$

Ginzburg-Landau theory introduces two length scales. The first of these is the penetration depth (as described in London theory) which describes the length scale over which a magnetic field decays once entering a superconductor. The second is the coherence length, $\xi$, which is the length scale over which the order parameter increases upon entering a superconductor. The dimensionless Ginzburg-Landau parameter, $\kappa$, can now be defined,

$$\kappa = \frac{\lambda}{\xi}. \quad (2.9)$$

Ginzburg-Landau theory also provides a method of differentiating between type I and type II superconductors. By considering the surface energy density at a superconducting-normal phase boundary in a magnetic field, it can be shown that it is energetically favourable to create new normal-superconducting boundaries within a superconductor for certain values of $\kappa$. Therefore vortices of normal material form and the superconductor is in a mixed state – type II superconductivity. The crossover from positive to negative surface energy occurs at $\kappa = 1/\sqrt{2}$ with type I superconductors having $\kappa < 1/\sqrt{2}$ and type II having $\kappa > 1/\sqrt{2}$.

## 2.8    The flux line lattice

In 1957, Abrikosov solved the Ginzburg-Landau equations using appropriate boundary conditions for type II conductors in the field range $B_{C1} < B < B_{C2}$ [9]. He proposed that magnetic flux penetrated the superconductor by means of a finite number of vortices of normal material. Each of these vortices carries a quantum of magnetic flux,

$$\phi_0 = \frac{h}{2e} = 2.07 \times 10^{-15} \text{ Tm}^2 .$$

(2.10)
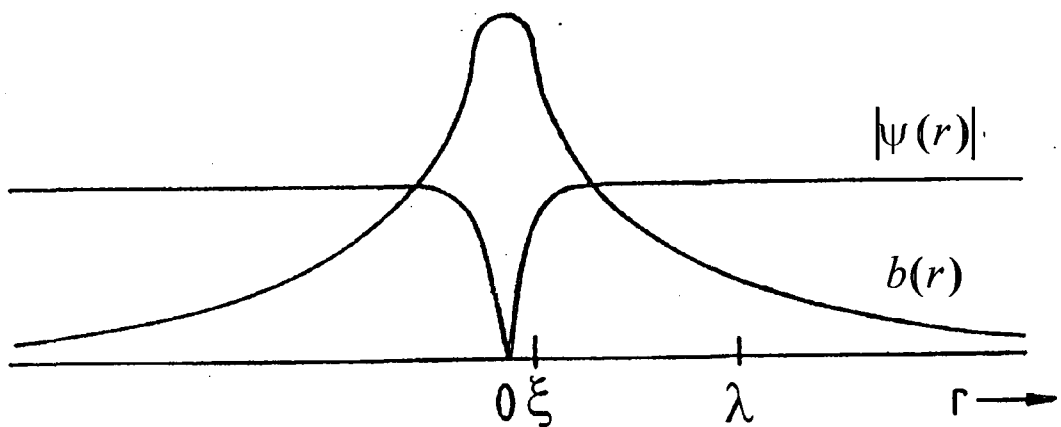


**Figure 2.2** Magnetic field , $b$, and Ginzburg-Landau order parameter, $\Psi$, as a function of distance from a single Abrikosov vortex [10].

9

Note that this expression for a flux quantum can be derived from Ginzburg-Landau theory. Figure 2.2 shows the variation in order parameter and magnetic field at a single Abrikosov flux vortex. These vortices are arranged in a regular vortex lattice. It was later shown by Kleiner that the most energetically favourable arrangement of the vortices was so that hexagonal (or triangular) as shown in Fig 2.3(a) [11]. This was later confirmed experimentally using the decoration technique [12] and more recently by scanning tunnelling microscope [13] as shown in Fig. 2.3(b).

The existence of vortices in type II superconductors asks the question whether the superconductor still exhibits perfect conductivity in a magnetic field. For an ideal homogeneous superconductor, the vortices would experience a Lorentz force per unit length of $\mathbf{J} \times \phi_0$ tending to make them move sideways, and they would exhibit an electrical resistance. However, in real materials, the vortices are pinned at inhomogeneities, so there is no resistance measured until a finite current is reached when the Lorentz force is large enough to exceed the pinning force.



(a)                               (b)
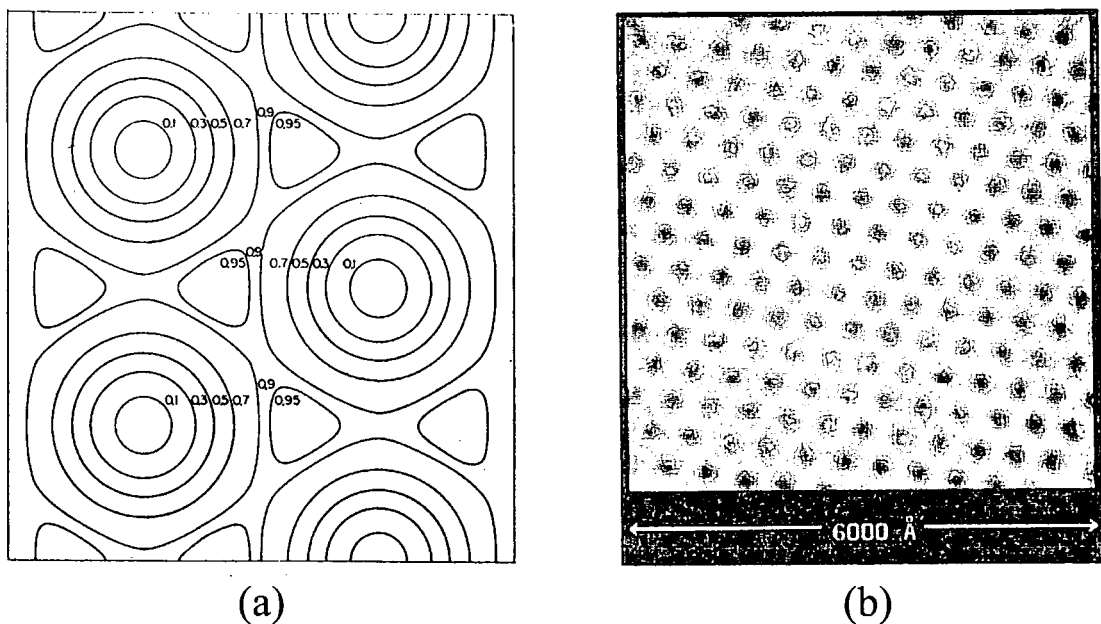
**Figure 2.3** The flux line lattice. (a) The spatial variation of the normalised order parameter, $|\psi|^2$, in a type II superconductor as calculated by Kleiner [11]. (b) Experimental verification of the Abrikosov flux lattice [13].

## 2.9 BCS theory

In 1957, Bardeen, Cooper and Schrieffer proposed a microscopic theory of superconductivity [14]. The fundamental idea behind this theory is the pairing of electrons and their interaction with the crystal lattice.

In 1956, Leon Cooper showed that if there was an attraction between electrons, the lowest energy state would be one where the electrons bound to form Cooper pairs. This would happen however weak the attractive interaction was [15]. The attractive force originates due to the interaction of the electrons with the lattice. An electron passing close to a positive ion will modify the vibration of the electron in the lattice. This ion will then interact with a second electron and the net effect of the two interactions is an apparent attractive force between the electrons. This can also be thought of as the exchange of a virtual phonon between the electrons.

BCS theory uses this phonon mediated pairing mechanism. The distance over which the electrons interact is the BCS coherence length, $\xi_0$. The electron pairs have equal and opposite momentum and spin and must be in the same quantum ground state. On applying a potential the Cooper pair cannot interact with the lattice otherwise it will have different momentum to the rest of the Cooper pairs. As this is not allowed, the Cooper pairs provide zero resistance transport of charge through the lattice. The only way to remove a Cooper pair from the ensemble is provide enough energy to break it apart.

As well as accounting for zero resistance and the Meissner effect, BCS theory predicts several other properties of superconductors. The first of these is the superconducting transition temperature corresponding to a phase transition. The temperature dependence of the thermodynamic critical field has also been predicted.

Before BCS theory, it had been observed that the critical temperature varied with the atomic mass of the isotope according to [16, 17]:

$$T_C \propto M^{-\frac{1}{2}} \qquad (2.11)$$

Although the isotope exponent $\approx -\frac{1}{2}$ for a few classic superconductors, experiments have shown that it can vary markedly for other materials. This has also been accounted for using BCS theory [18].

The final prediction that will be presented is the energy gap. This is given by the difference between a paired state and a two single electron states and is the energy required to break up the Cooper pair. This also means that for temperatures above 0 K there will be both paired and single electrons existing. The size of the gap will grow from $\Delta = 0$ at $T_C$ to a maximum at $T = 0$ K. The low temperature (near $T = 0$ K) specific heat is also evidence for an energy gap. Predictions for both the energy gap [19] and the low temperature specific heat have been verified experimentally [20].

It should be noted that Gor'kov used BCS theory to generate a microscopic derivation of Ginzburg-Landau theory given that the temperature is close enough to $T_C$ [21]. The superconducting charge carriers in Ginzburg-Landau theory were shown to be Cooper pairs. This meant that many practical problems could be solved using Ginzburg-Landau theory.

# Chapter 3

# A Review of Critical Current Density
# Measurements on Superconducting Strands

## 3.1    Introduction

It is important to know the transport critical current density ($J_C$) of superconducting strands as a function of applied magnetic field, temperature and strain for both fundamental studies of the mechanism that determines flux pinning in the strand and the determination of design specifications for industry. These measurements are also the focus of this thesis. This chapter provides a review of experimental techniques used in performing transport measurements to determine $J_C$, ranging from wiring and mounting samples correctly to specialised techniques for acquiring and analysing data. This chapter also forms the basis for a review article that is to be published [22].

This chapter is separated into four sections. In section 3.2, the general principles for measurement of critical current ($I_C$) as a function of field alone are considered. Different aspects of sample preparation are discussed in terms of sample geometry, associated mounting procedures and the wiring of voltage and current leads. The problem of eliminating current transfer and possible errors from measuring equipment are also presented. Following from this, section 3.3 presents different methods of analysing the data produced in a transport $J_C$ measurement. It explains how to differentiate between extrinsic and intrinsic properties of the strand and how to use the shape of the voltage-current characteristic to determine the distribution of $J_C$ as well as comparing the different methods for defining $J_C$.

A series of case studies are presented in section 3.4 for determining $I_C$ as a function of magnetic field in a liquid cryogen. These are for NbTi, $Nb_3Sn$ and BiSCCO, which are some of the most technologically important materials. All of these materials are or have been part of programs to produce standard $I_C$ test methods through either VAMAS (The Versailles Project on Advanced Materials and Standards) or IEC/TC90 (International
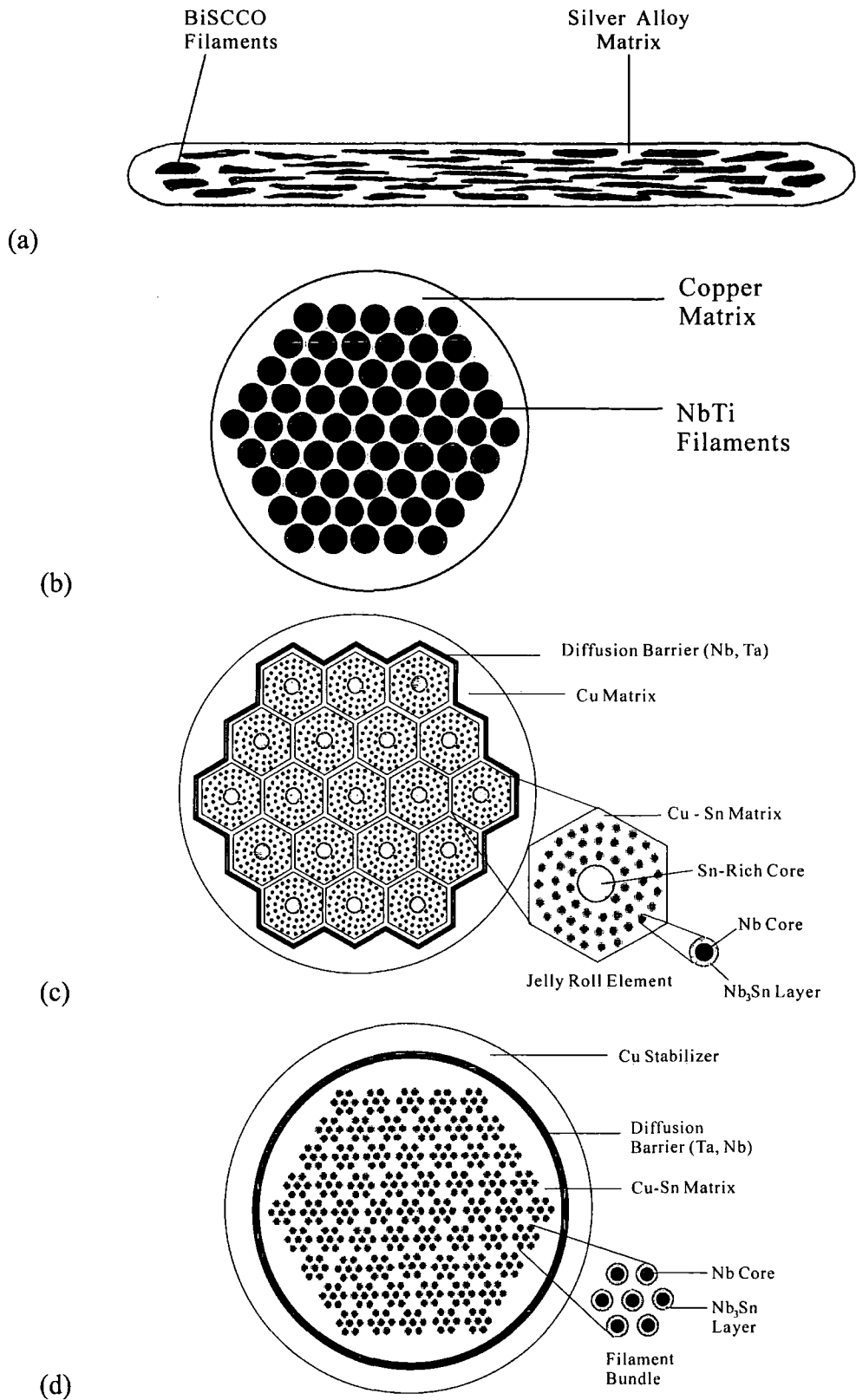
**Figure 3.1** Schematic diagrams of conductors. a) Ag-sheathed BiSCCO, b) Cu-NbTi, c) Modified Jelly Roll Nb₃Sn, d) Multifilamentary bronze route Nb₃Sn.

Electrotechnical Commission/Technical Committee 90) [23, 24]. Section 3.5 describes some more specialised test methods. These are pulsed methods, persistent mode measurements (used for measuring in the $pVm^{-1}$ regime) and determining $J_C$ as a function of applied magnetic field and temperature as well as field, temperature and strain. Finally, concluding comments are presented in section 3.6.

## 3.2    General principles for measuring $I_C$ when testing conductors

### 3.2.1    Four-terminal critical measurements on strand superconductors

There are many different designs for strand conductors. Schematic diagrams for some of the most common are shown in Fig. 3.1. In addition to the superconducting filaments, other components are illustrated including those required to produce the superconducting material itself (e.g. bronze) or to stabilise the conductor when carrying current (e.g. copper, silver). Some of the most important parameters for describing superconducting strands are listed in table 3.1. The construction of the strand is important when characterising its current carrying capacity (c.f. section 3.3). There are many excellent reviews and texts that discuss conductor design [26].

| | |
|---|---|
| Diameter | 1 mm |
| Number of filaments | 6,000 |
| Filament Diameter | 5 $\mu$m |
| Cu/Non Cu ratio | 2 |
| RRR of Cu | 100 |
| Twist Pitch | 60 mm |
| Twist direction | right-hand helix |
| Critical current at 10 T, 4.2 K (10 $\mu Vm^{-1}$) (100 $\mu Vm^{-1}$) | 150 A 160 A |
| $n$ value | 45 |
| Hysterisis loss ($\pm$ 5 T transverse field) ($\pm$ 5 T parallel field) | 3 $Jcm^{-3}$ 0.5 $Jcm^{-3}$ |

**Table 3.1** Typical parameters for a $Nb_3Sn$ strand.

(a)

(b)
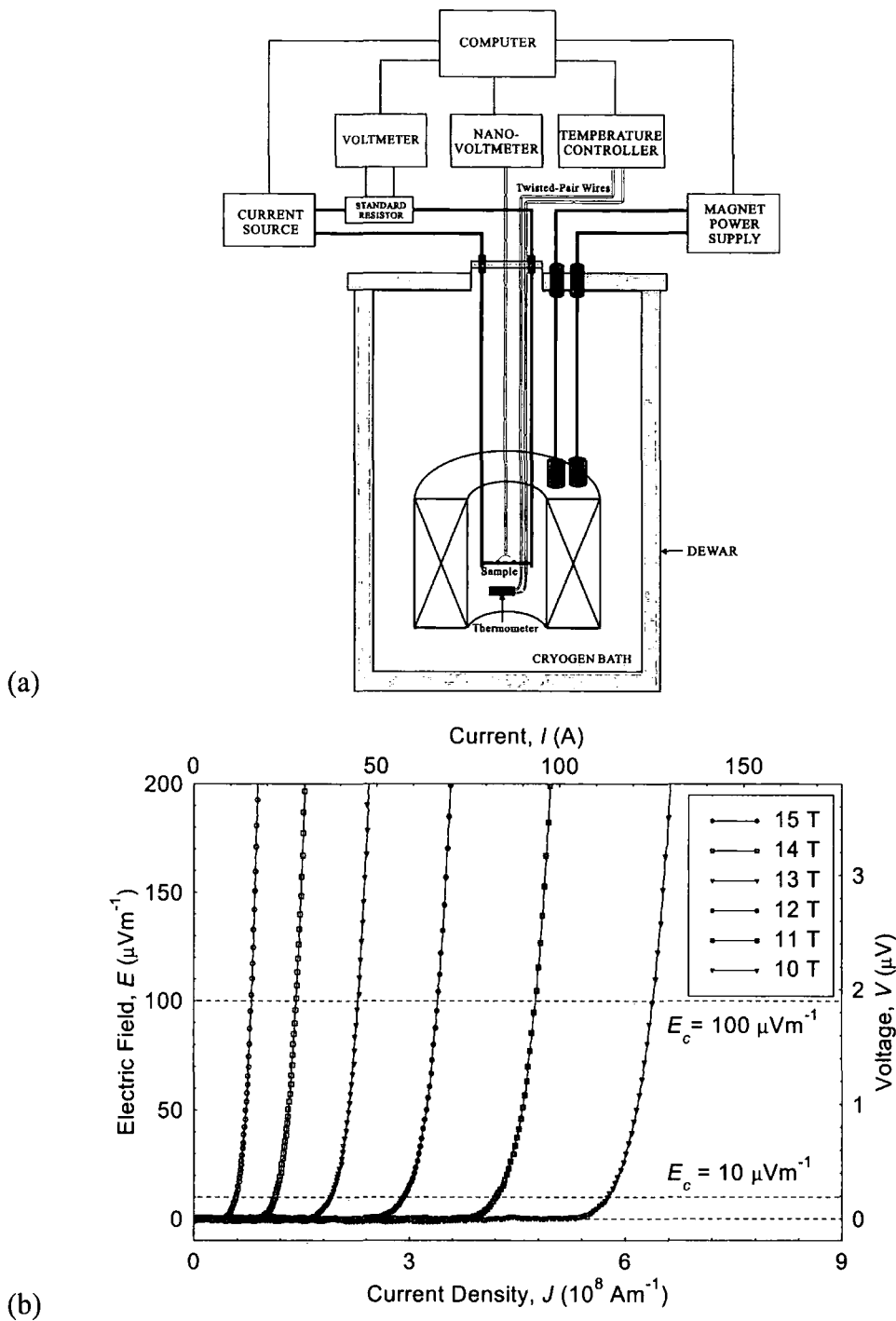
**Figure 3.2** a) A block diagram of the equipment used for measuring critical current density in strand conductors, and b) Typical $E$-$J$ characteristics generated for a $Nb_3Al$ strand [25]. The characteristics were generated as a function of field at 4.2 K. The data has been smoothed by finding an average electric field and current density using the 21 data points surrounding each individual data point. This has the effect of reducing the noise from the raw data without altering the shape of the transition.

The basic principle behind critical current measurements is the same as that for four-terminal resistance measurements. The current is applied to the sample by means of current contacts at both ends, and the voltage is measured across a pair of taps positioned across a length of the sample. The current is slowly increased from zero and the voltage across the taps is monitored. Eventually a $V$-$I$ (or equivalently an $E$-$J$) characteristic is measured. This process can be repeated as a function of applied magnetic field as illustrated in Fig. 3.2 (which includes a block diagram of a typical experimental arrangement and typical data). For the data shown, an $E$-field criteria of either 100 $\mu$V.m$^{-1}$ or 10 $\mu$V.m$^{-1}$ may be used (c.f. Section 3.3) to obtain the critical current density. Note that rigorously, vector notation should be used to describe electric and magnetic fields, currents and current densities. This is done in chapter 2 when describing London theory, Ginzburg-Landau theory and BCS theory where the magnitude and direction of these properties are known at each indiviual point. However when dealing with experimental critical current density measurements the same rigorous, detailed information is not known, and so this thesis will treat these properties as variables as is the convention in the literature.

## 3.2.2 Sample geometry and wiring
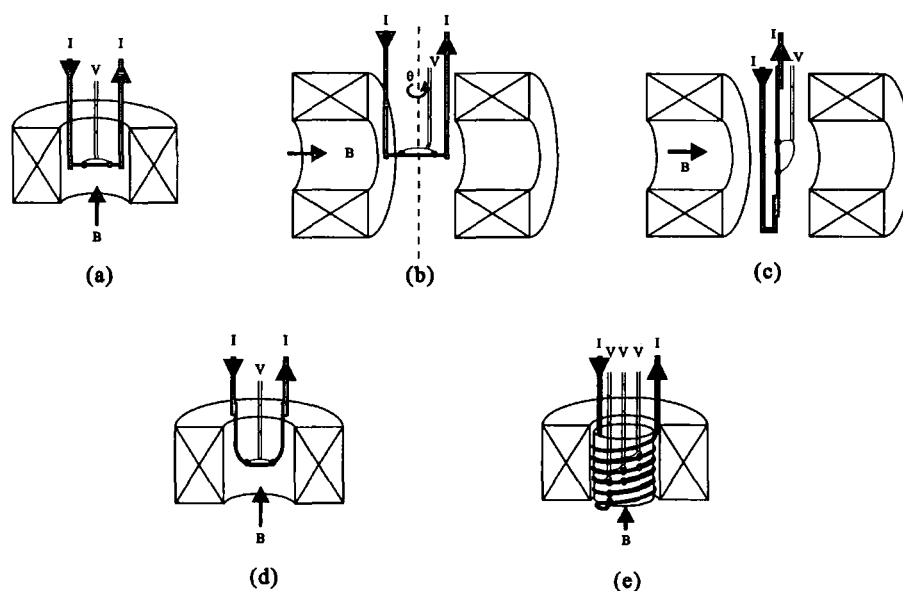


**Figure 3.3** Different geometries for performing critical current measurements. a) Short straight as used in solenoidal magnets, b) Short Straight for finding the angular dependence of critical current with magnetic field, c) Long Straight, d) Hairpin, e) Coil.

There are four different sample geometries that are most commonly used for measuring critical current, as shown in Fig. 3.3. These are the short straight, long straight, hairpin and coil geometries. The short straight geometry is most often used for conductors that are still in development where homogeneous long lengths of conductor are not available. The coil geometry is commonly used to test long lengths of conductors that are available commercially. The hair-pin and coil geometries are used for samples where current transfer from the current leads into the conductor are a problem (c.f. current transfer in section 3.2.6). In general the section of the conductor to be measured is perpendicular to the applied magnetic field. This orientation gives the lowest critical current, and therefore provides the most useful (limiting) case for high field applications [27, 28].

### 3.2.2.1    Short straight geometry

The short straight geometry is the simplest configuration. The short sample fits into the bore of a solenoidal magnet as shown in Fig 3.3a. No bending of the sample is required during mounting. The sample is easily supported against the Lorentz forces present when performing critical current measurements in applied magnetic fields, which is particularly important for brittle superconductors. The short sample geometry generates the least self field of all the configurations. The width of the bore (or cryostat tail) obviously provides a limiting size. Figure 3.3b shows how the short sample geometry can be used with a split pair magnet to measure the dependence of critical current on the orientation of current flow with respect to the direction of the applied field.

The short sample geometry provides the least sensitive $E$-field criterion for the determination of $J_C$ because of the short measuring length between the voltage taps. The orientation of the sample to the current leads means that there is a relatively small contact area for the current to penetrate into the sample compared with the other configurations. This, in turn, increases the contact resistance and heating. The reduced space around the sample limits the distance over which the current can distribute into the superconducting filaments. If the current has not transferred into the superconducting filaments, the voltage recorded across the taps, or dissipation, is associated with the current that has remained in the normal matrix. Hence voltage taps

need to be sufficiently separated from each other to allow sensitive $E$-field measurements to be made but also sufficiently separated from the current leads to avoid the problem of current transfer. Current transfer into the superconducting filaments is an important problem for measurements on small samples and will be addressed in more detail below.

### 3.2.2.2    Long straight geometry

A much greater length of sample is used in the long straight geometry, as shown in Fig. 3.3c. The voltage taps are in the homogenous region of the magnet and are well separated from the region where the current transfers from the current leads into the superconductor. A greater length of the sample is in contact with the current leads. This larger contact area reduces contact resistance and hence heating in this area. The longer length provides a longer measuring region for the voltage taps, leading to increased $E$-field sensitivity. In this geometry, however, the sample will no longer fit inside the narrow bore of a standard solenoidal magnet so split-pair (or Helmholtz) magnets are used, which are more expensive and do not reach as high fields. The homogeneity of the magnet determines the maximum length over which the voltage taps can be placed.

### 3.2.2.3    Hairpin geometry

The hairpin geometry shown in Fig 3.3d reduces the contact resistance between the leads and the conductor and hence reduces current transfer effects in a similar way to the long straight sample geometry. As the current leads are not near the voltage measurements region, a longer measuring distance between the voltage taps can be used and hence a better $E$-field sensitivity is achieved than in the short straight geometry. The hairpin geometry is suitable for ductile superconductors such as NbTi and conductors that can be reacted into the required shape (eg. $Nb_3Sn$). This geometry is not preferred for conductors that cannot be reacted in the hairpin shape, however, due to the strain produced in the sample on forming this configuration. Another aspect of this geometry is the curved nature of the sample. If the orientation of the conductor between the voltage taps varies with respect to the direction of applied magnetic field (e.g. is of

semi-circular shape) then the critical current measured will represent an angular average over applied field. A flat-bottomed hairpin is therefore preferable to a round-bottomed hairpin. Particular care must be taken to avoid damaging the sample when fabricating flat-bottomed samples.

### 3.2.2.4     Coil geometry

The coil geometry (Fig. 3.3e) is most commonly used for testing long lengths of conductor. It is suitable for ductile materials and conductors that can be reacted in the coil shape. The length of conductor used is the largest of all geometries, which means that the voltage taps can be placed the greatest distance apart, leading to the best $E$-field sensitivity. The contact resistance and the current transfer effect can be largely removed for this arrangement. Although the sample is oriented at an angle to the applied magnetic field, all parts of it experience the same offset angle, which generally has little effect. For example, in $Nb_3Sn$, a 7° pitch represents a change in $I_C$ of only 2% [27]. The coil geometry also provides the opportunity to investigate the homogeneity of the conductor by placing multiple sets of voltage taps along the sample.

### 3.2.3 Voltage wiring

There are many sources of voltage noise that can affect $J_C$ measurements. It is important to twist the voltage tap wires together and tie them down in order to prevent them from producing inductive voltage noise by moving in the magnetic field because of the flow of cryogenic gas. The area between the voltage wires and the sample should also be minimised to reduce the inductive loop area further. This procedure minimises inductive voltages which are produced either as the current through the conductor is increased or from the ripple in the applied magnetic field. For straight and hairpin samples, the voltage wires simply run along the surface of the conductor as shown in Fig 3.3. For the coil geometry, where the distance between voltage taps can be several turns, the wire from the first voltage tap should run alongside the sample until the second voltage tap. From there the wires should be twisted together. Other sources of voltage noise include thermoelectric, offset, ground loop, common mode and current transfer voltages [29]. If these voltages stay constant during the measurement then they

can be simply subtracted from the trace. This is achieved by comparing the voltage at zero current before and after the trace is measured. For the most sensitive voltage measurements, the twisted pair of voltage wires should be continuous from the sample to the voltmeter. In this case the thermoelectric voltages are minimised since there are no joints in the wire.

### 3.2.4 Current leads

The design of the current leads varies widely, depending on the application. The temperature gradient along sophisticated current leads, for example, can be controlled by more than one cryogenic liquid and/or the operation of a cryocooler. In general current leads must transport sufficiently large current without thermal runaway or burnout, have low electrical resistance so they do not generate much additional heat in the system and have low thermal conductivity to minimise static boil-off.

Unfortunately a room-temperature superconductor which may have ideal properties for current leads has not yet been discovered. Nevertheless, the high temperature oxide superconductors are being developed to significantly reduce power consumption and operating costs in large scale systems. Here some general design principles are considered for current leads that are made exclusively of metal and commonly used in testing strand superconductors. This will provide order of magnitude values for the size of current leads to aid scientists new to these measurements. For some detailed analysis, the reader is referred to two excellent reviews in the literature [26, 30]. In simple terms, the design of the current leads can be separated into three sections. The upper part of the lead, including the external power lead, generally includes a region where there is almost no gas flow. It is important in this region that the lead is sufficiently large that it doesn't burn out. In the middle section, there is the temperature difference from room temperature to the temperature of the cryogen. One must ensure that all the available enthalpy from the flowing cryogenic vapour is used to cool the lead in this region. In optimal design configurations, brass is often the preferred material. Tubes are used which are sufficiently bulky to provide a large surface area for efficient vapour cooling and far less likely to burnout than, for example, copper if temporarily operated outside optimal conditions [30]. An optimised constant diameter brass lead

operating from room temperature to liquid helium carries a current given by the condition $IL/A_{cs} \sim 1.5 \times 10^6$ A.m$^{-1}$ (where $I$ is the maximum current carried by the lead, $L$ is the length of the lead and $A_{cs}$ is the cross-sectional area of the brass). Hence for a 1 m lead, the current density in the brass should be 150 A.cm$^{-2}$. Under these conditions, the leads are sufficiently large that the resistive heating is not excessive at operating current, but sufficiently small to minimise static boil-off. The heat load ($Q$) into the helium cryogen is typically 1.08 W.kA$^{-1}$ or 1.4 litres of liquid helium boiling off per hour per kA. For brass leads vapour cooled with a nitrogen cryogen, $IL/A \sim 8 \times 10^5$ A.m$^{-1}$ and $Q = 25$ W.kA$^{-1}$ [30]. The lead in the bottom section of the device, which is submerged in the cryogen, should be relatively bulky to minimise resistive losses and, if possible, incorporate superconducting wires in parallel. The leads should also be large enough to prevent film boiling of the liquid cryogen [26]. During film boiling, the lead is enveloped by a layer of insulating gas which results in a rapid temperature rise of the current lead, and can change the sample temperature.

### 3.2.5 Material dependant issues

Experimental testing of conductors can involve making nano-volt measurements in high magnetic fields with hundreds of amps flowing through the conductor. The brittle nature of some conductors and the high Lorentz forces present mean that the conductor must be fastened securely to prevent the sample from moving and subsequently becoming damaged. Even for ductile conductors, sample movement may also lead to additional voltage noise, variations in the measured critical current, or even thermal runaway below $I_C$.

For straight and hairpin geometries, the sample is simply mounted onto the planar surface of the sample holder after reaction or fabrication. For the more complicated coil geometry, ductile materials are wound directly onto the cylindrical sample holder for testing. For brittle materials, conductors are either directly reacted on the sample holder or reacted on a mandrel in the furnace and then transferred after the reaction onto the sample holder. The direction of the Lorentz force per unit length ($F_L = IB$) is orientated so that it presses the sample against the sample holder and facilitates using less bonding agent to hold the sample in position. (Note again that rigorously vector notation should

22
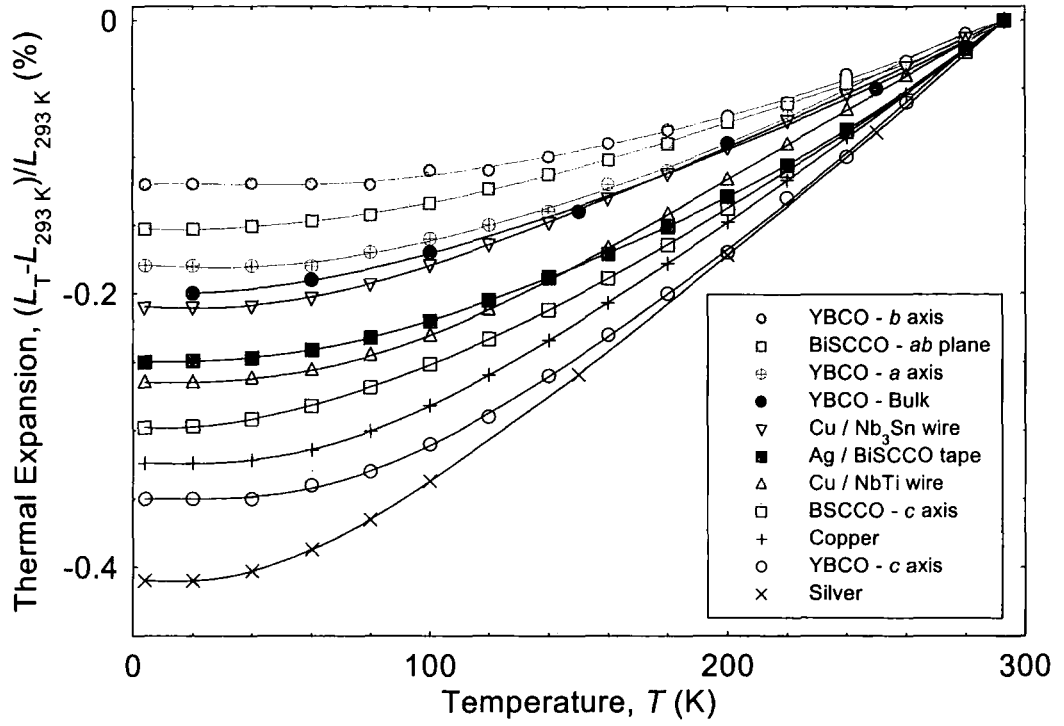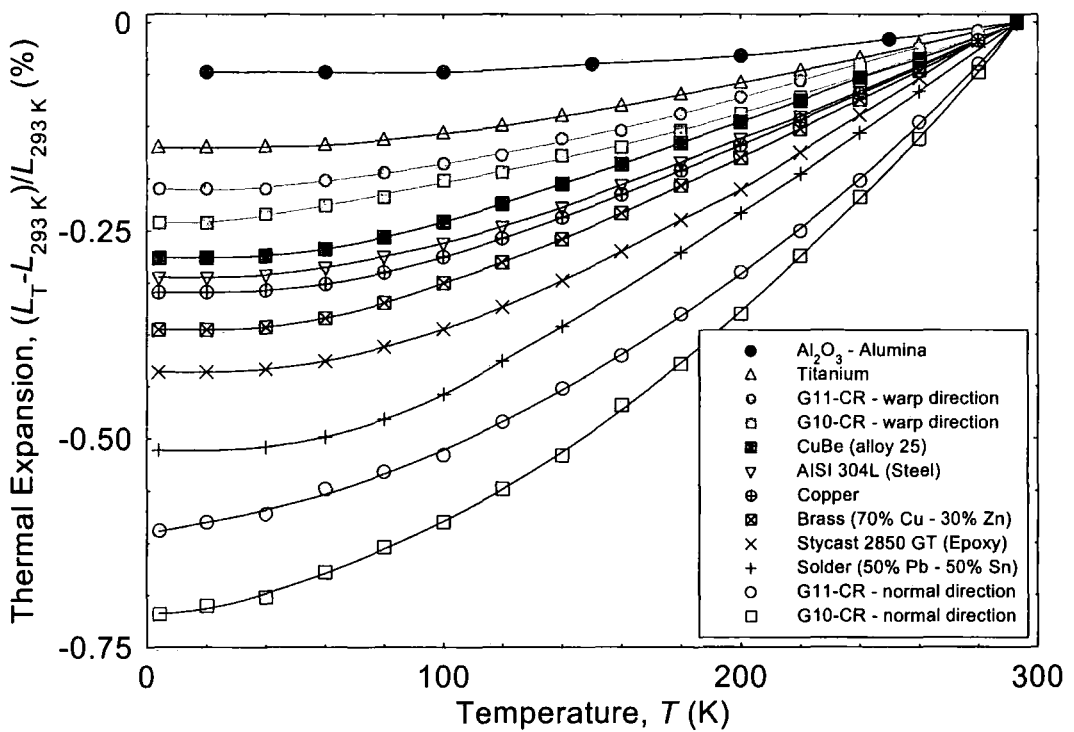
**Figure 3.4** Thermal expansion as a function of temperature for a) superconducting compounds, composites and matrix materials [31-36] – the Nb$_3$Sn conductor includes a tungsten core and b) mandrel materials and bonding agents [32, 37-39].

be used for forces such as the Lorentz force and pinning forces, $F_P$, however the conventions in the literature are being followed for the reasons given in section 3.2.1) Bonding agents include GE varnish, stycast, vacuum grease and solder. A high strength bonding material (e.g. epoxy or solder) is required if large Lorentz forces are present, since a low strength material such as grease may not stop the sample from moving. However, covering a sample with excess bonding agent must be avoided since this will inhibit the transfer of heat from the sample to the cryogen and can reduce the maximum measurable critical current.

It is important to try to match the coefficient of thermal expansion for the sample holder to that of the conductor. This ensures that there is no additional stress applied to the sample which may affect $I_C$ when the conductor is cooled from room temperature (or the soldering temperature if solder is the bonding agent) to the cryogenic testing temperature. The coefficient of thermal expansion is shown in Fig. 3.4, for some important cryogenic materials. Fig. 3.4a shows thermal expansion data for various superconducting compounds, composites and matrix materials [31-36]. It should be noted that the thermal expansion of the composites will depend ultimately on the construction of the wire. The thermal expansion for $Nb_3Sn$ at 4.2 K, for example, can be 0.21% (as shown in Fig 3.4a [34]) although these comprehensive data were taken on a six stranded cable indium soldered to a central tungsten core. In the VAMAS work, contractions of 0.26% to 0.28% were reported from room temperature to 77 K [40, 41]. Figure 3.4b shows the thermal expansion for various common mandrel or bonding materials [32, 37-39]. This parameter for G10-CR and G11-CR is similar in the fill and warp directions. The difference between the thermal expansion of the sample holder and the sample is transmitted between the two by the bonding agent. If a large amount of bonding material is used, both the sample holder and bonding material contribute to the net stress on the sample. The stronger the bonding material, the greater the strain produced by any differential thermal expansion between the sample holder and conductor. The type of bonding agent used must therefore be considered carefully for each particular experiment (see the case studies in section 3.4).

### 3.2.6 The current transfer problem

There are two forms of current transfer. The first of these is the initial transfer of current from the current leads into the conductor. Measurements of $J_C$ are most reliable with the voltage taps as far away as possible from the current transfer regions in the vicinity of the current leads. This ensures that the properties of the conductor alone are measured, rather than the properties of the current lead joint resistances. The second current transfer process is between filaments and is due generally to a distribution in $I_C$. This process depends on the detailed structure and materials in the composite conductor, including the size and distribution of the filaments within the conductor matrix.

In order to transfer current from the current leads into the superconducting filaments, the current must pass through an ohmic matrix or sheath. The voltages produced in the current transfer region increase linearly with current (unless, of course, there is heating in the sample). It has been shown [42] that the minimum distance required to allow for current transfer to a monocore conductor is given by;

$$L = d \sqrt{\frac{0.1}{N} \frac{\rho_m}{\rho_C}}$$

(3.1)

where $d$ is the diameter of the filament region of the wire (i.e. the area of the wire containing the superconductor filaments), $N$ is the index of transition which describes the shape of the $V$-$I$ curve for the superconductor (c.f. section 3.3), $\rho_m$ is the resistivity of the matrix, and $\rho_C$ is the resistivity criterion used to define the critical current density. This equation yields typical current transfer distances of approximately $30d$ for Nb$_3$Sn and $3d$ for NbTi [27]. The increased current transfer length for Nb$_3$Sn compared with NbTi is due to the lower values of $N$ (i.e. 20 for Nb$_3$Sn compared to 40 for NbTi), and the large resistivity of the matrix (bronze for Nb$_3$Sn compared to pure copper for NbTi). In BiSCCO 2223 and 2122, the transfer lengths were found to be of order a millimetre at 4.2 K, and tenths of millimetres at 77 K [43]. This unexpected temperature dependence was attributed to a large boundary resistance at the interface between the superconductor and the silver sheath.

The current transfer lengths affect directly the choice of sample geometry. Samples are typically no longer than 25 mm in the short straight geometry. This means that measurements on conductors with high resistivity matrix (e.g. bronze route $Nb_3Sn$) are best not made using the short sample geometry. However, because the current transfer is not an intrinsic property of the wire, the resistive voltage can be subtracted from the *V-I* trace [44]. Note that when testing conductors with twisted filaments (which is required in commercial conductors to minimise ac. losses), the current contact length should be greater than the twist pitch of the sample to allow the current to enter the filaments evenly [45].

The second type of current transfer is an intrinsic property of the conductor. It is particularly important for ac applications where currents can redistribute between the filaments. In dc applications, a quantitative picture of the dissipative state in inhomogeneous high $J_C$ conductors depends on the *E*-field range under investigation. At low *E*-fields, for example in NMR (or persistent mode) applications, the superconducting filaments may have a resistance that is still much smaller than that of the matrix. In this case, the *V-I* transition is largely unaffected by the matrix and the current transfer is not important. In high *E*-fields, sausaging of the filaments or inhomogeneities may mean the local $I_C$ in a filament is exceeded, current passes through the matrix either back into the sausaged filament or into another filament [43].

### 3.2.7 External circuitry

### 3.2.7.1 Current source and voltmeter

A smooth current source and nanovoltmeter are typically used under computer control for making $J_C$ measurements. The current through the conductor is usually recorded by measuring the voltage drop across a standard resistor, and the voltage across the conductor by the nanovoltmeter, as shown in Fig. 3.2. The sensitivity and response time of the nanovoltmeter is dependant on the quality of the instrument and the filters used. Voltages at about 100 nV can be measured over an interval of around 50 ms. Standard good practice must be observed when using filters to reduce the voltage noise on a *V-I* characteristic. In general, the greater the filter used, the larger the time delay

before the correct voltage reading is reached. If the response time of the filtering mode is too long, the apparent voltage will be less than the actual voltage, and the $V$-$I$ transition will artificially broaden giving a false value for $I_C$. Measurements below the 10 nV range are possible in low noise systems with long measurement times. Noise levels can be improved if unfiltered data are measured by computer, with subsequent editing of outlying points and numerically smoothing the data [46]. The current source itself can be a source of voltage noise. For example using a analogue nanovoltmeter it has been found that a battery power supply gave a noise level during the measurement of $\sim$ 2 nV, whereas a silicon controlled rectifier gave $\sim$ 100 nV [27].

In the most widely used measurement technique, the current is simply ramped at a constant rate until the required voltage is generated across the sample to determine $J_C$. The measurement should be sufficiently slow that the $V$-$I$ trace does not depend on the rate of increase of current. The rate of increase of current must be small enough that inductive voltages generated vary by less than the voltage used to determine $J_C$. Other factors that limit the ramp rate or the current are possible sample movement and induced eddy currents in metallic sample holders and probe components which cause heating. In the stepped method technique, point-wise data are taken with a delay to allow the inductive voltage to decay. A third method is to ramp quickly to below $I_C$, wait for the inductive voltage to decay and then sweep the current very slowly through the transition. Pulsed techniques are also used (c.f. section 3.4) and at high $E$-fields typically agree with dc methods to better than $\sim$ 0.2% [47] but usually with higher noise levels. A calibrated superconducting simulator is available to assess experimental procedure [48].

Most experimental arrangements also incorporate some form of quench protection device. This is particularly important when using unstabilised conductors where there is significant risk of burning out the sample. The protection automatically resets the current to zero when a pre-determined voltage across the sample is reached. Quench protection can be computer controlled or included as an independent analogue component [27].

### 3.2.7.2 Magnetic field

The magnetic field for critical current measurements is often provided by using a superconducting magnet. These systems can produce fields of up to ~ 23 T for a solenoidal type magnet and about 15 T for a split pair magnet. In the VAMAS $Nb_3Sn$ project, it was recommended that the field for testing conductors should be accurate to 1% and have a precision of 0.5%. The random deviation of magnet field should be less than 0.5% and its homogeneity should be of uniformity ± 1% over the length of the sample between the voltage taps [49].

Above ~ 1 T, high field superconducting magnets exhibit an almost linear dependence between the field generated and the current through the magnet. At low fields, however, hysteresis can cause problems when trying to determine the low field properties of conductors. There are various approaches that can be taken to eliminate errors due to the remnant field. The field at the sample can be measured independently using a Hall or NMR probe. This is the only technique that allows the hysteretic behaviour of $J_C$ for the conductor to be measured in increasing and decreasing applied field. The remnant field can be reduced to typically less than ± 20 mT by degaussing the magnet. This involves sweeping the field from a high value through zero and back, reducing the amplitude and sweep rate at each reversal. An alternative is to initiate a controlled quench in the magnet. This can be done by means of a carefully designed quench heater [50] incorporated within the turns of the magnet which forces the temperature of the superconducting windings to above $T_C$. This completely destroys the remnant field. However, the dangers of damaging the magnet by quenching should be noted.

For dc fields of up to ~ 30 T, high power resistive magnets (generally available at international facilities) can also be used. These magnets produce no remnant field. However, the water cooling and power required for this design of magnet are large with commensurate mechanical vibrations in the magnet system, which can cause additional sources of voltage noise.

## 3.3    Voltage-current characteristics and critical current analysis
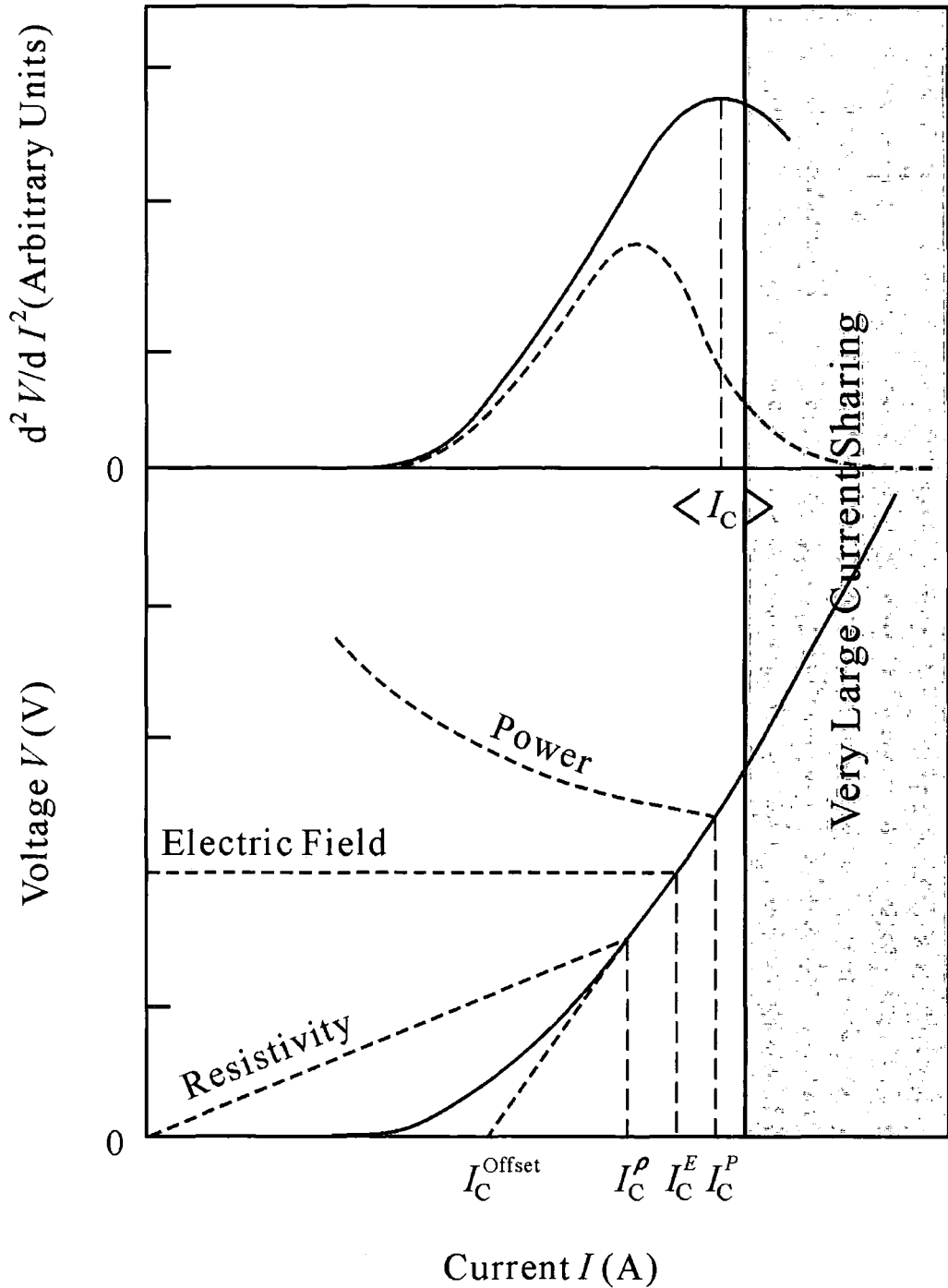


**Figure 3.5** The lower panel shows the conventions used to define $I_C$ – the electric field, resistivity and power criteria as well as the offset method. The upper panel shows the variation of $d^2V/dI^2$ with current. The dashed line is for the conductor and shunt resistance [51]. The solid line is for the superconductor alone and can be equated to the distribution in $I_C$.

### 3.3.1 Defining the critical current ($I_C$) and the critical density ($J_C$)

A generic voltage-current ($V$-$I$) characteristic is shown in Fig. 3.5 with the various conventions used to define the critical current. The choice of convention depends on how the data are to be used. For example, in standard high field solenoids the engineering current density at an electric field criterion of about 10 $\mu$V.m$^{-1}$ will determine the performance of the magnet. For NMR applications, on the other hand, where the magnet is in persistent mode, the current density at an $E$-field about six orders of magnitude lower is required. The critical current can consequently be strongly dependent on the chosen criterion [27].

The most commonly used convention for defining critical current ($I_C$) is an electric field criterion ($E_C$) given by $E_C = V/L$, where $V$ is the voltage difference between the voltage taps and $L$ is the length of wire between the voltage taps. Typically the electric field used to define $I_C$ is 10 $\mu$Vm$^{-1}$ or 100 $\mu$Vm$^{-1}$: $I_C$ never falls to zero, using such criteria. A resistive (ohmic) sample, which has no curvature on the V-I trace, will still cross the electric field criteria at some point, leading to a value of $I_C$. For typical conductors (~ 1 mm diameter), this non-superconducting current (for example in the Cu that stabilises the conductor) ranges from 10 – 500 mA when the $E$-field is 10 $\mu$Vm$^{-1}$, which is not significant in engineering applications (although as discussed below it can be important for more fundamental studies). In the case of short straight geometry where the measurement distance is typically no longer than 1 cm, a voltage sensitivity of less than 100 nV is required to obtain an electric field criteria of 10 $\mu$Vm$^{-1}$. It should be noted, however, that low current densities obtained using this criterion can be characteristic of non-superconducting metals.

The resistivity criterion ($\rho_C$) for $J_C$ is given by $\rho_C = VA_{cs}/IL$, where $V$ is the voltage difference between the voltage taps, $L$ is the length of the wire between the voltage taps, $A_{cs}$ is the cross sectional area of the wire and $I$ is the current through the wire. Values of $J_C$ are often quoted at $\rho_C$ of $10^{-14}$ $\Omega$m or $10^{-13}$ $\Omega$m. The critical current using the resistivity criteria disappears at high fields as long as that chosen is less than the normal state resistivity of the conductor. However, problems can arise in fundamental studies if the resistivity criterion is used. For example, some superconductors do not show a zero

resistance region in high fields. If the (superconducting) flux flow region has a resistivity above that of the resistivity criterion, $I_C$ is zero but the conductor remains in the superconducting state.

A power criterion ($P_C$) defined by $P_C = IV$, is sometimes used in large scale applications. It can be a useful criterion in magnet design to specify the maximum allowed consumption of cryogen and thus a suitable working current.

The offset method [44] is a method for calculating $I_C$ which attempts to minimise the problems associated with the electrical field or resistivity criterion. $I_C$ is calculated in two stages. A tangent to the $V$-$I$ curve is constructed at an electric field criteria given by $E_C$. The critical current is then defined as the current at which the tangent is extrapolated to zero voltage. This procedure provides an attempt to subtract the current flowing in the non-superconducting components from the total current, which can be useful for samples where there is a large shunt in parallel with the superconductor.

The critical current density can be calculated in three ways once the critical current has been measured. For engineering applications, the conductor is treated as a single entity. The $V$-$I$ characteristic for the entire conductor including the stabilising material and the matrix is required. The engineering critical current density ($J_C^E$ or $J_E$) is defined as the critical current divided by the cross sectional area of the entire conductor. This is the important parameter when designing systems such as magnets. The second definition of current density is relevant for comparing and developing conductors of different superconducting materials. It can be seen in Fig. 3.1 that, in contrast to NbTi and BiSCCO, $Nb_3Sn$ conductor has matrix material such as (tin depleted) bronze, which is neither superconducting nor contributes to stabilising the conductor. However, it is required in the processing of the conductor and cannot be removed. Hence $J_{C(Non-Cu)}$ can be calculated using the area of the superconductor that is not matrix material (i.e. non-Cu or non-Ag). This provides the second definition of $J_C$ and is particularly useful for wire manufacturers. In fundamental studies, the critical current density in the superconducting layer alone is required. Measuring the cross sectional area (CSA) in NbTi or BiSCCO is relatively straightforward. However, if there are fine

superconducting filaments as in $Nb_3Sn$ or $Nb_3Al$ conductors, it can require electron microscopy to determine the CSA of all the superconducting layers alone.

### 3.3.2 Flux creep, flux flow and damage

In this section the difficulties that can occur in interpreting $V$-$I$ traces are discussed. Poor experimental technique can produce artefacts in the data that can be very misleading, particularly when measuring brittle superconductors. Figure 3.6 shows five $V$-$I$ characteristics that will be discussed in this context. These data are schematic representations of actual characteristics with their important features enhanced, and can be explained as follows:
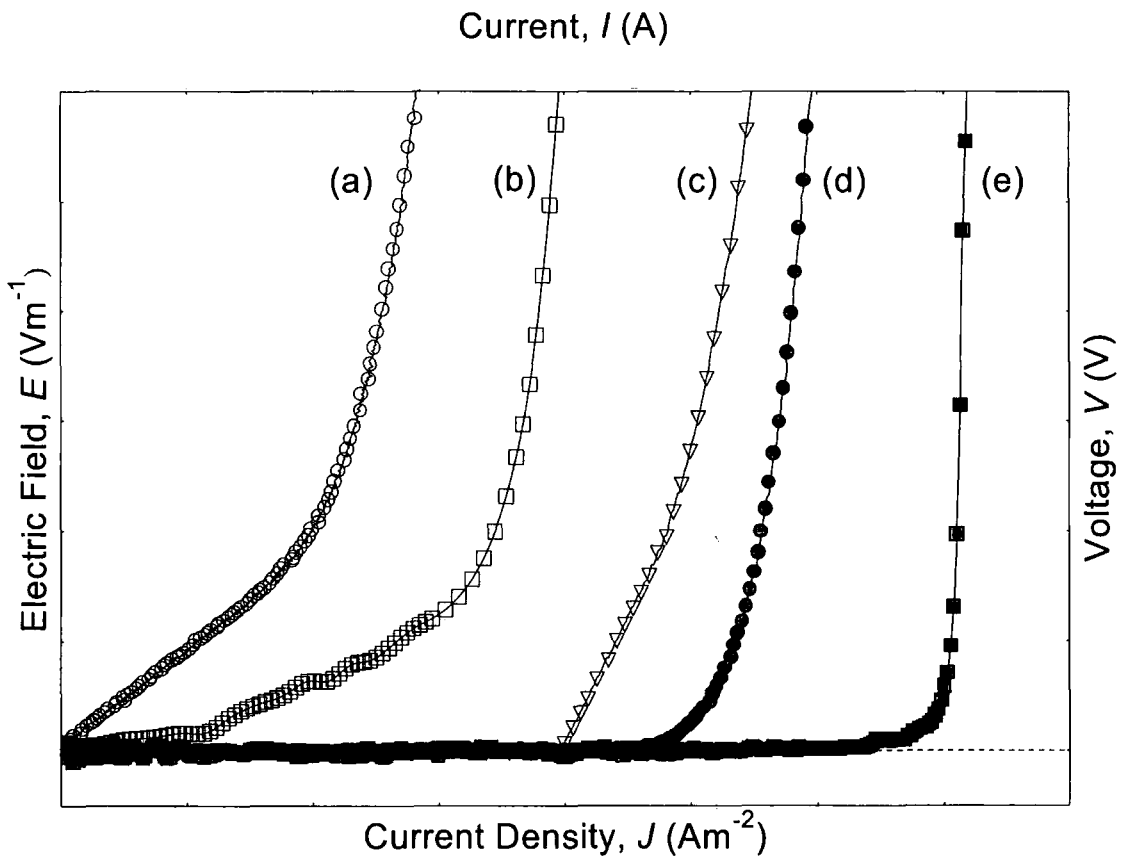
**Figure 3.6** Schematic $V$-$I$ characteristics. (a) current transfer due to insufficient seperation between voltage taps and current leads. (b) flux creep at low currents before the transition when flux flow sets in. (c) current transfer due to a limited number of damaged filaments. (d) zero resistance followed by a flux flow transition (the transition can also be seen in (a) and (c)). (e) thermal runaway.

Fig. 3.6(a) There is a resistive (current transfer) region at low currents due to an insufficient separation between the current leads and the voltage taps. The transition to the normal conducting state is evident at high currents.

Fig. 3.6(b) Flux creep is evident at low currents. At high currents, the transition rises sharply as flux flow sets in.

Fig. 3.6(c) Zero resistance occurs at low currents with supercurrent flowing in undamaged filaments. At intermediate currents, there is a resistance due to current transfer in and out of a limited number of damaged filaments. At high currents, the conductor is in the flux flow state.

Fig. 3.6(d) There is zero resistance region followed by a flux flow transition.

Fig. 3.6(e) There is zero resistance until a quench occurs in the conductor. This is followed by heating and thermal runaway.

The explanations provided for the curves (a) – (e) are clearly not unique. If the effects of heating due to filament damage or tunnelling across cracks are introduced for example, one can relatively easily provide a different explanation for any of the *V-I* traces. The critical point to note from these data is that one can misinterpret curves (a), (c) and (e), which do not show the intrinsic properties of the conductor, for curves (b) and (d) which are intrinsic. From the *V-I* trace alone, it may not be possible to distinguish reliably between flux creep (intrinsic to the conductor) and current transfer (and heating), which can occur because of damage or poor measuring technique. It is concluded that it is *essential* to employ good practice in mounting samples and is preferable that more than one length of the conductor is measured to ensure the reliability of the results.

### 3.3.3 Shape of the transition

The shape of the *E-J* characteristics of a conductor can be described using

$$E = \alpha J^N \tag{3.2}$$

or less frequently

$$E = E_0 \exp\left(\frac{J - J_0}{J_1}\right) \qquad (3.3)$$

where $\alpha$, $E_0$, $N$, $J_0$ and $J_1$ are all experimental or materials constants. The $N$-value is often called the order of transition or index. It is important to note that $N$ characterises the entire conducting path between the voltage taps, including the stabilising material. If the conductor is mounted on a metallic (low resistance) sample holder, although current sharing through the shunt may only affect $I_C$ slightly (depending on the criterion used), the value of $N$ can decrease significantly [52]. High $N$ values tend to signify more homogeneous superconductors. Typical values for $N$ lie between 10 and 100 and in engineering applications tend to be used as a figure of merit.

In flux pinning and flux motion studies of conductors, analysis techniques are used to develop the data beyond the empirical expressions for the $E$-$J$ characteristics and the (arbitrary) conventions used to define $J_C$. For conductors at low temperature, where thermal activation is not important, the $E$-$J$ transition of a superconductor can be described by [53].

$$E(J) = \rho_{ff} \int_0^J (J - J_i) f(J_i) dJ_i \qquad (3.4)$$

where $J_i$ is the local critical current, $f(J_i)$ is the distribution of critical currents in the sample, and $\rho_{ff}$ is the resistivity describing flux flow in regions of the superconductor where the current exceeds the local critical current. In the analysis, the current density terms represent the current density flowing in the superconductor in which case current flowing in the shunt and the stabilising material of the conductor must be subtracted to obtain the correct $f(J_i)$ function [51]. This has been done by measuring the $E$-$J$ characteristic above $B_{C2}(T)$ [54]. For high temperature superconductors (HTS), this can be achieved by etching off the matrix [51, 55]. By invoking the central limit theorem, it can be assumed that $f(J_i)$ can be described by a normal distribution of the form:

$$f(J_i) = \frac{1}{(2\pi)^{\frac{1}{2}}} \frac{\beta}{J_C} \exp\left\{-\frac{1}{2}\left[\beta\left(\frac{J_i - \overline{J_C}}{J_C}\right)\right]^2\right\} \quad , \quad \beta = \frac{\overline{J_C}}{\sigma(J_C)} \qquad (3.5)$$

where $\overline{J_C}$ is the average $J_c$ of the distribution and $\sigma(\overline{J_C})$ is the standard deviation of the critical current distribution [53, 54]. Good agreement is found between experimental data and Eqns. 3.4 and 3.5. Detailed variable temperature, variable field measurements have been completed on NbTi [54, 56], Nb$_3$Sn [57] and V$_3$Ga [58] conductors and scaling laws found for $\rho_{ff}$, $\beta$, $N$ and $\overline{J_C}$. Equating the empirical equation (Eqn. 3.2) to the more physical one (Eqn. 3.4) at $J = \overline{J_C}$ [56] gives:

$$\beta = N\left(\frac{2}{\pi}\right)^{\frac{1}{2}} \tag{3.6}$$

This equation is consistent with the empirical finding that homogeneous materials have high values of $N$ (it is not valid for very low $N$ values ($N < 5$) at low $E$-fields [59, 60]). The distribution of critical current densities can be derived explicitly making no assumption about the form of the distribution using [59, 61]:

$$f(J_0) = \frac{1}{\rho}\left(\frac{d^2E}{dJ^2}\right)_{J=J_0} \tag{3.7}$$

A graphical representation of this analysis is shown in Fig. 3.5. However, the distribution obtained is sensitive to noise and the algorithm used to calculate the second derivative [62]. It is difficult to measure the distribution at high current because of heating and the local hot spots that occur at high $E$-field values. This is particularly problematic if the stabilising material is etched out of the conductor [51].

The formulism used to describe the vortex glass – vortex liquid phase transition in weak-pinning high-$T_C$ superconductors has also been developed to describe the $E$-$J$ characteristics. Generalised scaling laws have been developed [63] by considering thermal activation and flux pinning. It is clear that similar scaling laws are also to be expected if a distribution in $T_C$ and $B_{C2}(T)$ is introduced. Scaling in the $E$-$J$ characteristics has been observed in both low temperature [64] and high temperature superconductors [63].

The two approaches for the analysis of *E-J* characteristics are essentially complementary. At low fields and temperatures, $J_C$ is high and thermal activation may play little role. Sausaging in the conductor filaments, variations in microstructure and composition are important and in these cases one can expect the resultant distribution in $J_C$ to be described using Eqn. 3.4. At the highest fields and temperatures, the distribution in fundamental properties, thermal activation, percolation and regions of very low $J_C$ may dominate the properties of the conductor. In this case the phase transition formulism is probably most appropriate. These two formulisms are both being developed to better understand and optimise the distribution and magnitude of $J_C$ in conductors.

## 3.4    Case studies for testing different materials

### 3.4.1  $I_C$ as function of field in liquid

This section describes mounting techniques for NbTi, Nb$_3$Sn and BiSCCO conductors. All of these materials either have been or are currently part of international comparative studies for the standardisation of measurement techniques. The typical errors found when measuring each material are also discussed. Very accurate and stable temperature control can be achieved when making critical current measurements by direct immersion of the conductor in liquid cryogen. However, there are some general points to be aware of when measuring any of these materials:

The vapour pressure of the gas can be monitored to give the temperature of the bath as suggested by the VAMAS Technical Working Party in their standard method for $I_C$ determination of Nb$_3$Sn wires [49]. Bath temperatures can be determined from standard tables [65]. Temperature errors can occur when using liquid nitrogen if air (primarily oxygen) has dissolved in the nitrogen due to associated changes in the vapour pressure – temperature relation. If atmospheric pressure is used, care must be taken that there is not a build-up of pressure in the dewar as the critical current transition is reached.

It is prudent to monitor the temperature of the sample during the $V$-$I$ measurement to ensure there is no heating. The type of thermometer used should be chosen based on its properties in high magnetic field, its sensitivity and its response time.

For measurements in the coil geometry, both metal (normally stainless steel) and glass fibre reinforced plastics/epoxy (FRP) are commonly used for the sample holder. The wire should be wound on to a spirally grooved sample holder to help prevent it from moving during the measurement. The spiral groove should be at an angle no more than $7°$ to reduce the effects of placing the sample at an angle to the applied magnetic field. Copper ends are fitted to the sample holder and act as current contacts to which the ends of the sample are soldered. The direction of the Lorentz force during measurements should be into the sample holder. The FRP sample holders should be machined from plate stock so the axis of the tube/cylinder is along the normal direction of the FRP plate. It is less preferred to use rolled FRP tubes with the axis of the tube in "fill" direction because the thermal contraction is more anisotropic than with machined plate and depends on the dimensions on the tube [66]. The groove should be of $60°$ V-cross-section with a depth approximately equal to the diameter of the wire. Thin-walled stainless steel sample holders should also be grooved to guide the wire [49]. An important consideration when using metallic sample holders is the current sharing that occurs in the dissipative state. Current sharing can produce a large reduction in the $N$-value particularly if a solder bond is used [52]. For standard testing of commercial wires for engineering purposes, current sharing is best avoided. However, although the technologically important $J_E$ may not be accurately measurable on soldered metallic sample holders, in fundamental studies that require $J_C$ (i.e. for the superconductor alone) even the current sharing through the stabilising matrix within the conductor should be subtracted from the measured data. In such experiments one can use soldered metallic sample holders and treat current sharing through the normal shunt and stabilising material as a single path in parallel with the superconductor. Indeed in such studies, it has been found useful to electroplate a very thin copper layer onto the stainless steel sample holder to ease the soldering process, prevent unstabilised conductors from burning out and ensure that localised damaged sections of the wire do not quench the entire conductor during testing.

When using solder, in particular for attaching voltage taps, it is important not to thermally shock the conductor. For brittle superconductors, a hot-air gun may be used to warm the conductor uniformly to just below the melting point of the solder before using the soldering iron to attach leads. The temperature of the gun can be set using a thermocouple-based thermometer. Low temperature solder such as $In_{0.52}Sn_{0.48}$ (M.P. $\sim$ 118 °C) can be used to minimise thermal shock [67]. It should also be noted that standard PbSn solder (M.P. $\sim$ 190 °C) is superconducting at 4.2 K up to $\sim$ 0.1 T.

In low fields, $I_C$ can be strongly dependent on whether the applied field has been increased or decreased to obtain the required value (i.e. $I_C$ is history dependent) [68-70].

In general one tries to match the thermal contraction of the sample holder to that of the conductor. The properties of any conductor are determined by all its component parts. The sample holders suggested by the standards testing community have been chosen as appropriate for a reasonable range of the common commercial conductors.

### 3.4.2 NbTi

NbTi is usually measured using the coil geometry. Insulation can be removed chemically using a mixture of phenol/methylene chloride to prevent mechanical damage during sample preparation. Although NbTi is a ductile superconductor and $J_C$ is reasonably insensitive to strain [71], care must be taken to avoid placing any extra strain on the wire during winding.

Both FRP and stainless steel holders can be used. The FRP used is G-11CR (US notation) or EP GC 203 (European notation) which has a thermal contraction similar to NbTi. If the sample is held in place using varnish, a strong epoxy (such as stycast), vacuum grease, or no bond at all, this has little effect on $I_C$ [72]. In the IEC/TC90 standardisation of the NbTi critical current measurement test method, stainless steel sample holders and FRP were used with low temperature adhesives. The use of solder was not recommended. The critical current values for the samples on steel sample holders were only slightly different to samples mounted on G10 [73].

One of the "standard measurements" laboratories in the USA (NBS/NIST) has produced a standard reference NbTi material (SRM 1457) that has been tested for long length homogeneity and measured extensively in interlaboratory comparisons. Critical currents were measured at 2, 4, 6 and 8 T on FRP for temperatures from 3.90 K to 4.24 K using electric field criteria from 5 to 20 $\mu Vm^{-1}$. The total uncertainty of the reported critical current values at any of the four magnetic fields was no greater than 2.6% [71]. In a second series of measurements, the uncertainties for the critical currents (measured at an electric field criteria of 10 $\mu Vm^{-1}$) were found to be 1.71% and 1.97%, and the difference between the interlaboratory averages and certified critical current were 0.2% and 0.3% for 6 and 8 T respectively [74]. In the IEC/TC90 experiments, the coefficient of variation for samples mounted on FRP (standard deviation divided by the average value) was lower than 2% for $I_C$ measurements from 1 to 7 T [73].

### 3.4.3 Nb₃Sn

The increased sensitivity of Nb$_3$Sn to mechanical strain means that care must be taken when mounting samples to avoid degrading $J_C$ prior to measurement. The coil geometry is generally used. Nb$_3$Sn conductors should be reacted on a stainless steel reaction mandrel of a geometry that closely matches the sample holder. The surface of the reaction mandrel should be heavily oxidised to prevent any diffusion bonding between it and the conductor – 800 °C for 3 hours in air is usually sufficient. The wire should then be wound on the mandrel for the heat-treatment during which brittle Nb$_3$Sn A15 compound is formed. The sample should then be carefully transferred on to the sample holder taking care not to unduly strain the wire during this operation.

A G10-CR (US notation) (EP GC 201: European notation) or stainless steel measurement mandrel is often used. G10-CR (machined from plate) is similar to G11-CR (used for NbTi), but has a differential thermal contraction better matched to Nb$_3$Sn [40]. Other materials with similar thermal expansion properties to Nb$_3$Sn conductors are non-magnetic stainless steels, copper or non-magnetic copper alloys (see Fig. 3.4). As part of the VAMAS report, similar $I_C$'s as a function of magnetic field were found using G10 and stainless steel sample holders. Stainless steel has the advantage that it can be used for both the reaction and measurement, which eliminates

the need to transfer the sample. Vacuum grease was suggested as the bonding agent in the VAMAS test as it is easy to remove from the sample after use. Stycast (a high strength epoxy) was also tested and gave similar $I_C$'s for stainless steel and G-10CR sample holders [75]. The IEC/TC90 round-robin test on $Nb_3Sn$ composite conductors advised explicitly against using a solder bond on the stainless steel. Alumina ceramic can also be used as a dual-purpose mandrel/sample holder, either by itself or as a coating on stainless steel [72]. There is less chance of bonding between the holder and the conductor, but the thermal expansion is not very well matched.

In the VAMAS work on $Nb_3Sn$, the variation in $I_C$ was obtained from two intercomparisons. The first allowed each laboratory to use their own methods of measuring $I_C$, the second used the standard method using G10 and vacuum grease described above. The ratio of standard deviation to average value for the first intercomparison was 8.0% for $I_C$ defined at 10 $\mu Vm^{-1}$ measured at 12 T and 4.2 K. This fell to 2.2% for the second intercomparison using agreed mounting procedures [74].

### 3.4.4 BiSCCO

It is often not possible to wind high temperature superconducting tapes into coil form due to their brittle nature. Thus the most common measurements for high $T_C$ tapes use the short straight geometry. The results of the interlaboratory comparisons have been reported, some of which are included below [67].

Both G-10 and brass have been used as sample holders. However, it was reported that the sample was more likely to separate from the substrate when mounted on brass (due to differential thermal contraction) which can damage the samples. Hence the samples are best bonded to a G10 sample holder using a glass filled epoxy. Current contacts and voltage taps can be soldered directly to the sample using a low temperature solder. However, some damage inevitably occurs by soldering although successful measurements on short samples can be made by soldering the current leads and using silver paint/epoxy for voltage taps [76]. Methods used for mounting HTS conductors have been discussed [67]. Many BiSCCO conductors are not fully dense. For the Ag-sheathed BiSCCO tape it was observed that the thermal expansion was dependent on

thermal cycling, which was attributed to yielding due to an internal stress between the Ag-sheath and the BiSCCO(2223) filaments [36]. Cryogenic liquid can seep into the conductor during measurement. Under these circumstances it is essential to warm the sample slowly after measurement so the cryogen can escape without blistering the silver matrix [67].

In round robin testing, the coefficient of variation for a BiSCCO sample premounted by a central laboratory (NIST) were 4.4% (77 K) and 3.2% (4.2 K) [67]. The IEC/TC90 is in the process of developing a dc critical current test method for Ag-sheathed BiSCCO conductors [77].

## 3.5 Specialist techniques

### 3.5.1 Pulsed methods for $I_C$ measurements

The most common pulsed method involves increasing the current from zero to a predetermined level in 1-10 ms, measuring the voltage drop along the conductor and ramping back to zero again. The voltage is also measured before and after the pulse to allow for the subtraction of any offset. A series of pulsed measurements can be used to construct the superconducting $V$-$I$ characteristic [78]. Highly sensitive instruments with rapid response times are required for these measurements. An important advantage of the pulsed method is that if the current contacts are poor (highly resistive), they have limited effect on the measurement. This is because there is not sufficient time during the pulse for the heat to diffuse to the part of the conductor between the voltage taps. Measurements have also been performed using pulsed magnetic fields [79]. In this case a constant current is applied to the sample, and the voltage generated is recorded. This method has the advantage of allowing measurements to be taken up to the highest fields (>50 T). The rapid change in magnetic filed, however, causes eddy current heating which prevents accurate measurement of some samples.

### 3.5.2 Persistent mode experiments

The *V-I* characteristics can be found by measuring the decay of the current in a persistent mode coil [80]. A current is induced into a superconducting coil, and the decay of the self-field measured a function of time. The decay can be converted into an equivalent resistance for the conductor. This is presently the only method which gives measurements on long lengths of conductor down to an electric field of a few $pVm^{-1}$ relevant for NMR applications. Results obtained on NbTi and $Nb_3Sn$ are in broad agreement with a normal distribution of critical currents described using Eqns. 3.4 and 3.5.

### 3.5.3 $J_C(B,T)$ – Techniques

The variation of critical current as a function of temperature is critical in assessing conductors for cryogen-free applications and for many large scale systems for which forced flow helium is used. Over limited temperature ranges, vapour pressure thermometry is best used. With liquid helium, it is possible to vary the temperature between ~ 1.8 K and 5.22 K and with nitrogen from about 55 K to about 85 K. The temperature of the liquid is varied by controlling the vapour pressure of the gas above the liquid.

Techniques have also been developed to measure conductors in an isothermal environment so the temperature can be varied continuously over any temperature range above 1.8 K [81, 82]. Typically, the sample is in intimate contact with a copper thermal block that incorporates a heater and thermometry. A temperature controller maintains the temperature constant as the *V-I* characteristics are measured. Purpose built and commercial variable temperature cryostats can also provide the required isothermal environment. Both dc continuous and pulsed methods are used to obtain the *V-I* characteristics [83, 84].

### 3.5.4 $J_C(B,T,\varepsilon)$ – Techniques

As mentioned in the introduction, this thesis focuses on critical current measurements as a function of applied magnetic field, temperature and uniaxial strain. The review of these measurements will therefore be presented in chapter 5, rather than in this section. However, the critical current has also been measured as a function of transverse stress, and of uniaxial stress to evaluate the strength of the strand.

The effect of transverse stress on critical current has been measured previously [85-88]. The samples were placed between a fixed position pressure block and a movable pressure block. The stress is applied by compressing the sample. Although it is not possible to measure the strain in this configuration, it is possible to obtain equivalent stresses for uniaxial strains to allow direct comparison between measurements. The $V$-$I$ characteristics are measured at a series of different stresses. It has been demonstrated that the effect of transverse stress is critically dependent on how the stress is applied. If the stress is localised, the effect on $J_C$ is far more marked than if the stress is uniformly applied. This can be seen by comparing the degradation of $J_C$ between round and flat conductors [87, 89].

Critical current measurements have also been performed as a function of stress to estimate the strength of a conductor. In this case the sample was loaded to a certain stress level and then unloaded to zero stress at room temperature. The conductor was then cooled to 4.2 K and the critical current was measured. The variation of critical current as a function of repeated applied stress at room temperature has been measured and the strength distribution for the composite calculated [90].

## 3.6    Concluding comments

Although appearing to be simple, critical current measurements have an underlying complexity. It is essential that they are understood so that reliable measurements can be made and that there is a better understanding of the underlying science. This chapter has reviewed the relevant the techniques so that accurate measurements can be made. The relatively simple case of measuring $I_C$ as a function of magnetic field, with the

sample immersed in liquid cryogen, has been considered in detail with reference to the international effort to standardise test procedures for the main technological materials. Methods of analysis were presented and a distinction made between intrinsic and extrinsic properties of the wire. Specialist techniques for measuring $I_C$ were also reviewed.

# Chapter 4

# Preliminary Experiments on the Effect of Hot Isostatic Pressing on the Strain Tolerance of the Critical Current Density Found in Modified Jelly Roll Nb$_3$Sn Wires

## 4.1    Introduction

The measurements presented in this chapter were part of a larger project and served two purposes.  The first was to provide experience in using the strain probe in preparation for the variable temperature measurements presented in chapter 5.  Secondly, the mechanical properties and reversibility of the wire were investigated.  Unfortunately, there was not enough time to complete a comprehensive study, although the results presented in this chapter are interesting enough to warrant further exploration [91].

Modified Jelly Roll [92] (MJR) Nb$_3$Sn superconducting wires have several advantages over bronze processed multifilamentary wires.  They are generally easier to fabricate, and give more flexibility for the final configuration of the wire.  This flexibility in the design allows customised wires to be fabricated for different applications.  For high field applications, not only the magnitude but also the strain tolerance of the critical current density ($J_C$) is important.   Work has been reported on Hot Isostatically Pressed (HIP'ed) Nb$_3$Sn wires at low magnetic fields [93] between 3 T and 8 T which showed an improvement in the strain tolerance of $J_C$ that could potentially be repeated at higher fields.  It is known that Kirkendall voids are present near the grain boundaries in Nb$_3$Sn wires and that a high pressure reaction on reacted wires is sufficient to eliminate the voids [93, 94].   Furthermore, work on high temperature superconductors has demonstrated that $J_C$ can be increased by improving the current transport across grain boundaries.   These results have led us to consider whether HIP'ing can be used to improve the properties of MJR wires in high magnetic fields.

In this chapter an investigation into whether the critical current density of wires optimised at ambient pressure can be further improved by HIP'ing is presented. The effect of HIP'ing on the strain tolerance of the upper critical field is also reported.

The chapter is arranged as follows. Sections 4.2 and 4.3 describe the experimental procedure used and present the results obtained. The analysis in this chapter is presented in terms of a simple Kramer analysis [95]. Strictly, a more general analysis should be used such as that of Fietz-Webb [96] as will be presented for the data in chapter 5. However, the Kramer analysis has been successfully used to characterise $Nb_3Sn$ conductors under similar applied magnetic field, temperature and strain ranges [86, 97, 98], and so is used here. Section 4.4 uses this analysis and presents the results within the framework of a scaling law [99]. Finally the effects of HIP'ing on the critical current and scaling law parameters are discussed and the important conclusions drawn.



**Figure 4.1** A $Nb_3Sn$ superconducting strand soldered to a CuBe spring for critical current measurements as a function of magnetic field, temperature and strain.

## 4.2 Experimental

The wires examined in this study were 0.5 mm diameter internal-tin MJR wires with niobium diffusion barriers [100]. The wire was wound loosely on to a steel reaction mandrel with a 0.5 mm deep 60° V-groove. The mandrel had been subjected to a 3 hour pre-reaction heat treatment in oxygen in an effort to reduce diffusion bonding to it by the sample. The wires were reacted in argon at 1 atmosphere pressure using the manufacturers heat treatment procedure of 210°C for 100 h followed by 340 °C for 48 h and finally 650 °C for 180 h. The HIP'ed wire was then subjected to a further heat treatment of 750 °C for 6 hours in argon at 2000 atm.
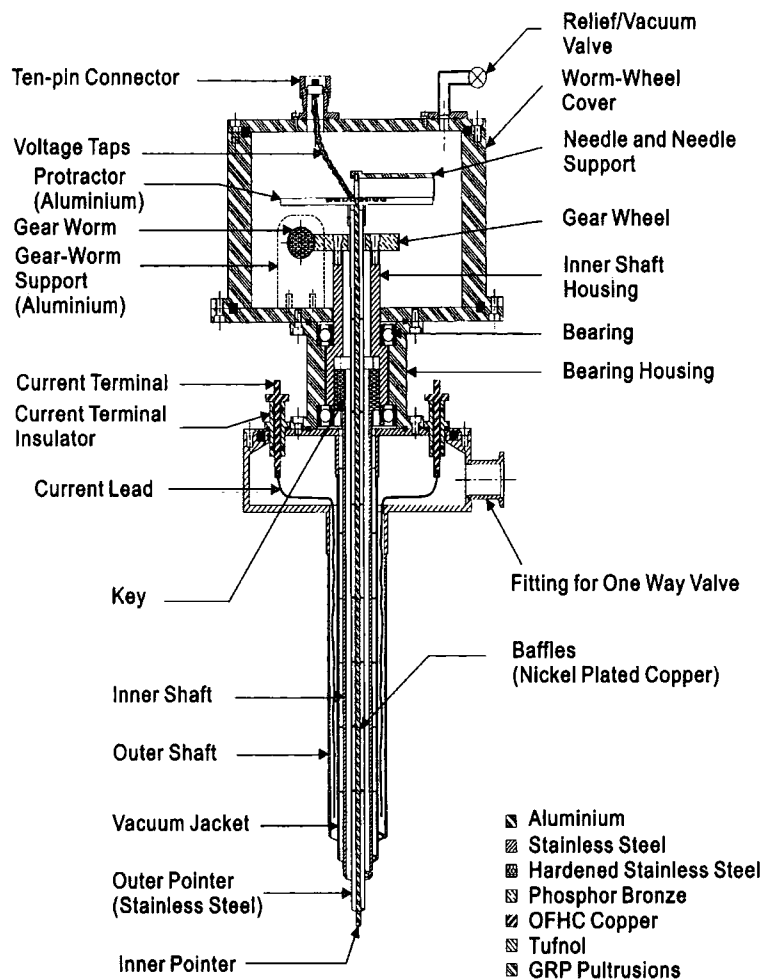


**Figure 4.2** Schematic diagram of the top part of the probe designed for $J_C(B,T,\varepsilon)$ measurements on superconducting wires and tapes. (Reproduced from Cheggour *et al.* [39].)

The reacted wires were then transferred on to a 2% beryllium doped copper alloy spring. The pitch on the spring was 6.35 mm so that the wire was orientated at an angle of 5.3° from perpendicular to the magnetic field. The spring and sample were partially electroplated with copper. The wire was then soldered to the spring in order to reduce Joule heating and to provide some protection for the wire against the Lorentz forces that occur during the measurement. A wire that has been soldered to a CuBe spring can be seen in Fig. 4.1.

To check the homogeneity of the wires, HIP'ed and unHIP'ed samples were also reacted directly on the critical current sample holders. This eliminated the need to transfer the sample after reaction so values of $J_C$ could be measured with little risk of handling damage.
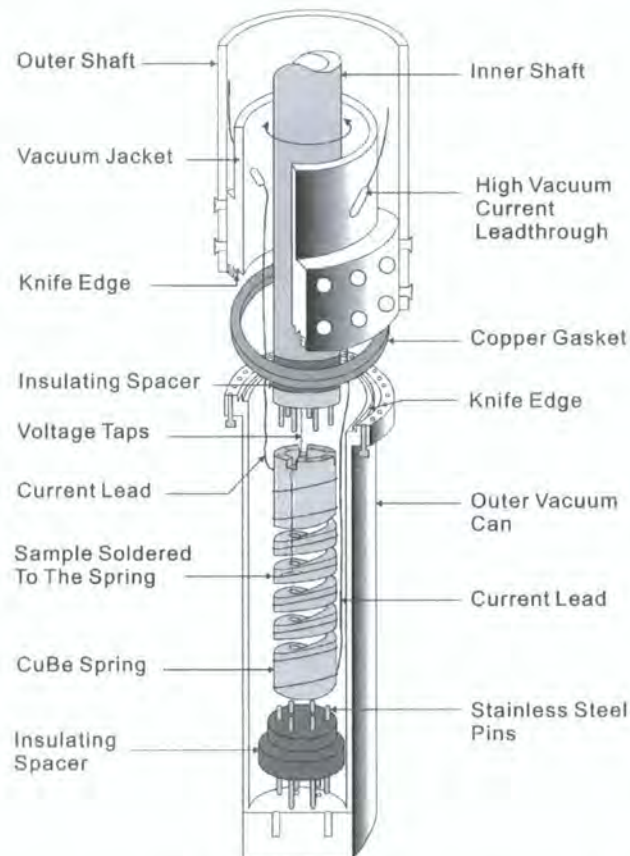


**Figure 4.3** Schematic diagram of the bottom part of the probe designed for $J_C(B,T,\varepsilon)$ measurements on superconducting wires and tapes. For measurements at temperatures of liquid cryogens, the outer vacuum can is replaced by a can with holes at the bottom. (Reproduced from Cheggour *et al.* [39].)

Measurements were performed using the variable temperature strain probe [39] at 4.2 K. Figs. 4.2 and 4.3 show schematic diagrams of the top and bottom of the probe respectively. To allow measurements to be performed at 4.2 K by direct immersion of the sample in liquid helium, the outer can shown in Fig 4.3 was replaced by one with holes in the bottom and the copper gasket is removed. The strain was applied to the sample by rotating the top of the spring relative to the bottom. The angular displacement of the top and bottom of the spring was then converted to strain from a previous calibration. For these measurements, the spring was calibrated from $-2.1\% \leq \varepsilon \leq 0.7\%$. The uncertainty in the strain values quoted is less than $10^{-4}$.

The critical current was measured using a standard 4-terminal resistance measurement at a criterion of 100 $\mu Vm^{-1}$. Current was provided using a 500 Amp power supply built in-house with an accuracy above 1 Amp of better than 0.25%. The voltage was measured using a Keithley 182 voltmeter with typical noise levels of $\pm$ 12 $\mu Vm^{-1}$. This leads to a typical uncertainty in generating $I_C$ at a criterion of 100 $\mu Vm^{-1}$ of 1% to 2%. The critical current was measured as a function of applied magnetic field at constant strain. The magnetic field was applied using a superconducting magnet providing fields up to 15 T. Once the variation of critical current with applied magnetic field was measured at one strain, the strain was changed, and the $J_C$ measurements repeated. The strain was initially increased from 0% to about 0.45% strain. The strain was then reduced back to 0% to investigate the reversibility of critical current under strain. The strain was then increased to 0.7% (which is the elastic limit of the spring) and reduced to 0% again. The increments of strain were 0.057%, so that a good description of the strain tolerance of the wire could be found, except in the final release of strain where measurements were performed at 0.63%, 0.23% and 0% strain.

## 4.3 Results
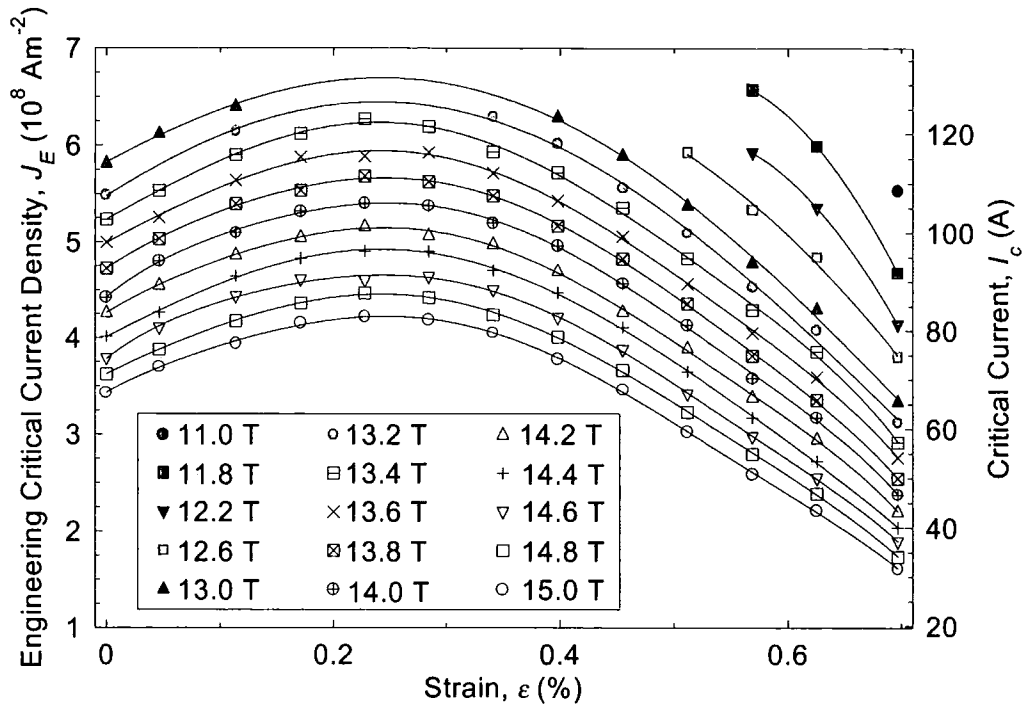


**Figure 4.4** Engineering critical current density as a function of strain and applied magnetic field for the unHIP'ed wire. Measurements were taken during the second increase in strain.
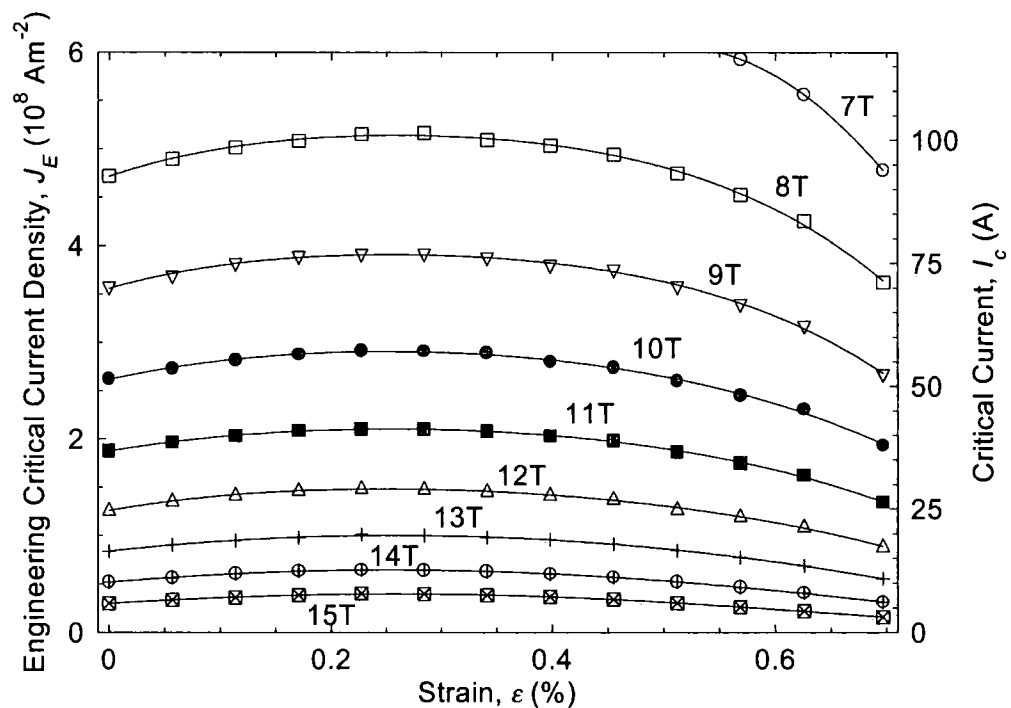


**Figure 4.5** Engineering critical current density as a function of strain and applied magnetic field for the HIP'ed wire. Measurements were taken during the second increase in strain.
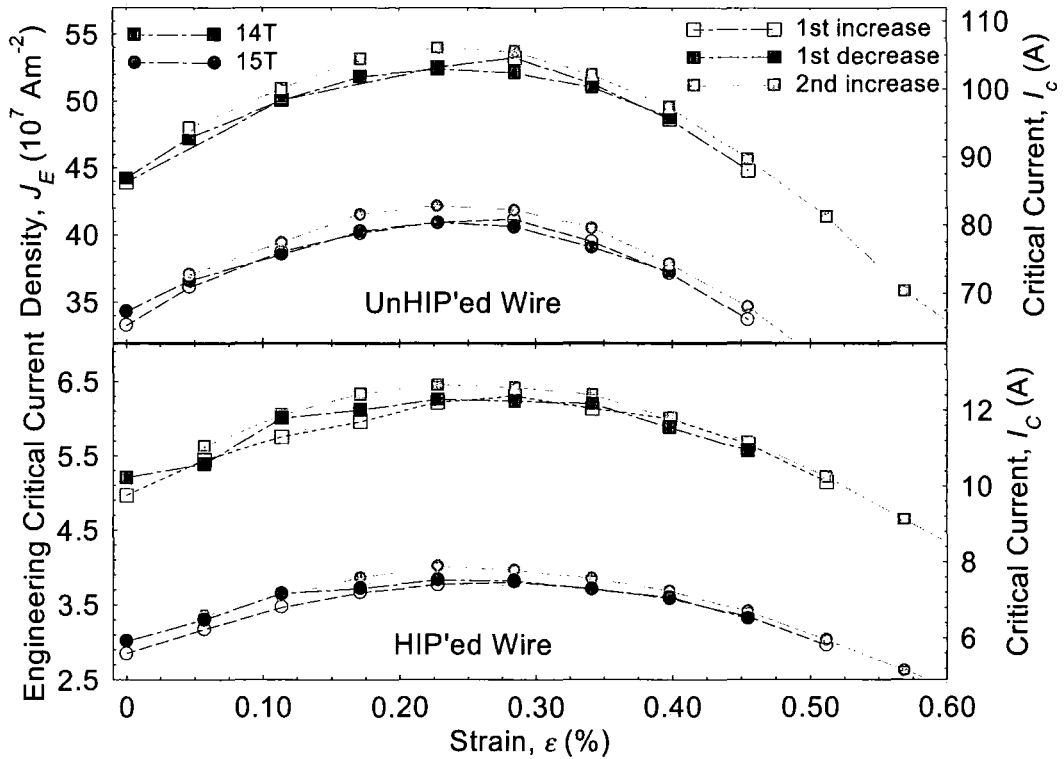
**Figure 4.6** Engineering critical current density as a function of strain for the HIP'ed and unHIP'ed wires. The data characterise the reversibility in $J_E$ at 14 T and 15 T.
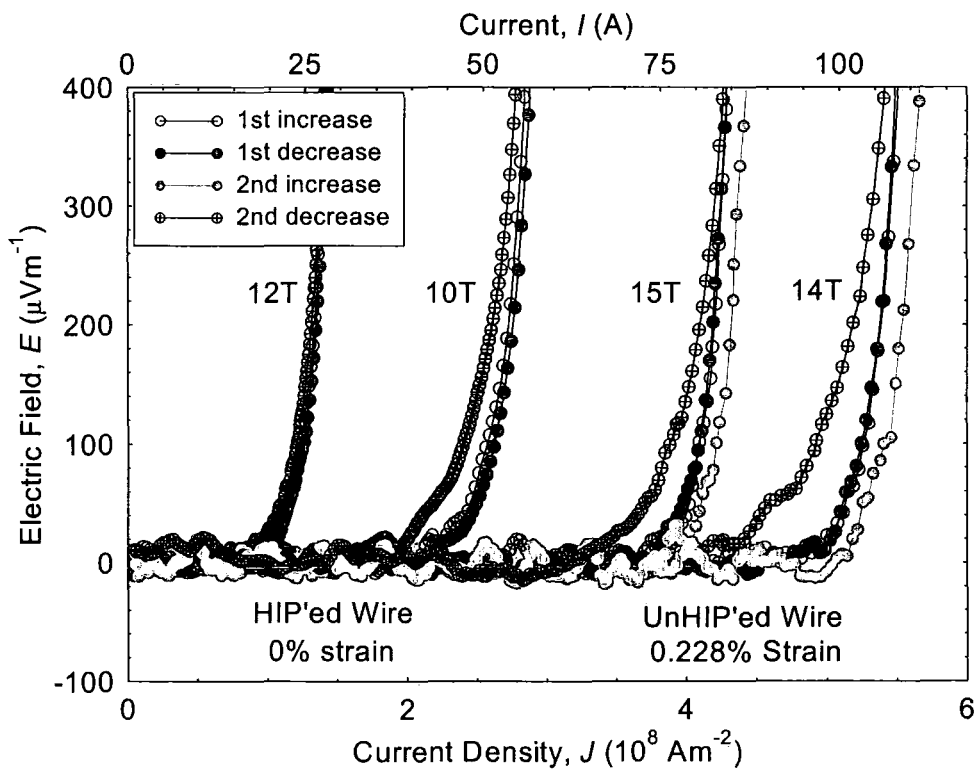


**Figure 4.7** Electric field-current density characteristics for the HIP'ed and unHIP'ed wires at the same strain for a given field during different strain cycles.

Figs. 4.4 and 4.5 show the engineering critical current density, $J_E$ (the critical current density for the entire wire), as a function of strain for the unHIP'ed and HIP'ed wires respectively. The data were both taken during the second increase of strain. It can be seen that the thermal precompression for the unHIP'ed wire is 0.23% and 0.27% for the HIP'ed wire. The variation in the critical current values for different sections of both the HIP'ed and unHIP'ed wires was about 10%. The critical currents measured for both types of wires on springs or reaction mandrels were in good agreement.

Fig. 4.6 characterises the reversibility of the critical current density at 14 T and 15 T as a function of strain. The clear symbols describe the first increase of strain, whereas the first decrease and second increase are represented by black and grey symbols respectively. It can be seen that the second increase in strain gives slightly larger critical current densities than the equivalent first cycle. However, the first cycle does appear to be almost reversible with applied strain in all cases. The reversibility is also evident in Fig. 4.7. This shows the electric field-current density characteristics at 10 T and 12 T for the HIP'ed wire as well as 14 T and 15 T for the unHIP'ed sample. The
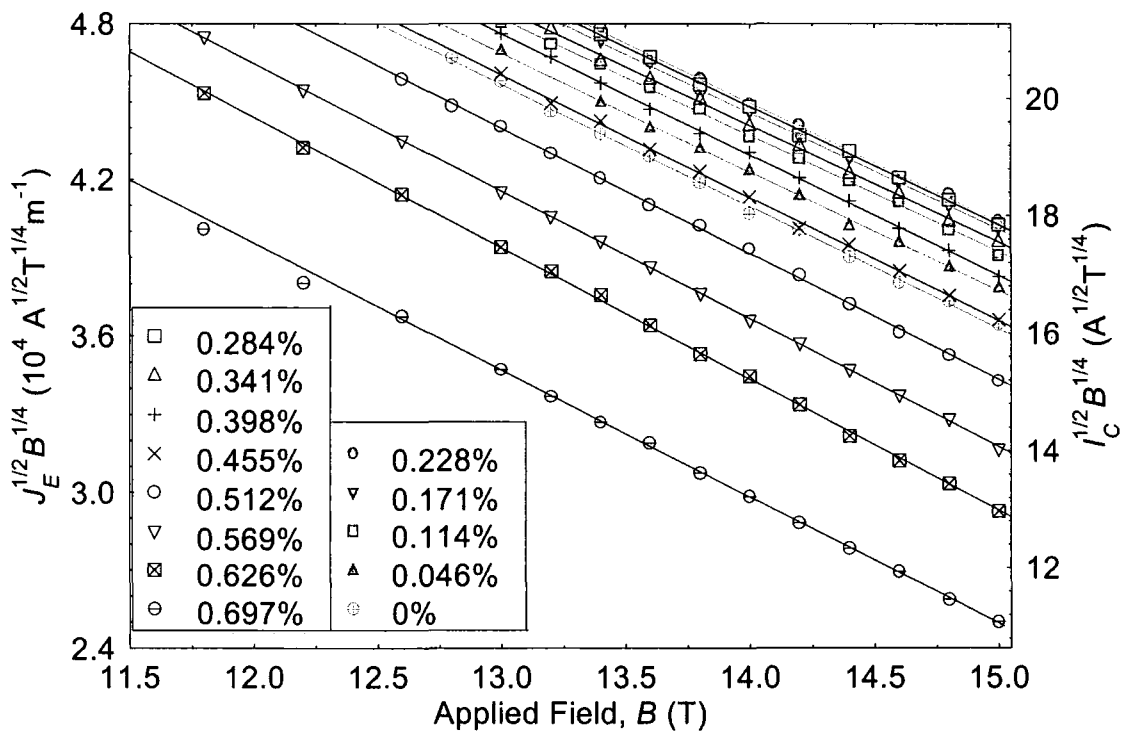


**Figure 4.8** Kramer plot for the unHIP'ed wire, from which $B_{C2}^{Kramer}$ and $F_{PM}$ are calculated. The data were taken during the second increase of strain.

first increase and decrease of strain overlap, confirming the reversibility seen in Fig. 4.6. Again, the second increase in strain has higher $J_E$ values than the first cycle, and a degradation in $J_E$ can be seen on the final decrease of strain. It is evident that the degradation is more noticeable at lower electric fields, and is larger at higher current densities.

## 4.4 Analysis

Fig. 4.8 shows a typical Kramer plot [95] for the unHIP'ed wire during the second increase in strain calculated from the data in Fig. 4.4. The data at each strain were fitted to a line of best fit so that values of upper critical field ( $B_{C2}^{Kramer}$ ) and maximum pinning force ($F_{PM}$) could be calculated. This fitting procedure was repeated for the HIP'ed wire.

The reduced upper critical field as a function of intrinsic strain for the first cycle and second increase of strain for both wires are shown in Fig. 4.9. The values of upper
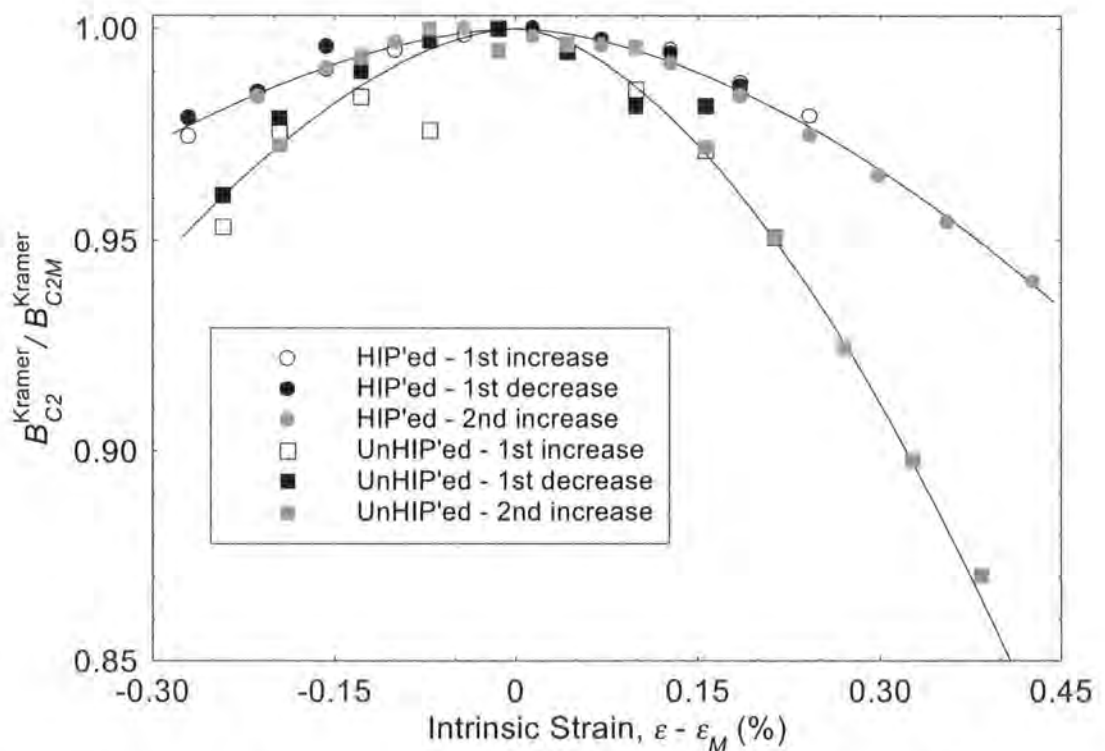


**Figure 4.9** Reduced upper critical field as a function of intrinsic strain for the HIP'ed and unHIP'ed wires.
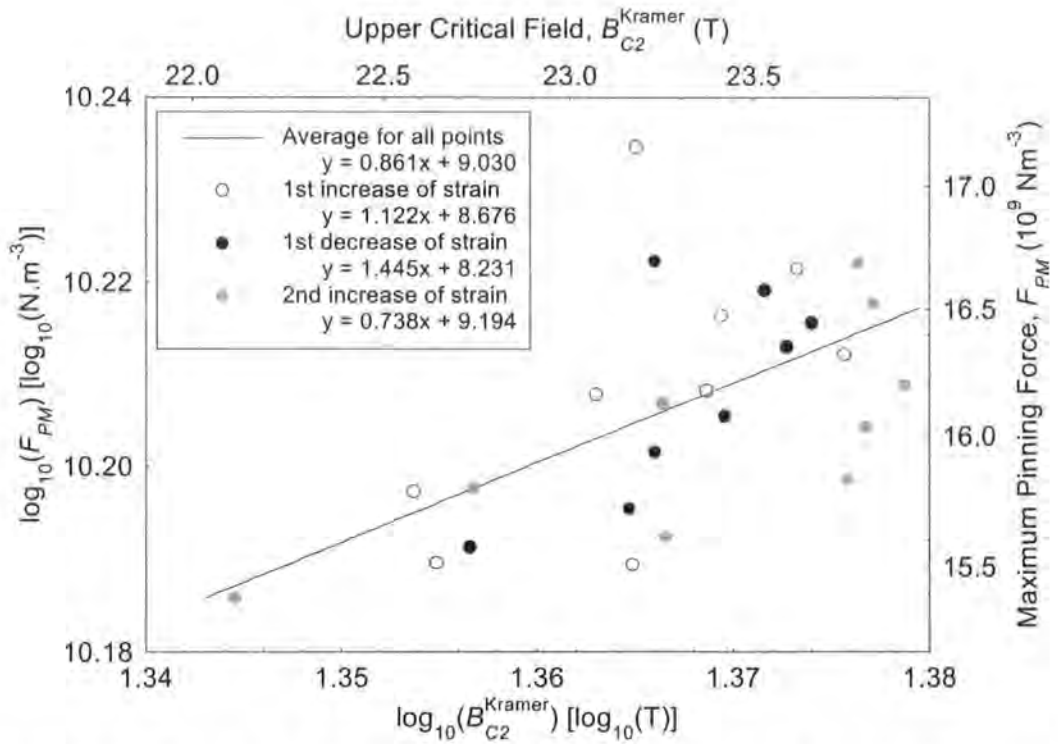
**Figure 4.10** A log-log plot of the maximum pinning force as a function of upper critical field for the unHIP'ed wire. The equations in the legend give best fits to the data.
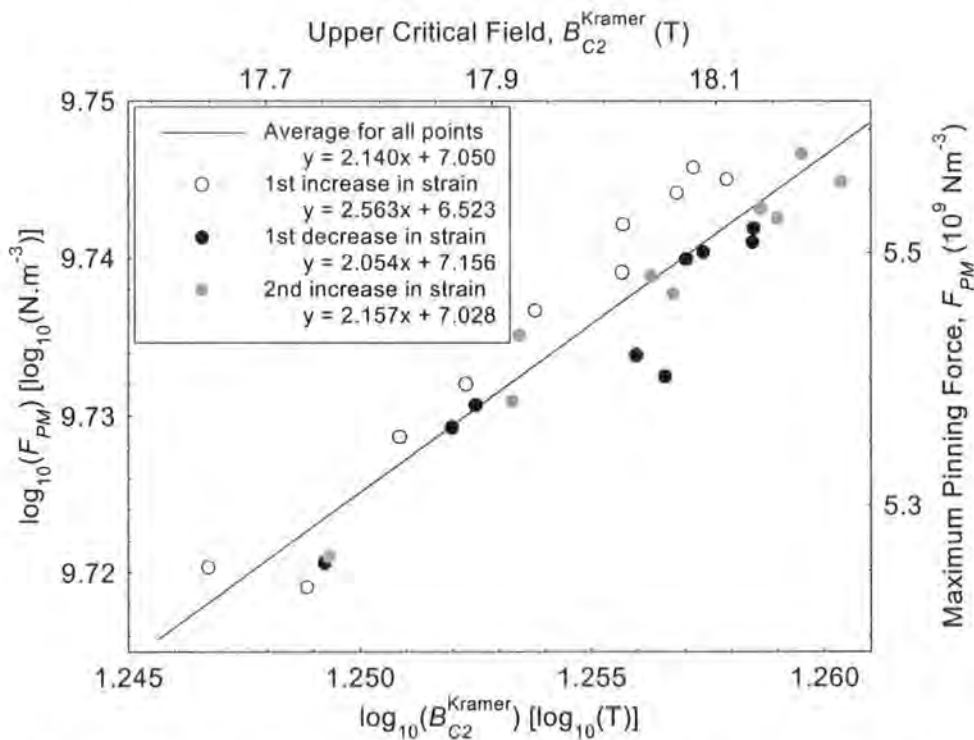


**Figure 4.11** A log-log plot of the maximum pinning force as a function of upper critical field for the HIP'ed wire. The equations in the legend give the best fits to the data.

critical field for the unHIP'ed and HIP'ed samples at the peak ($B_{C2M}^{Kramer}$) were 23.83 T and 18.13 T respectively. These values were measured during the first reversible cycle. Values for the second increase in strain were slightly higher.

Figs. 4.10 and 4.11 show log-log plots of the maximum pinning force as a function of upper critical field for the unHIP'ed and HIP'ed wires respectively. The data in Figs. 4.10 and 4.11 have been fitted to lines of best fit. For both samples, the two halves of the first strain cycle and the increase in strain data from the second cycle have been fitted separately as well as the average of all the data. From fitting to these data, the slope of the line for the unHIP'ed data is $0.861 \pm 0.241$, and for the HIP'ed data is $2.14 \pm 0.16$.

## 4.5    Discussion

The strains at which the critical current is maximum ($\varepsilon_M$) for both unHIP'ed and HIP'ed wires are very similar, having values 0.23% and 0.27%. These compare favourably with values reported in the VAMAS report of 0.2% and 0.21% for an internal tin wire measured at two independent laboratories [101]. The value of $\varepsilon_M$ remains constant for both wires regardless of whether the strain is increased or decreased, and is reproducible on the second increase of strain.

The increase in critical current density with the second increase of strain can be attributed to the composite nature of the wire. When straining the wire, some components deform plastically while others remain elastic. Thus, on returning to zero strain, the strain state for the wire may be changed from the original state causing a change in the critical current.

The electric field-current density characteristics give more direct evidence as to the irreversibility of the wires. The first increase and decrease of strain show that the critical current is reversible, no matter what electric field criterion is used. The increase in critical current observed on the second increase in strain is found irrespective of criterion used. The degradation of critical current during the second decrease of strain is a dependent on electric field criterion. A smaller $E$-field criterion leads to a larger

difference between that critical current observed and that found during the first increase of strain. The index ($N$) of transition, given by $E = \alpha J^N$, is smaller because there is a resistive region that appears in the trace before the wire goes through the complete superconducting transition. This effect is less apparent at low currents as shown by the 12 T characteristics for the HIP'ed wire that almost overlap. This suggests that after the cycle to 0.7%, the wire was damaged in some way, and this smaller index of transition is due to a transfer current or heating effect. This feature is seen on the characteristics of not only the unHIP'ed wire, but also the HIP'ed wire. By comparing $E$-$J$ characteristics at 0.63% strain when it was increased to and decreased from 0.7%, a similar change in the index of transition was noted suggesting most of the damage was done above 0.63%. This also suggests that the HIP'ing reaction did not improve the ultimate tensile strain of the wire.

The strain tolerance of the reduced upper critical field for the HIP'ed wire is greater than that of the unHIP'ed wire. The scaling law [99] for $B_{C2}^{\text{Kramer}}$ and the volume pinning force $F_P$ is:

$$B_{C2}^{\text{Kramer}}(\varepsilon) = B_{C2M}^{\text{Kramer}}\left(1 - a\left|\varepsilon - \varepsilon_M\right|^u\right) \tag{4.1}$$

$$F_P \propto \left[B_{C2}^{\text{Kramer}}(\varepsilon)\right]^m f(b) \tag{4.2}$$

where $B_{C2M}^{\text{Kramer}}$ is the maximum upper critical field, and $f(b)$ is a function of the reduced critical field only. Using $u = 1.7$ in Eqn. 4.1, fits were made to the data shown in Fig. 4.9. The resulting values for the constant $a$ are reported in Table 4.1 along with values reported by Ekin [99] for comparison.

| Sample | $a$ ($\varepsilon < \varepsilon_M$) | $a$ ($\varepsilon > \varepsilon_M$) |
|---|---|---|
| unHIP'ed | 1126 | 1640 |
| HIP'ed | 530 | 623 |
| Ekin [99] | 900 | 1250 |

**Table 4.1** Strain scaling law parameter compared with Ekin's results.

As can be seen from Table 4.1, the unHIP'ed sample was more strain sensitive than the samples measured by Ekin. The HIP'ed sample was less strain sensitive. The reduced sensitivity of the reduced upper critical field to strain is important for improving applications. If the HIP reaction could be optimised so that the critical current density, and upper critical field of the wire remained close to unHIP'ed values, but the tolerance to strain was improved as reported here, further enhancements of wires for high field and large scale applications may be achieved.

Ekin found that variable strain data were parameterised by $m = 1$ for $Nb_3Sn$ in the scaling law for $F$. From data in Fig. 4.10, it can be seen that $m = 0.861 \pm 0.241$ for the unHIP'ed sample which is in agreement with the data of Ekin. However the HIP'ed sample has $m = 2.14 \pm 0.16$. Data obtained at variable temperature lead to typical values for $m$ of between 2 and 3.5. Therefore the value of the $m$ found in the scaling law for the HIP'ed sample is more like the values obtained from variable temperature data. We suggest that the closing of the voids associated with the HIP treatment probably causes this change in $m$. These results may help provide a more complete description of the scaling law, and the relationship between variable temperature and variable strain data.

## 4.6  Conclusions

The critical current density of HIP'ed and unHIP'ed $Nb_3Sn$ Modified Jelly Roll superconducting wires has been measured as a function of magnetic field and strain at 4.2 K. The critical current was shown to peak at a maximum strain of 0.23% and 0.27% for the unHIP'ed and HIP'ed wires respectively, in close agreement with the VAMAS report. The critical current was also shown to vary irreversibly with strain for both HIP'ed and unHIP'ed wires, with reversibility only being seen over one cycle in strain. The critical current density and upper critical field of the wire have decreased after HIP'ing. The reduced upper critical field derived from Kramer plots was found to be less strain sensitive for the HIP'ed wire than for the unHIP'ed wire. By considering the maximum pinning force as a function of upper critical field, the form of the scaling law has been evaluated. The index ($m$) was found to be 0.861 for the unHIP'ed wire which increased to 2.14 for the HIP'ed wire. We suggest this is probably due to the closing of the voids during the HIP reaction.

# Chapter 5

# The Strain and Temperature Scaling Law for the Critical Current Density of a Jelly Roll Nb₃Al Strand in High Magnetic Fields

## 5.1    Introduction

At present, $Nb_3Sn$ conductors are the materials of choice for high field applications above 12 T.    Although it has been long understood that stoichiometric $Nb_3Al$ and $Nb_3(AlX)$ (X=Ge or Cu) have superior critical temperature ($T_C$) and upper critical field ($B_{C2}$) to $Nb_3Sn$ [102-106], only recently have fabrication techniques improved sufficiently for $Nb_3Al$ to emerge as a practical alternative to $Nb_3Sn$. $Nb_3Al$ conductors offer the potential for less sensitivity to stress (the Young's modulus is about a factor of 2 higher), strain [107-111] and have similar sensitivity to neutron irradiation [112]. Long lengths of the $Nb_3Al$ conductor investigated in this work have been mass-produced within the framework of the International Thermonuclear Experimental Reactor (ITER) Engineering Design Activity (EDA) [113].   The conductor contains off-stoichiometric $Nb_3Al$ with slightly lower critical parameters than $Nb_3Sn$.   Nevertheless, because strain tolerance is at a premium in large scale systems (particularly if they are fabricated using react-and wind techniques [114]), the engineering critical current density ($J_E$) is now sufficiently high to make the strand a candidate for large-scale fusion systems.

To properly optimise the design of high field magnet systems, the strain tolerance of the conductor must be known.   Large Lorentz forces strain the conductor when the system is energised as does the differential thermal compression between component parts of the strand and/or cable on cooling it to cryogenic temperatures.   In most of literature on the strain tolerance of technological conductors, the sample is measured when immersed in a cryogenic liquid including the work on $Nb_3Sn$ [99], NbTi [115, 116], $PbMo_6S_8$ [117, 118], YBCO [119], and BiSCCO [120-123].    However with the increasing importance of cryocooled and cable-in-conduit systems which operate over a range of temperatures, design engineers need to know how the strain tolernace of conductors in

high-fields changes as function of temperature. Such combined variable-temperature, variable-strain measurements of $J_E(B,T,\varepsilon)$ have been reported for Nb$_3$Sn [97, 98, 124] and recently proven useful in providing a unified scaling law for $J_E(B,T,\varepsilon)$ in a small diameter (0.3 mm) Nb$_3$Sn wire [108, 125]. Measurements on Nb$_3$Al are less extensive. High-field variable temperature data (at constant strain) [83, 126, 127] or variable strain data (at constant temperature) [110, 111] have been reported. To the authors knowledge, this is the first report of detailed $J_E(B,T,\varepsilon)$ data for a technological Nb$_3$Al conductor.

The critical science that underpins $J_E$ in A15 superconducting materials such as Nb$_3$Sn and Nb$_3$Al is still not properly understood. The semi-empirical Fietz-Webb [96] scaling law for the pinning force, $F_P = J_E B = A\,[B_{C2}(T)]^n b^p (1-b)^q$ where $p$ and $q$ are constants, has proven useful to parameterise $J_E$ data. However the free parameters are strongly correlated. For example, data presented in this work show that a change in $B_{C2}$ of only 1 T can cause $p$ and $q$ to double. In the literature there have broadly been three approaches to break the correlation, in part driven by the experimental challenges of the measurements. Firstly, $p$ and $q$ have been constrained at the Kramer values [95] $p = 0.5$ and $q = 2$. This widely used approach has been successfully used to parameterise both variable-temperature and the variable-strain data on technological Nb$_3$Sn and Nb$_3$Al conductors where $B_{C2}$ is typically 25 – 30 T [86, 91, 97, 98, 128-130]. However, because this approach generally completely ignores the low $J_E$ data at the highest fields, it is not clear to what degree this parameterisation is valid or unique. Secondly, resistivity measurements have been used to measure and $T_C^p(\varepsilon)$ and $B_{C2}^p(0,\varepsilon)$ directly and $p$ and $q$ treated as free parameters to describe the $J_E$ data [124, 127]. Detailed measurements have been reported on a high bronze-Nb$_3$Sn monofilament at high temperatures where $B_{C2}$ is relatively low. Whether this approach can be used for technological conductors is not yet clear. Thirdly all possible values of $p$ and $q$ are considered. Usually $J_E$ data are measured over as broad a field range and as close to $B_{C2}$ as possible and then fitted [99, 125]. This generally provides an accurate parameterisation of the high field tail. However, it unclear how to interpret the non-half-integral values of $p$ and $q$. In the work presented here, a comparison between these different approaches is provided and their relative merits explained.

In this chapter, engineering critical current measurements and complementary resistivity measurements as a function of magnetic field, temperature and strain are presented on a technological Nb$_3$Al strand. Section 5.2 presents the experimental procedure used to prepare and measure the Nb$_3$Al strands. Improved temperature control allows the measurements to be performed up to 200 A at 4.2 K, and 80 A at temperatures above 4.2 K to a stability of ± 5 mK, with an overall uncertainty in temperature of 100 mK. Improvements in the electric field sensitivity resulting in a typical noise level of 1 µVm$^{-1}$ allow reliable measurements of the index, $N$ [1], of the $E$-$J$ transition (where $E = \alpha J^N$). The strain range is from −1.8% to 0.7% provided by a helical bending spring [86, 131], rather than free-standing axial tension measurements [99, 132], so large compressive strains can be applied to vary the fundamental properties and test for scaling of $J_E$ in the conductor as extensively and critically as possible. The results from these measurements are presented in section 5.3 along with a comparison with other data in the literature.

In order to analyse this work, two different approaches have been taken. Initially, a technological fit that includes part of the high field tail is presented in section 5.4. This accurately parameterises the data above 1 A and is useful for high field applications such as the ITER coils. A single unified temperature and strain scaling law is presented in section 5.5, which includes a self-consistent interpretation of the tail in the context of accurate scaling and can be used to address the underlying mechanism that determines $J_E$. A discussion of this work is presented in section 5.6 with the summary and conclusions drawn in section 5.7.

---

[1] The symbol, $n$, is often used in the literature to denote both the index of transition of an $E$-$J$ measurement, and the exponent of $B_{C2}$ in the flux pinning scaling law. In order to avoid confusion, in this thesis, $N$ is used for the index of transition, and $n$ in the flux pinning scaling law.

## 5.2 Experimental

### 5.2.1 Sample preparation

The strands measured in this study were Sumitomo Cr-plated jelly roll $Nb_3Al$ strands of 0.81 mm diameter [113, 133]. The strands contain 96 filaments of 54 µm diameter and have a Cu to non-Cu ratio of 1.4. A micrograph of the cross-section of the strand is shown in Fig. 5.1. The strands were heat-treated in a high homogeneity furnace at 750 °C for 50 hours. This reaction was performed in a high purity argon atmosphere with the samples mounted on a stainless steel (type 316) mandrel. Temperature was monitored during the reaction using a compensated Type N thermocouple that provided an estimated accuracy of ± 4 °C.

Electrical transport measurements were made using a copper beryllium spring sample holder. In order that the strand could be soldered to the CuBe spring, the chrome plating was removed from the strand by etching in an ultrasonic HCl bath for
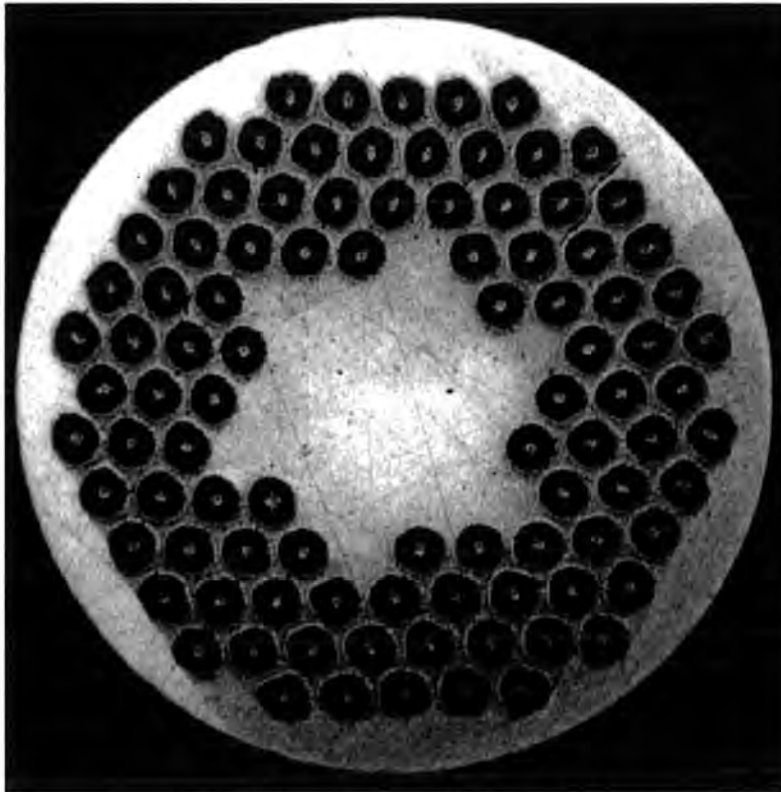


**Figure 5.1** Cross-sectional view of the $Nb_3Al$ strand [113, 133].

approximately 3 hours. The reaction mandrel was then attached to the CuBe spring and the sample was carefully transferred on to the spring. The surface of the spring was then partially electroplated with copper using a copper sulphate/sulphuric acid bath. This closed up any gaps between the strand and the spring and provided a current shunt to protect the strand from burn-out during critical current testing. Typically, a current of 180 mA for 20 hrs deposited sufficient copper. Finally the sample was soldered to the spring and current leads and voltage taps attached.

### 5.2.2 Measurement procedure

### 5.2.2.1    Experimental apparatus

Critical current ($I_C(B,T,\varepsilon)$) measurements and resistivity measurements to obtain the upper critical field ($B_{C2}^\rho(T,\varepsilon)$) were performed. The basic principles of the probe design and measurement have been described in detail elsewhere [39]. Schematic diagrams of the original design of the probe are shown in chapter 4 in Figs. 4.2 and 4.3. A helical bending spring based on the design of Walters *et al.* was used to apply strain to the sample [131]. An example of such a spring used in this experiment can be seen in Fig. 4.1. Tensile and compressional strain was applied to the sample by twisting the spring on which the sample was mounted. The uncertainty in the strain values is quoted is less than $10^{-4}$.

A helical bending spring has several advantages over short-length sample measurements [86, 99, 124]. Firstly the longer measuring length allows lower $E$-field sensitivity to be achieved. Indeed, recently we have reported measurements with a noise of $\sim 0.2\ \mu Vm^{-1}$ [134]. The voltage taps are well separated from the current leads, which minimises current transfer voltages that arise from the current not fully having transferred from the matrix into the filaments [25]. A typical current transfer length for a $Nb_3Sn$ conductor is $30d$, where $d$ is the diameter of the conductor [27] although in short-length sample measurements first-order corrections can be made if necessary [44]. Furthermore the concerns that arise as to whether the measurements are representative of the strand in operation, if the measurement length is less than the twist pitch (typically 10 mm) of the filaments in the strand are avoided.

CuBe was used for the spring rather than Ti [131], Ti coated with Cu and a Ag/Cu solder [98] or brass [86]. CuBe has a high limit of elasticity, matches reasonably well the coefficient of thermal expansion of many A15 conductor composites (which often include copper for electrical and thermal stability and require bronze) [39] and can be soldered to directly. When the sample is soldered, it has the advantage over freestanding samples [99, 124] of allowing both tensile and compressive measurements [86, 131] but requires additional measurements or calculations to determine the strain-free state. If the sample is only soldered at the ends of the spring but not soldered in the central (voltage tap) region, measurement of the torque applied allows one to determine the properties of the strain-free state directly by measuring $J_E$ just prior to the sample tightening significantly on the spring [135]. Although the (tensorial) strain applied is different in free-standing measurements and spring measurements, comparison of data obtained from different techniques shows that to first order the strain dependence of the critical current in the different configurations is the same. Furthermore we suggest that the spring geometry offers a more realistic configuration for the strain present in high field magnets.

In the probe, the spring is situated in an isolated enclosure that incorporates high current lead-throughs [136] to enable variable temperature measurements [81]. A copper gasket seal maintains the vacuum integrity of this environment and sustains the applied torque [39]. The spring design also facilitates accurate temperature control by separating the current transfer regions, where heat is generated, from the section of strand measured.

### 5.2.2.2    Improvements to the strain probe and overall accuracy

The current carrying capacity of the probe has been increased by adding more superconductor, brass and copper to the original leads. Thick brass current leads [30] were used at the top of the probe where the temperature varies from room temperature to 4.2 K. The cross sectional area of the brass for each lead was 100 mm$^2$, and incorporated four 0.3 mm diameter Cu/Ni NbTi wires soldered in parallel along the entire length. The brass leads were connected to the external current terminals by eight 1 mm diameter copper wires, and at the bottom to the high current lead-throughs (into the isolated variable temperature enclosure) by four 1 mm diameter copper wires and

(a)

(b)

Groove for
Current
Flylead

OFHC Copper

Ag/BiSCCO
Tape

Groove for
Current
Flylead

(c)

Spring

Cernox
Thermometer

Strand

Tufnol
Spacer

OFHC Copper
Sections Each
With a 17 W
Constantan Wire
Heater

Stainless Steel
Spacers
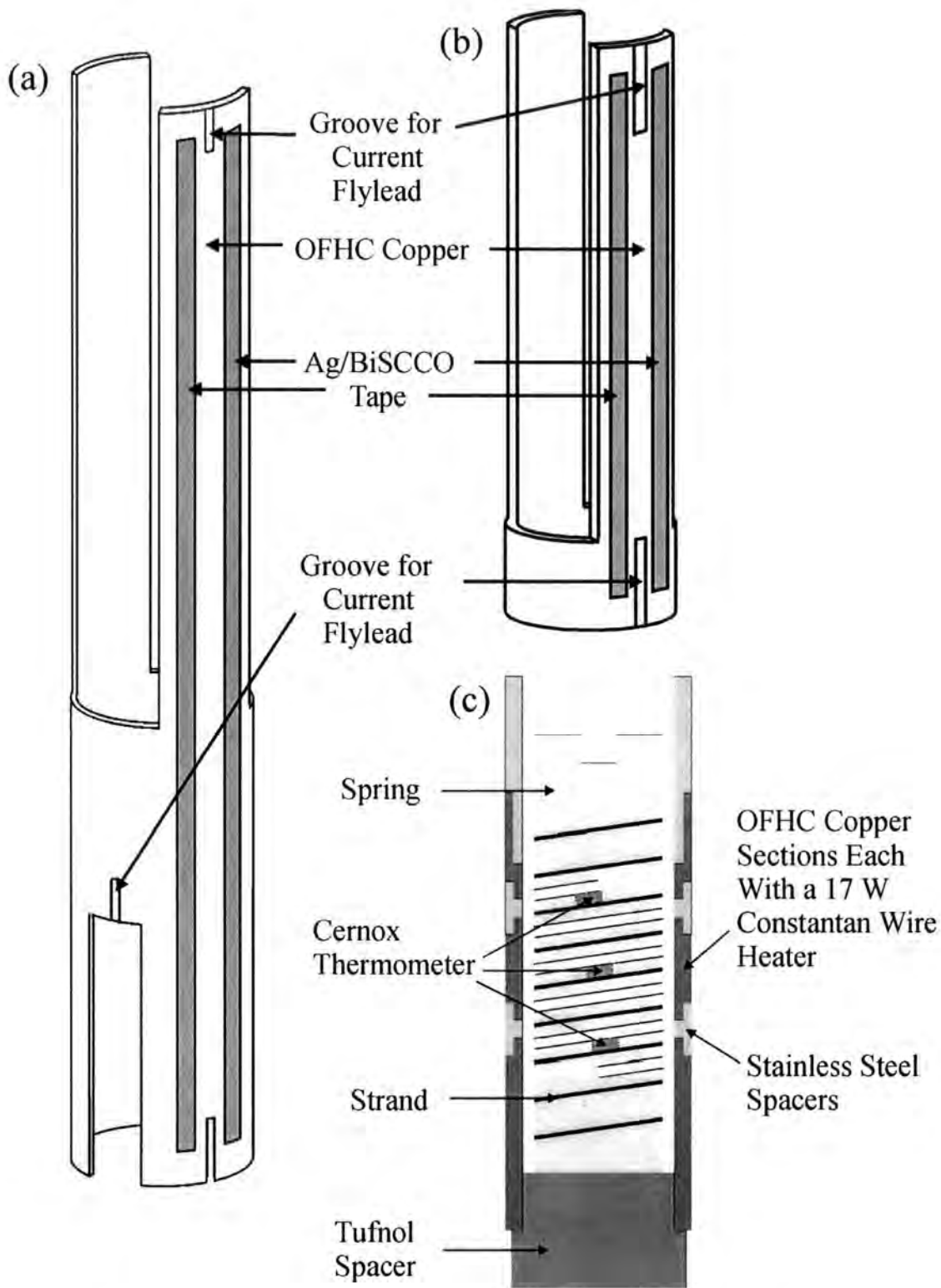
**Figure 5.2** Modifications made to the variable temperature strain probe below the high vacuum leadthrough. (a) is the outer current lead, (b) the inner current lead and (c) describes the changes made to the heater and the positioning of the Cernox thermometers.

Current Flylead

Inner Current Lead

Current Flylead

Cernox Thermometers

Heater

Current Flylead

Inner Shaft

Outer Vacuum Can

Electrical Connection Leadthrough

Spring and Sample

Outer Current Lead

Insulating Spacer

$\theta$
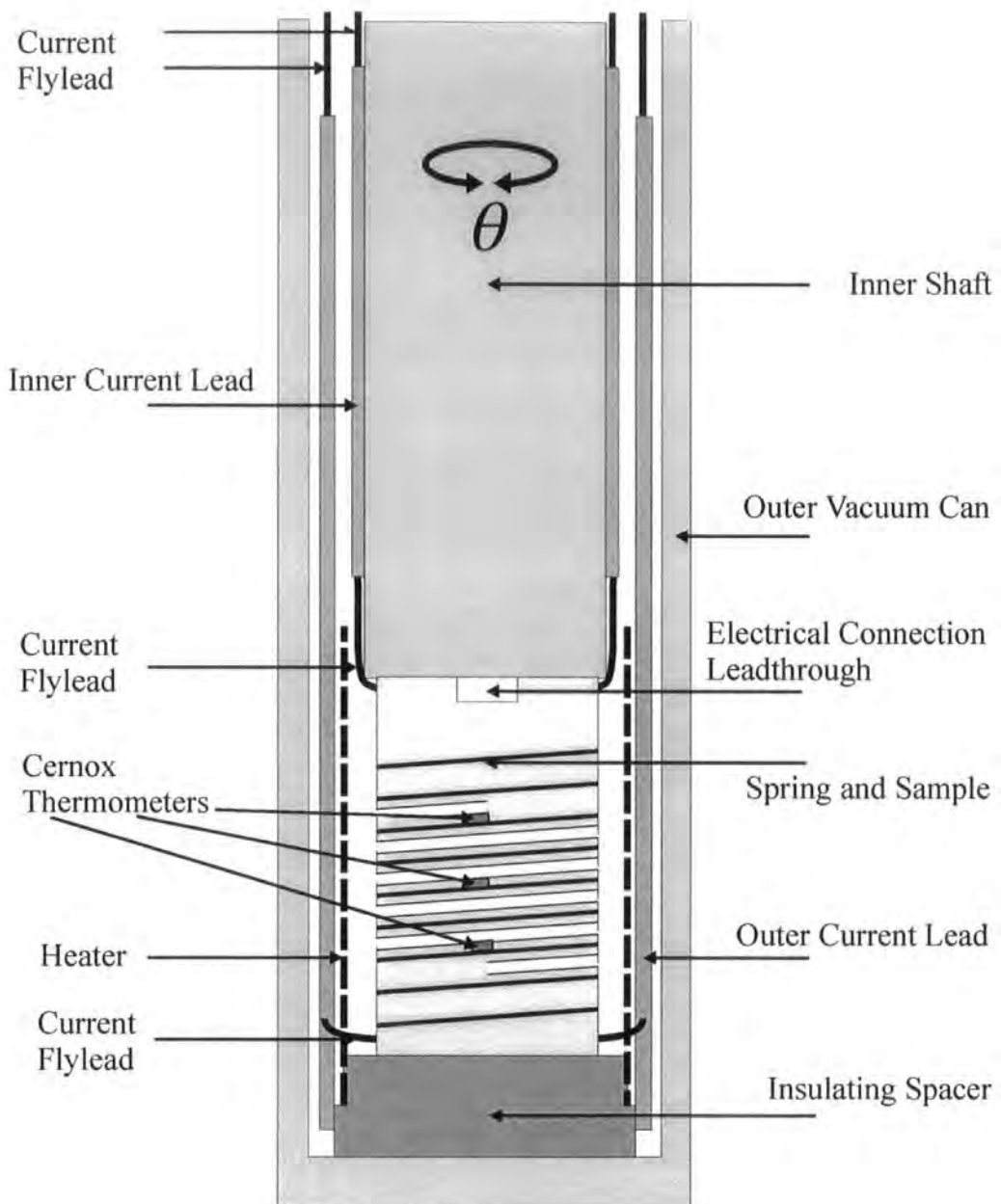
**Figure 5.3** Schematic cross sectional diagram of the bottom of the variable temperature strain probe showing how the modifications were implemented.

four 0.36 mm diameter Cu NbTi wires soldered in parallel. Below the lead-throughs two thicker oxygen-free high-conductivity (OFHC) copper cylindrical current leads were used in the enclosure to reduce heating around the spring. These are shown schematically in Fig. 5.2(a) and (b). Four Ag-sheathed BiSCCO tapes were soldered in parallel on both cylindrical current leads to further reduce heating. The cylindrical

current leads were connected to the spring and the high-current lead-throughs using 4 short lengths of 0.8 mm diameter copper wire per current lead. The positioning of the current leads in the region of the spring is shown in Fig 5.3.

To improve the temperature control during the measurements, three Cernox thermometers, which were all calibrated commercially in zero field, were mounted directly along the strand on the surface of the spring as shown in Figs. 5.2(c) and 5.3. Although these thermometers have low magnetic field dependence, there is typically an 80 mK correction at 4.2 K in magnetic fields up to 10 T [137-139]. The central control thermometer was calibrated in-house in fields up to 15 T at temperatures between 4.2 K and 20 K, as shown in Fig. 5.4 and the field-dependence accounted for in setting the
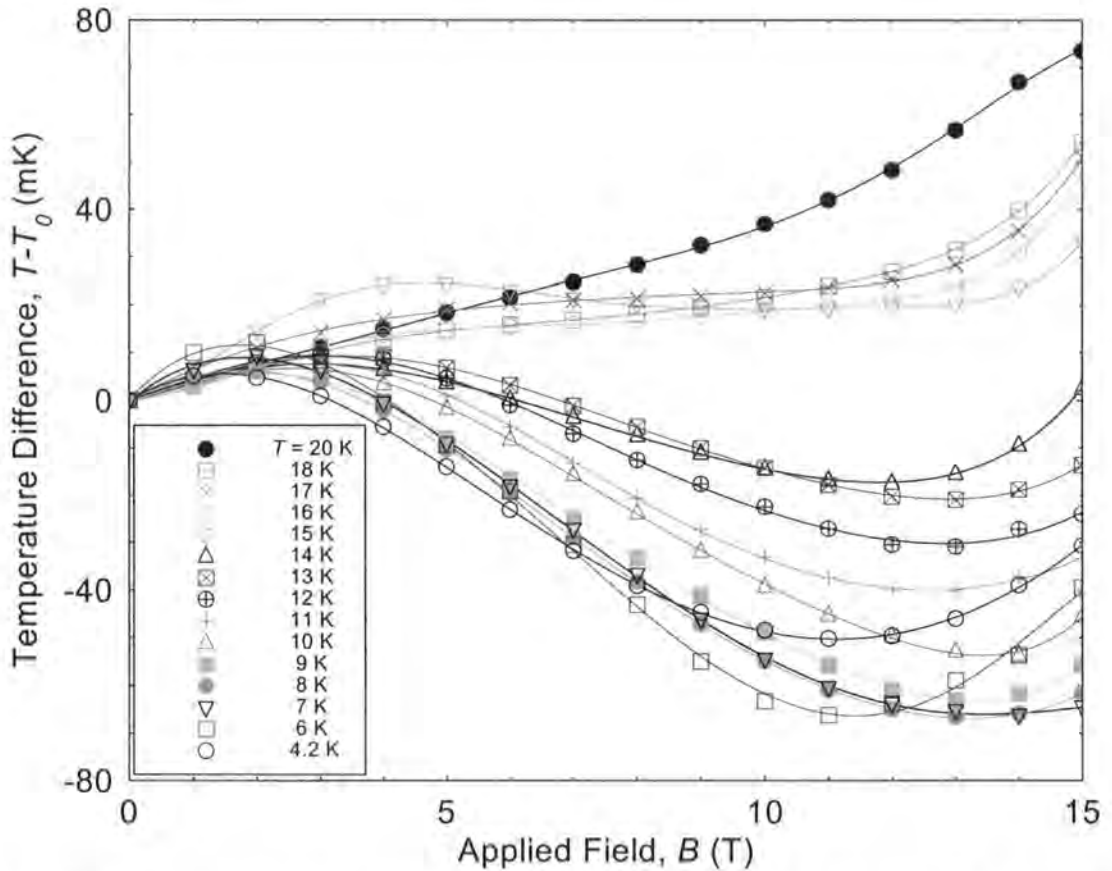


**Figure 5.4** Temperature correction as a function of applied magnetic field for the Cernox thermometer used to control the temperature for measurements above 4.2 K. $T_0$ is the temperature of the thermometer in zero magnetic field. The lines are guides to the eye.

temperature. The temperature along the sample was set using three independent heaters positioned concentrically about the spring as shown in Fig 5.2(c). The stability of the temperature during both critical current and resistivity measurements is estimated to be < 5 mK. The improved temperature control and new current leads facilitate measurements of currents up to ~ 200 A at 4.2 K and ~ 80 A at temperatures above 4.2 K, although the static boil-off of the probe has now increased by about 15 %. It is estimated that the overall accuracy of the probe is equivalent to an uncertainty in temperature of ± 100 mK. At 4.2 K, the strand is immersed directly in liquid helium with commensurately smaller overall errors.

### 5.2.2.3 Experimental method

The data acquisition followed a standard procedure [22, 71]. At fixed magnetic field, temperature and strain, the current through the sample was slowly increased and the voltage across the sample monitored using a standard four-terminal $V$-$I$ configuration. When the $V$-$I$ transition had been recorded, $I_C$ was extracted at a criterion of 10 $\mu$Vm$^{-1}$ or 100 $\mu$Vm$^{-1}$ and $J_E$ calculated and stored digitally. The measurement was then repeated as a function of magnetic field. Thereafter the temperature was changed and $J_E$ remeasured throughout the field range. The current flow direction ensured that the Lorentz force pushed the strand into the sample holder. Typical noise levels were ± 1 $\mu$Vm$^{-1}$. When the upper critical field ( $B_{C2}^{\rho}(T,\varepsilon)$ ) was less than 15 T, the resistivity was measured as a function of field at different temperatures. A lock-in amplifier was used to provide the excitation current, at 76 Hz, and measure the generated voltage. Three different currents were used to measure the resistivity - 82 mA, 28 mA and 6.5 mA. The strain was then changed and $J_E$ and resistivity measured again as a function of field and temperature. This process was repeated to obtain $J_E$ and $B_{C2}^{\rho}(T,\varepsilon)$ in the strain range from –2.1% to +0.7%.

Critical current measurements were made in decreasing magnetic field at 4.2 K on the first strand (Strand A) and from 6 K up to 14 K in 2 K steps on a second strand (Strand B). Resistivity measurements were made every Kelvin from 5 K to 16 K. Measurements were also made with the strand in the normal state so that the non-

superconducting current flowing through the strand and the electroplated spring (i.e. the shunt) could be determined as a function of field, temperature and strain. All currents quoted in this chapter have had this current (typically 25 mA at 10 $\mu$Vm$^{-1}$) subtracted from the total current measured in order to calculate the current in the superconductor alone [22].

## 5.3    Results

### 5.3.1  Critical Current Measurements

Figure 5.5 shows typical electric field-current density ($E$-$J$) characteristics as a function of applied magnetic field at 4.2 K. The data were all taken at zero strain after different strain cycles: measured before any strain was applied, after 1 cycle to −0.23% and after
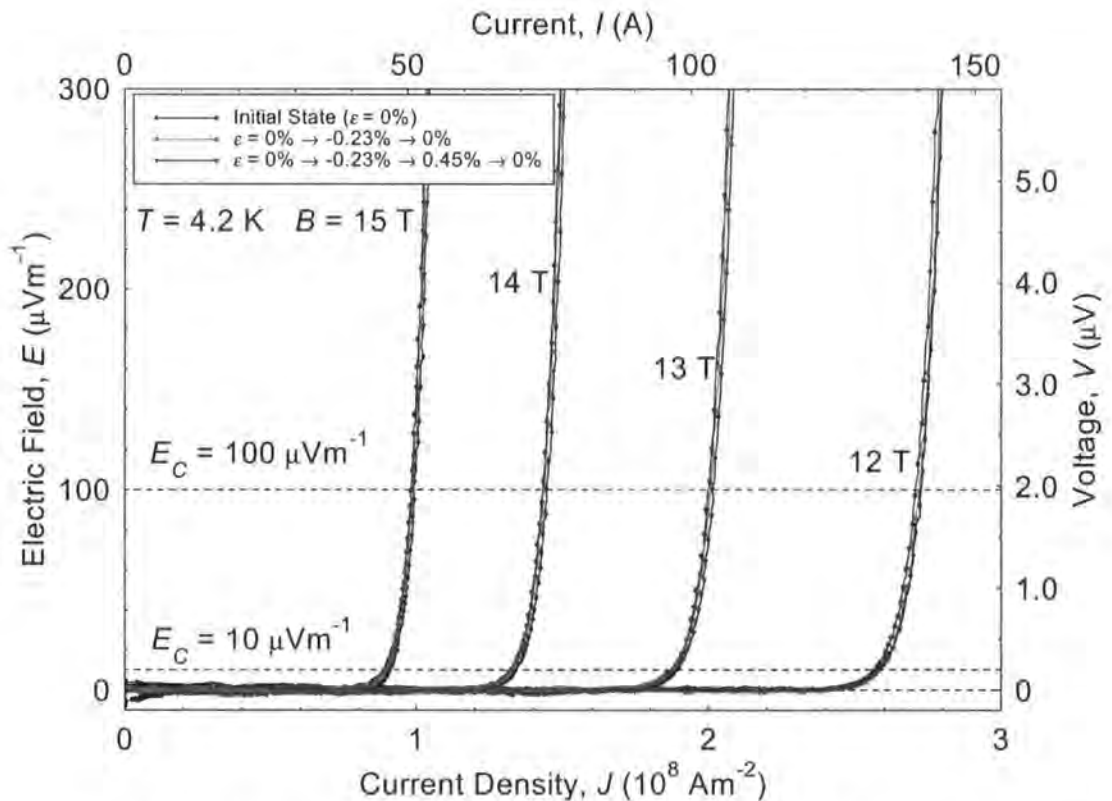


**Figure 5.5** Electric field-current density characteristics for zero strain at 4.2 K for the Nb$_3$Al strand. The data demonstrate that independent of criterion, $J_E$ is reversible. The strain was cycled as detailed in the legend.
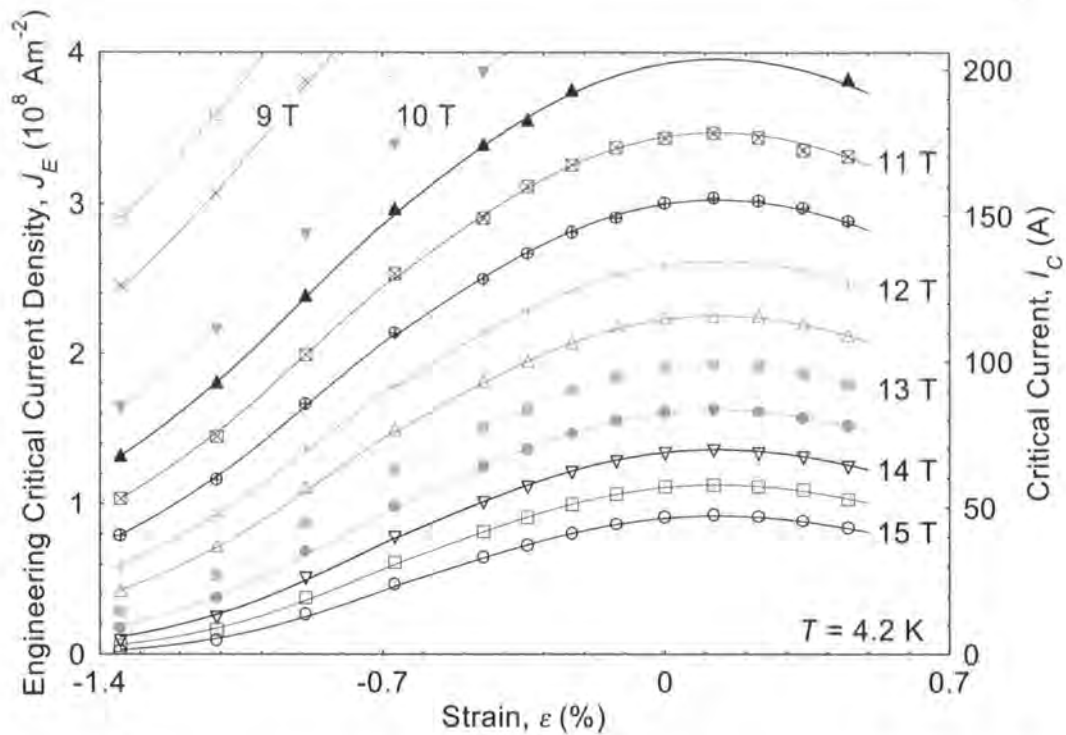
**Figure 5.6** Engineering critical current density as a function of strain and applied magnetic field at 4.2 K for the Nb$_3$Al strand. The solid lines are the technological fit to the data.
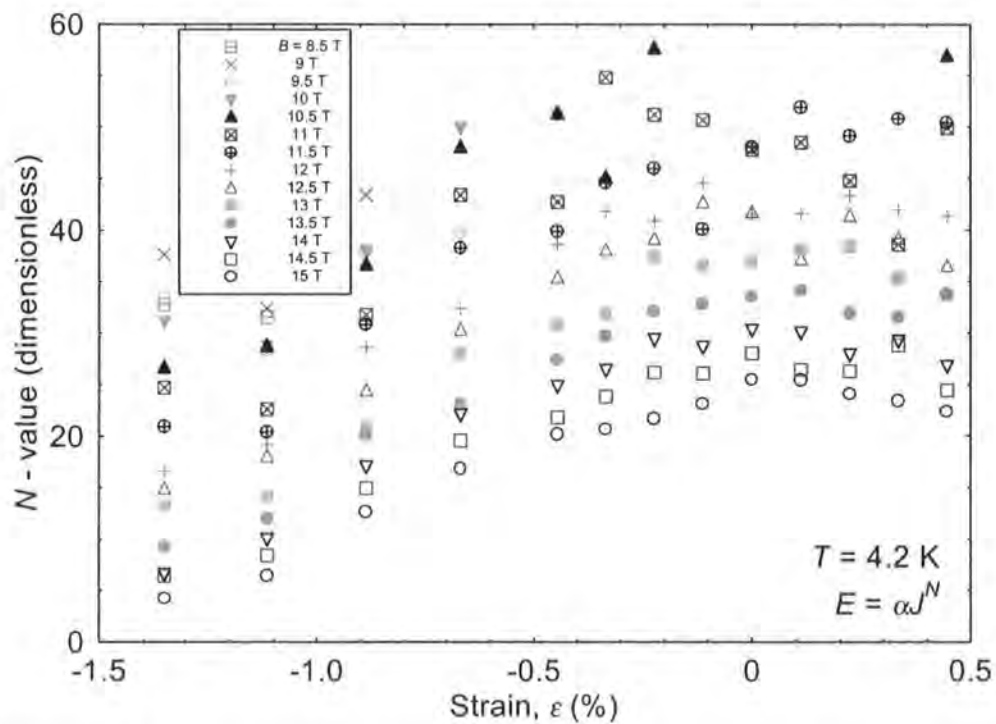


**Figure 5.7** $N$-value as a function of strain and magnetic field at 4.2 K for the Nb$_3$Al strand. The $N$-value is calculated using $E=\alpha J^N$ between 10 $\mu$Vm$^{-1}$ and 100 $\mu$Vm$^{-1}$.
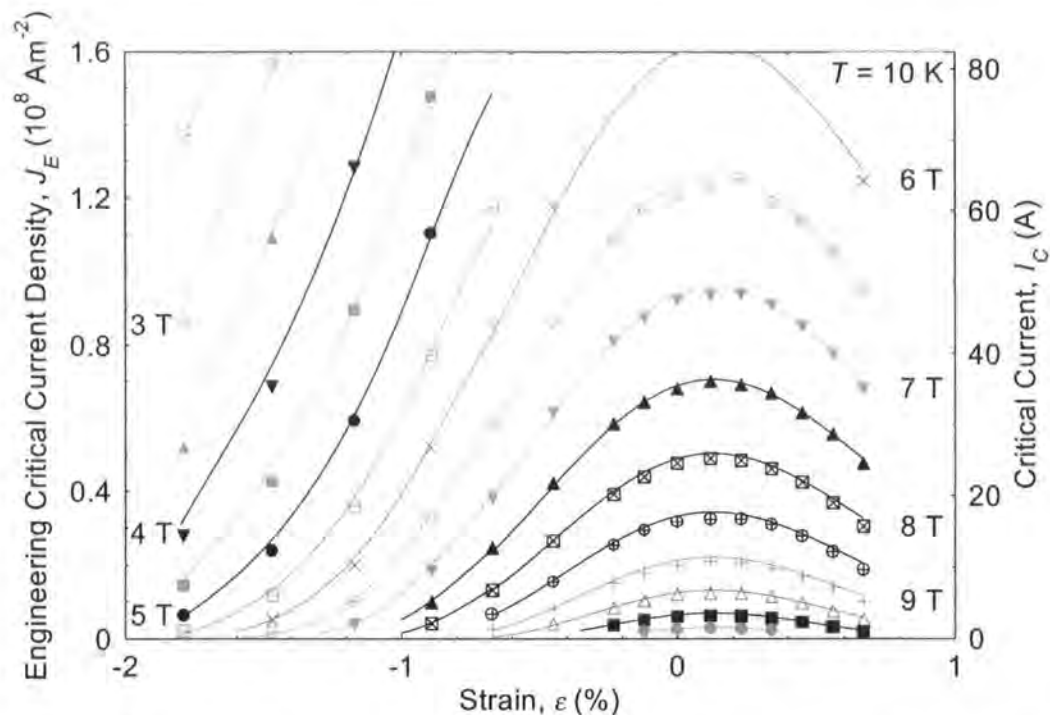
**Figure 5.8** Engineering critical current density as a function of strain and applied magnetic field at 10 K for the Nb₃Al strand. The solid lines are the technological fit to the data.
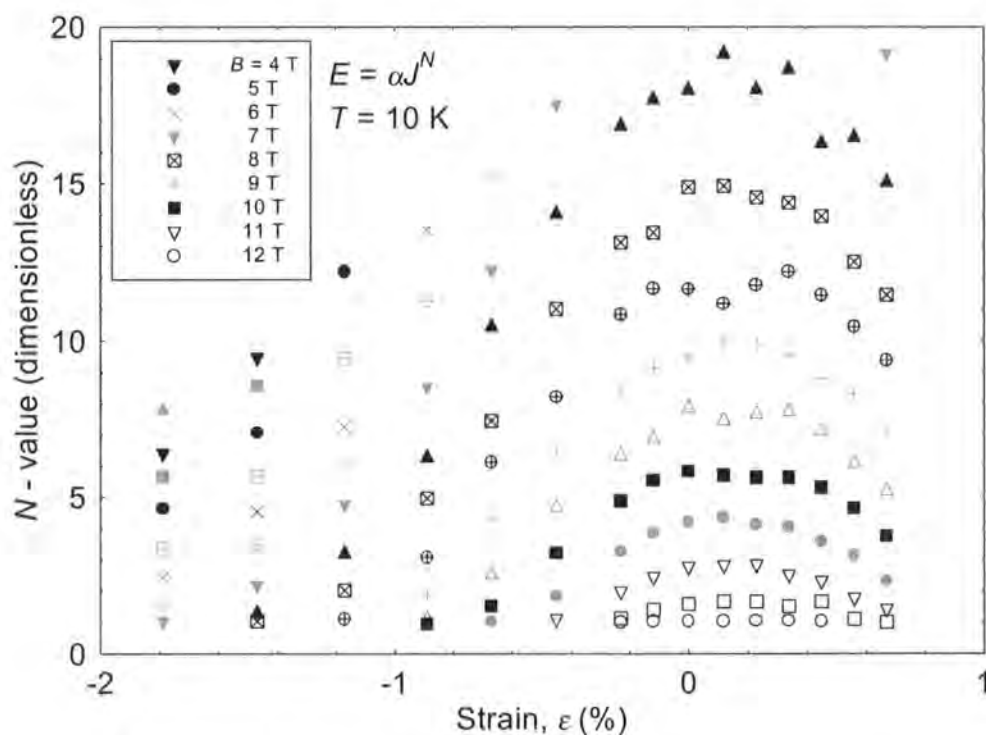


**Figure 5.9** $N$-value as a function of strain and magnetic field at 10 K for the Nb₃Al strand. The $N$-value is calculated using $E=\alpha J^N$ between 10 $\mu Vm^{-1}$ and 100 $\mu Vm^{-1}$.

a second cycle to +0.45%. The critical current density is reversible for the different strain cycles, independent of which electric field criterion is used to define it.

In preliminary experiments, different sections of all strands that were subsequently measured in detail, were first measured at zero strain and 4.2 K to test the homogeneity of the wire. The variation in $I_C$ of strand A, subsequently measured at 4.2 K alone, was 3.7%. The equivalent variation for strand B was 5%. To assess any possible damage that occurred during handling, a third strand was taken from the furnace and retained on the reaction mandrel for measurement. The strand was covered with a small amount of vacuum grease (which solidifies at 4.2 K). Measurements were made as a function of magnetic field at 4.2 K over several different sections of the wire. The variation in $I_C$ in this case was 4.3%, and the magnitude of $I_C$ was almost identical to that measured on the CuBe spring. We have concluded that to within the accuracy of our measurements, there is no evidence for damage to the sample during handling.

In Fig. 5.6, the engineering critical current density ($J_E$: the critical current divided by the entire cross sectional area of the wire of diameter 0.81 mm) measured as a function of field and strain at 4.2 K are shown. The E-field criterion used to define $I_C$ and $J_E$ over the entire data range was 10 $\mu$Vm$^{-1}$. The solid lines are from the technological fit to the data that is described in section 5.4. We report that a current transfer voltage was observed at high compressive strains which only occurred when $\varepsilon < -1\%$, and was more pronounced when $B_{C2}$ dropped below about 2 Tesla. This ohmic region in the E-J characteristic was below 5 $\mu$Vm$^{-1}$ at $I_C$. It has negligible effect on the critical current results presented in this chapter, defined at 10 $\mu$Vm$^{-1}$.

Using the standard equation, $E = \alpha J^N$, the index $N$ has been calculated in the range from 10 $\mu$Vm$^{-1}$ to 100 $\mu$Vm$^{-1}$ is shown in Fig. 5.7 as a function of strain at different fields at 4.2 K. The behaviour of $J_E$ and $N$ with strain at different magnetic fields is also shown at 10 K in Figs. 5.8 and 5.9 for comparison with the data obtained at 4.2 K. The strain at which $J_E$ is largest, $\varepsilon_M$, (originating from the precompression exerted on the Nb$_3$Al filaments from copper matrix during cooling of the sample from reaction to measurement temperature [90]) is the same for both temperatures. For these Nb$_3$Al
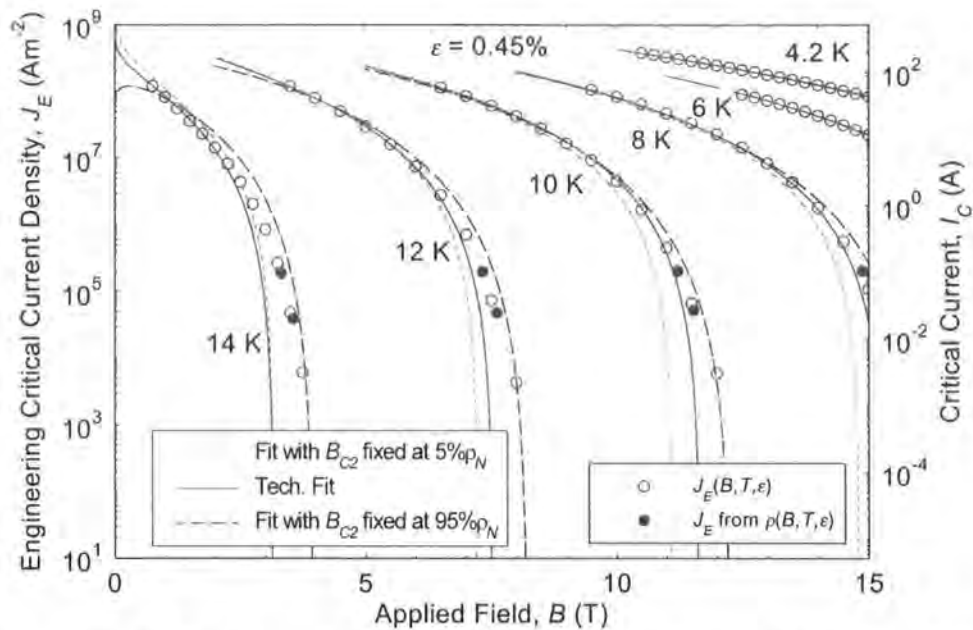
**Figure 5.10** A log-linear plot of engineering critical current density and $J_E$ derived from the resistivity measurement as a function of applied magnetic field and temperature at $\varepsilon = 0.45\%$ for the $Nb_3Al$ strand. The thick solid line shows the technological fit to the data. The thin dashed lines show technological fits to the data constraining $B_{C2}$ at $5\%\rho_N$ and $95\%\rho_N$.
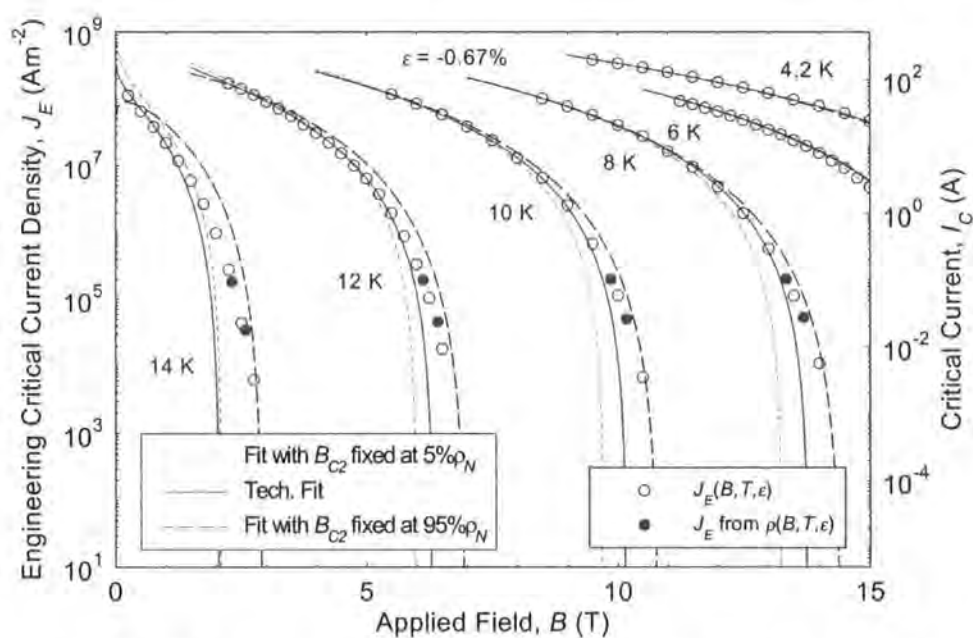


**Figure 5.11** A log-linear plot of engineering critical current density and $J_E$ derived from the resistivity measurement as a function of applied magnetic field and temperature at $\varepsilon = -0.67\%$ for the $Nb_3Al$ strand. The thick solid line shows the technological fit to the data. The thin dashed lines show technological fits to the data constraining $B_{C2}$ at $5\%\rho_N$ and $95\%\rho_N$.

strands, $\varepsilon_M = 0.15 \pm 0.03\%$.  A similar systematic dependence is noted at both temperatures for $J_E$ and $N$, which is consistent with excellent temperature stability at 10 K of better than 5 mK.  Log-linear plots of engineering critical current density as a function of magnetic field throughout the entire temperature range at $\varepsilon = 0.45\%$ and $\varepsilon = -0.67\%$ are shown in Figs. 5.10 and 5.11 respectively.

## 5.3.2 Resistivity Measurements

Typical resistivity data taken as a function of field at different temperatures and $\varepsilon = 0.45\%$ are shown in Fig. 5.12.  The noise level on the measured voltage was 0.22 $\mu$Vm$^{-1}$ which is equivalent to a resistivity noise of 1.4 p$\Omega$m, 4.0 p$\Omega$m and 17 p$\Omega$m for the 82 mA, 28 mA and 6.5 mA excitations respectively.  The resistivity data have been used to calculate $I_C$ values close to $B_{C2}$.  When the peak ac voltage (i.e. $\sqrt{2}V_{RMS}$)
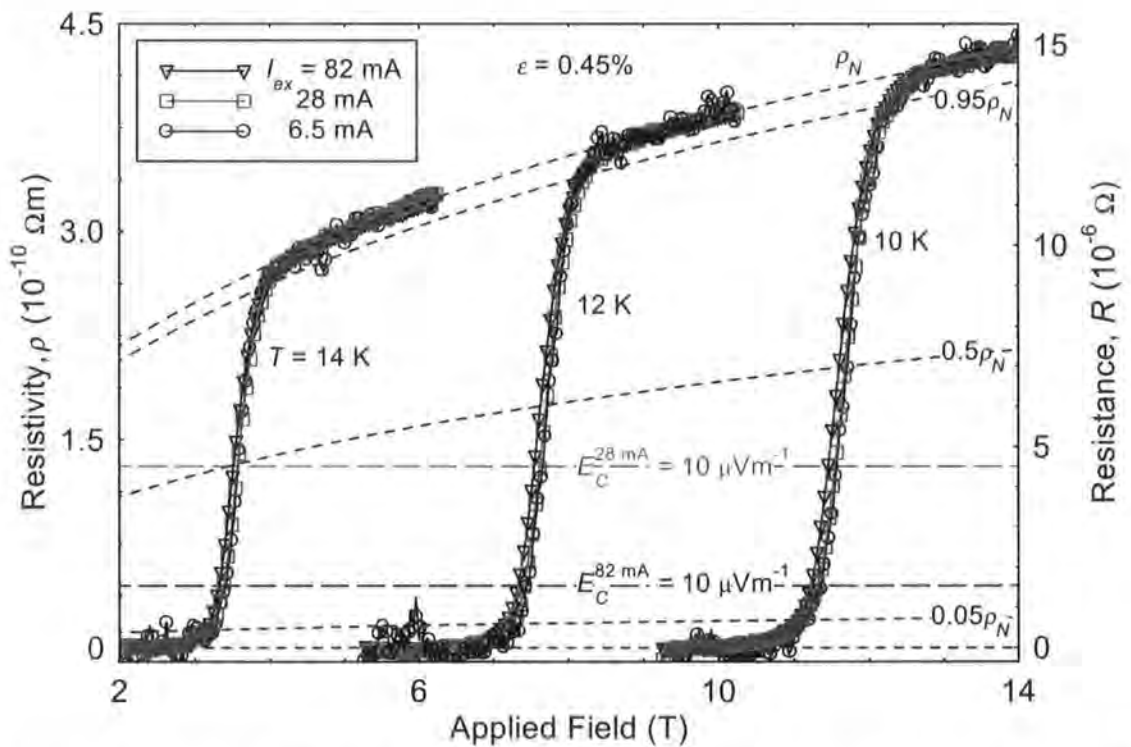


**Figure 5.12** Resistivity as a function of magnetic field at different temperatures at $\varepsilon = 0.45\%$ for the Nb$_3$Al strand.  The lines show the different criteria used to determine upper critical field and derive a critical current density.

generated across the sample reaches $10 \, \mu Vm^{-1}$, it is assumed that the peak ac current (minus the shunt current) provides the value of $I_C$ at the applied field. It was not possible to generate $I_C$ data for the 6.5 mA excitation because even in the normal state, the $E$-field generated was not sufficiently high. The construction lines to determine both $B_{C2}$ and $I_C$ are shown on Fig. 5.12. It should be noted that the shape of the resistivity transition at 28 mA and 6.5 mA excitation current are very similar. In Figs. 5.10 and 5.11, the inclusion of $J_E$ obtained through the $V$-$I$ and resistivity measurements demonstrates good agreement between the two types of measurement. Figure 5.13 shows the upper critical field determined at 50% of the normal state resistivity as a function of temperature and strain from the data obtained using 28 mA excitation current.
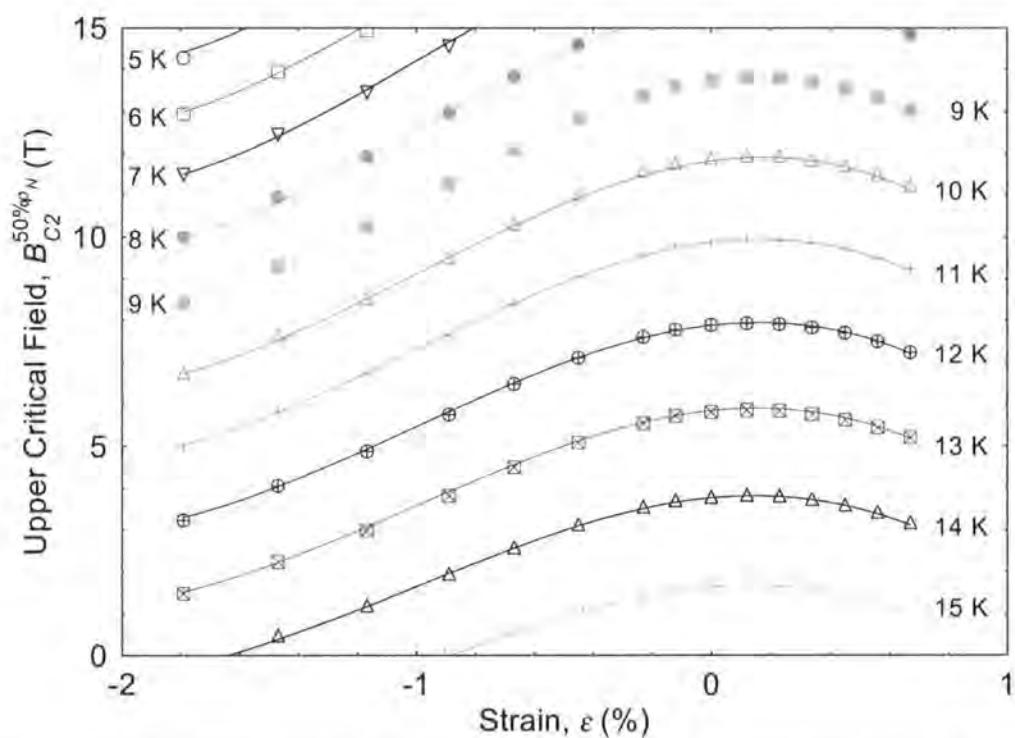


**Figure 5.13** Upper critical field as a function temperature and strain for the $Nb_3Al$ strand. Upper critical field is determined at 50% of the normal state resistivity.

### 5.3.3 Comparison with other data in the literature
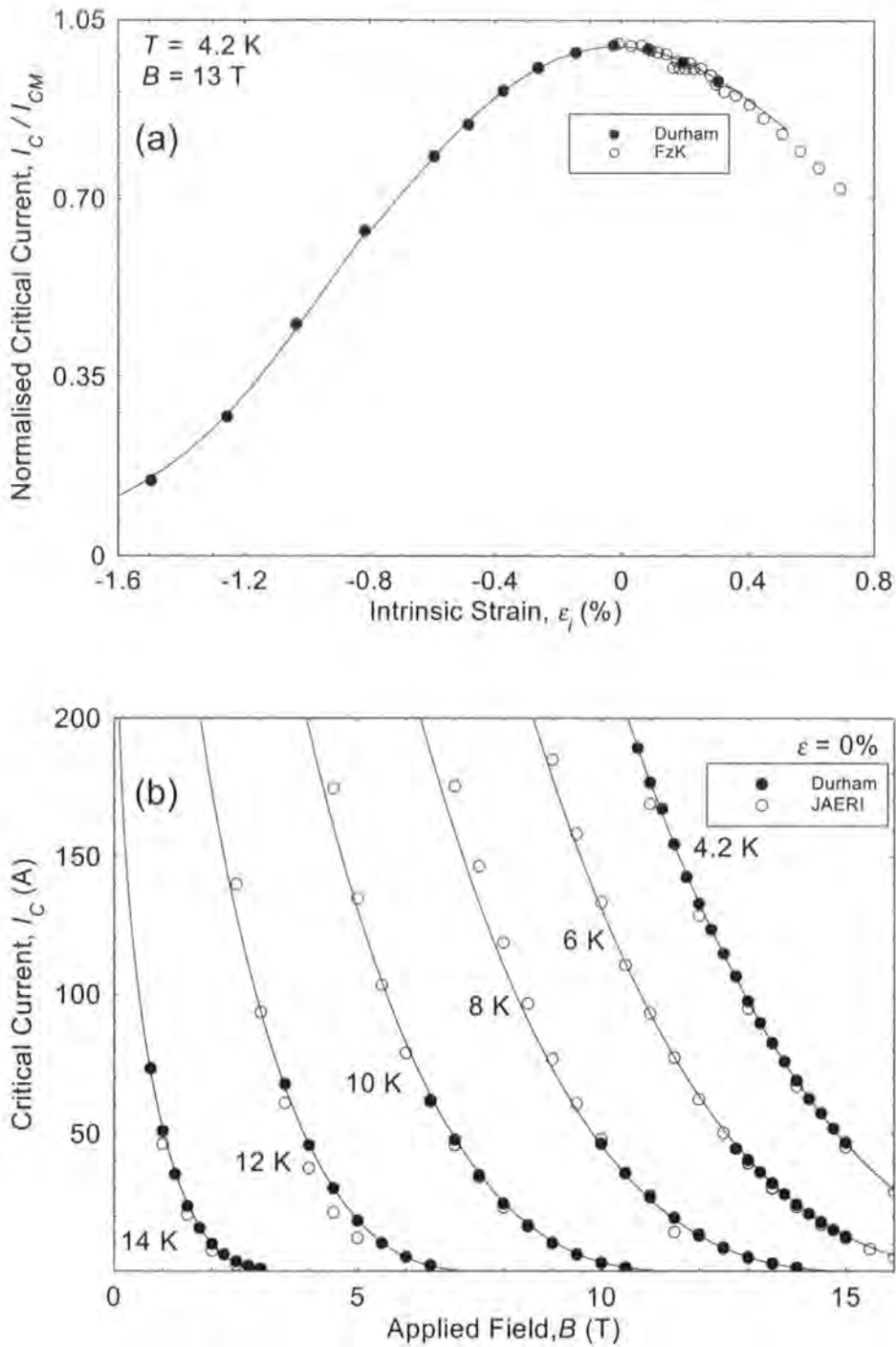


**Figure 5.14** Comparison of critical current measurements between similar Nb3Al strands in the literature. (a) Normalised critical current as a function of intrinsic strain at 13 T and 4.2 K for measurements performed in Durham and FzK [110], (b) Critical current as a function of field at various temperatures and zero strain between Durham and JAERI [140]. The solid lines shown are the technological fit to the data.

A comparison between data generated in Durham and that from FzK (Forschungszentrum Karlsruhe) and JAERI (Japanese Atomic Energy Research Institute) is shown in Fig. 5.14. Figure 5.14(a) shows the normalised critical current as a function of strain at 4.2 K and 13 T from Durham and FzK [110]. At FzK, an axial pull rig is used to apply strain [132]. Although the strand investigated by FzK is not identical to the one studied in this chapter, it is similar so the good agreement found is expected. A similar comparison has been made between data from Durham and FzK on $Nb_3Sn$ wires and again good agreement was obtained between both methods [141, 142]. In Fig. 5.14(b), comparison is made between the variable temperature data of JAERI [140] and Durham at zero strain. We conclude that there is very good agreement between the three laboratories for $I_C$ measured in overlapping field-temperature-strain conditions using different measurement techniques.

## 5.4    Empirical parameterisation of the data

The bulk pinning force density, $F_P = J_E B$, for many low-temperature type-II superconductors varies with field, temperature and strain according the semi-empirical Fietz-Webb scaling law of the form [95, 96, 143, 144]:

$$F_P = J_E B = C(T, \varepsilon) b^p (1 - b)^q \tag{5.1}$$

where $b$ is the reduced field ($B/B_{C2}$) and $p$ and $q$ are constants. For low temperature A15 conductors, the upper critical field data can be parameterised using the empirical equation [108, 127, 145]:

$$B_{C2}(T, \varepsilon) = B_{C2}(0, \varepsilon) \left[ 1 - \left( \frac{T}{T_C(\varepsilon)} \right)^\nu \right] \tag{5.2}$$

where $B_{C2}(0, \varepsilon)$ and $T_C(\varepsilon)$ are the strain dependant upper critical field at 0 K and the critical temperature respectively and $\nu$ is a constant. Two alternative empirical forms for the prefactor, $C(T, \varepsilon)$, have been considered [99, 124, 125]:

$$C(T, \varepsilon) = A(T)\big[B_{C2}(\varepsilon)\big]^m \qquad (5.3)$$

$$C(T, \varepsilon) = A(\varepsilon)\big[B_{C2}(T)\big]^n \qquad (5.4)$$

where $A(\varepsilon$ or $T)$ is a function of strain or temperature only. The parameter $m$ is the strain index, and $n$ is the temperature index. These exponents have been named in this way because historically $m$ was determined from variable-strain measurements of $J_E$ at constant temperature and $n$ from variable temperature measurements of $J_E$ at constant strain.

Figure 5.15 shows the critical current of the Nb$_3$Al strand as a function of field at 4.2 K and $\varepsilon = 0.45\%$ and scaling law fits to the data with different values of C, $B_{C2}$, $p$ and $q$.
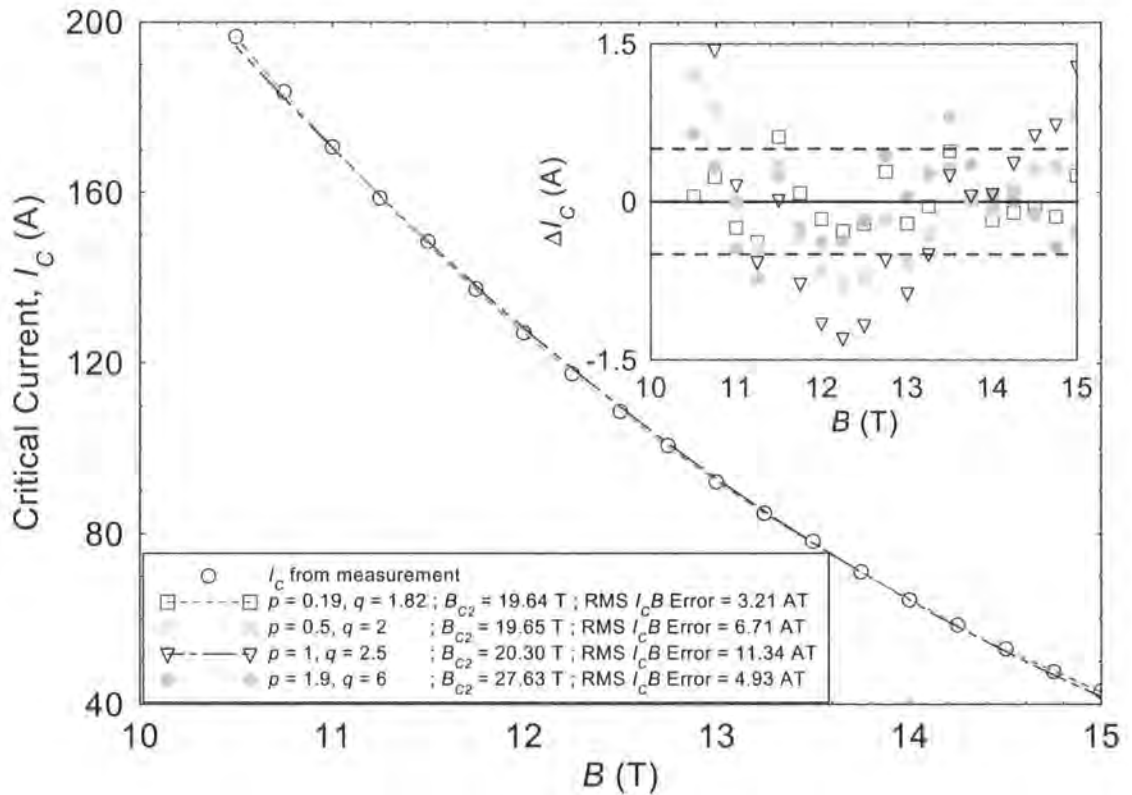


**Figure 5.15** Critical current as a function of applied field at 4.2 K and $\varepsilon = 0.45\%$ for the Nb$_3$Al strand. The lines indicate four acceptable fits to the data using widely varying $p$ and $q$. The equivalent RMS $I_C$ errors are approximately an order of magnitude smaller than the RMS $I_CB$ errors (i.e. ~0.4 A and ~1 A). The inset graph shows the difference in $I_C$ between the data and the fits.

The difference in $I_C$ between the data and the fits is about 0.5 Amp (shown inset) which is within experimental error. The constants $p$, $q$ and $B_{C2}$ are strongly positively correlated. In the context of trying to distinguish which mechanism determines $J_E$, where changes of ½ in either $p$ or $q$ implies a change of mechanism (for example, surface pinning by normal precipitates leads to $p = 0.5$ and $q = 2$ whereas point pinning gives $p = 1$ and $q = 2$ [144]), the range of $p$ and $q$ values that are consistent with the data is enormous. Although extremely good fits can be found to parameterise the data, Fig. 5.15 demonstrates that if $B_{C2}$ is left as a free-parameter, any interpretation of a single pair of these correlated $p$ and $q$ values is completely unreliable.

Nevertheless from a magnet engineering/technological perspective, the primary function of the unified scaling law is to provide an accurate mathematical description of the $J_E(B,T,\varepsilon)$ data that can be used to optimise design parameters. Whether another equivalent functional form exists is very much of secondary interest. It is demonstrated in section 5.5 that a greater range of data can be more accurately parameterised using Eqn. (5.4) rather than Eqn. (5.3). More specifically the errors on the temperature index, $n$, are lower than those for the strain index $m$. Combining Eqns. (5.1), (5.2) and (5.4), a unified empirical relation for $F_P$ is [108, 124]:

$$F_P = J_E B = A^*(\varepsilon) \left\{ B_{C2}^*(0,\varepsilon) \left[ 1 - \left( \frac{T}{T_C^*} \right)^\nu \right] \right\}^n b^p (1-b)^q \qquad (5.5)$$

For simplicity, it has been assumed that the maximum in $B_{C2}^*$, $T_C^*$, $J_E$ and the minimum in $A^*(\varepsilon)$ occur at the same strain, $\varepsilon_M$. The utility and accuracy of the parameterisation was further improved by only considering $I_C$ data of technological importance, namely above 1 Amp and by leaving $B_{C2}^*$ as a free parameter. This latter condition improves the accuracy of the parameterisation at the expense of no longer identifying $B_{C2}^*$ with any features of the resistive transitions, or with a characteristic field of any physical significance.

| Data Range | $p$ | $q$ | $n$ | $v$ |
|---|---|---|---|---|
| 4.2 K $\leq T \leq$ 10 K<br>-0.67% $\leq \varepsilon \leq$ 0.67% | 0.845 | 2.740 | 2.301 | 1.323 |
| 4.2 K $\leq T \leq$ 10 K<br>-1.79% $\leq \varepsilon <$ -0.67% | 1.125 | 2.893 | 2.392 | 1.250 |
| 10 K $< T \leq$ 14 K<br>-1.79% $\leq \varepsilon \leq$ 0.67% | 0.787 | 2.756 | 2.249 | 1.403 |

**Table 5.1** Constants derived from the technological fit to the critical current data for the Nb$_3$Al strand.

| –0.67% $\leq \varepsilon \leq$ +0.67%<br>4.2 K $\leq T \leq$ 10 K | $A^*(\varepsilon)$ (Am$^{-2}$T$^{-2.301}$) | $B_{C2}^*(0,\varepsilon)$ (T) | $T_C^*(\varepsilon)$ (K) |
|---|---|---|---|
| $c_0$ | $3.942 \times 10^7$ | 26.26 | 15.81 |
| $c_1$ | 0 | 0 | 0 |
| $c_2$ | $5.424 \times 10^{10}$ | $-3.264 \times 10^4$ | $-1.255 \times 10^4$ |
| $c_3$ | $-3.096 \times 10^{12}$ | $6.521 \times 10^5$ | $2.202 \times 10^6$ |
| $c_4$ | $-3.608 \times 10^{14}$ | $1.156 \times 10^8$ | $4.190 \times 10^7$ |

**Table 5.2** Free parameters for the technical parameterisation in the range –0.67% $\leq \varepsilon \leq$ +0.67%, 4.2 K $\leq T \leq$ 10 K for the Nb$_3$Al strand.

| –1.79% $\leq \varepsilon <$ –0.67%<br>4.2 K $\leq T \leq$ 10 K | $A^*(\varepsilon)$ (Am$^{-2}$T$^{-2.392}$) | $B_{C2}^*(0,\varepsilon)$ (T) | $T_C^*(\varepsilon)$ (K) |
|---|---|---|---|
| $c_0$ | $2.552 \times 10^7$ | 23.18 | 12.52 |
| $c_1$ | $-3.567 \times 10^9$ | $-1.535 \times 10^3$ | $-1.126 \times 10^3$ |
| $c_2$ | $-2.028 \times 10^{11}$ | $-2.617 \times 10^5$ | $-1.459 \times 10^5$ |
| $c_3$ | $-6.839 \times 10^{12}$ | $-1.382 \times 10^7$ | $-7.206 \times 10^5$ |
| $c_4$ | $-1.250 \times 10^{14}$ | $-2.524 \times 10^8$ | $-1.307 \times 10^8$ |

**Table 5.3** Free parameters for the technical parameterisation in the range –1.79% $\leq \varepsilon <$ -0.67%, 4.2 K $\leq T \leq$ 10 K for the Nb$_3$Al strand.

| –1.79% $\leq \varepsilon \leq$ +0.67%,<br>10 K $< T \leq$ 14 K | $A^*(\varepsilon)$ (Am$^{-2}$T$^{-2.249}$) | $B_{C2}^*(0,\varepsilon)$ (T) | $T_C^*(\varepsilon)$ (K) |
|---|---|---|---|
| $c_0$ | $4.455 \times 10^7$ | 25.88 | 15.49 |
| $c_1$ | 0 | 0 | 0 |
| $c_2$ | $4.416 \times 10^{10}$ | $-3.024 \times 10^4$ | $-1.017 \times 10^4$ |
| $c_3$ | $3.244 \times 10^{12}$ | $5.446 \times 10^5$ | $-1.737 \times 10^5$ |
| $c_4$ | $7.452 \times 10^{13}$ | $6.801 \times 10^7$ | $5.646 \times 10^5$ |

**Table 5.4** Free parameters for the technical parameterisation in the range –1.79% $\leq \varepsilon \leq$ +0.67%, 10 K $< T \leq$ 14 K for the Nb$_3$Al strand.

In order to obtain the fitting parameters in Eqn. (5.5), a preliminary global fit of all the data was made. The values of $A^*(\varepsilon)$, $T_C^*(\varepsilon)$ and $B_{C2}^*(0,\varepsilon)$ obtained in this way were then fitted to fourth-order polynomial functions where:

$$\left.\begin{array}{c} A^*(\varepsilon_I) \\ B_{C2}^*(0,\varepsilon_I) \\ T_C^*(\varepsilon_I) \end{array}\right\} = c_0 + c_1\varepsilon_I + c_2\varepsilon_I^2 + c_3\varepsilon_I^3 + c_4\varepsilon_I^4 \qquad (5.6)$$

and $c_n$ are constants. To improve further the accuracy of the parameterisation, three different ranges of temperature-strain phase space were identified and fits to Eqns. (5.5) and (5.6) were made in each of those ranges alone. A fit of each data set in each range was then completed with the constants in the polynomial fits and $n$, $\nu$, $\varepsilon_M$, $p$ and $q$ as free parameters. The value of $\varepsilon_M$ was found to be 0.131%. The parameterisations are described in terms of intrinsic strain $\varepsilon_I$, and the applied strain $\varepsilon$, where $\varepsilon_I = \varepsilon - \varepsilon_M$. The values found for $n$, $p$, $q$ and $\nu$ are shown in Table 5.1. It is understood that one can parameterise these data using a more physical form for the constants [99, 146], however for this technological fit we have used polynomials because they provide the most accurate mathematical description of the data. The constants in the polynomial fits are shown in Tables 5.2 – 5.4. Most of the data is parameterised to within ± 1 A of the measured values. To achieve this accuracy, it is clear that single pair of $p$ and $q$ values cannot be used to parameterise the entire set of data. A comparison between measured $J_E$ data and the technological fit is shown as a function of temperature at $\varepsilon = 0.45\%$ and $\varepsilon = -0.67\%$ in Figs. 5.10 and 5.11 respectively. The fit only starts to break down at very high temperatures and high compressive strains where $B_{C2}^*$ is of the order of 2 T. Also shown in Figs. 5.10 and 5.11 are fits to the data where $B_{C2}$ has been constrained at $5\%\rho_N$ and $95\%\rho_N$, and $p$, $q$, $n$, and $\nu$ are assumed single valued throughout the entire range of data. It can be seen that the fits constrained at $95\%\rho_N$ fit the high field, low $J_E$ tail well, but does not provide a good overall fit. On the other hand, defining $B_{C2}$ at $5\%\rho_N$ provides a better overall fit to the data at the expense of not fitting the low $J_E$ data.

| Upper critical field defined at: | $\nu$ (dimensionless) | Standard Deviation (mT) |
|---|---|---|
| $5\%\rho_N$ | 1.25 | 38.9 |
| $50\%\rho_N$ | 1.27 | 33.5 |
| $95\%\rho_N$ | 1.31 | 30.2 |

**Table 5.5** Upper critical field scaling law parameter ($\nu$) derived from the resisitivity data and the standard deviation on the fit to the data for the Nb$_3$Al strand.

| $T_C^\rho(\varepsilon)$ (K) defined at: | $5\%\rho_N$ | $50\%\rho_N$ | $95\%\rho_N$ |
|---|---|---|---|
| $c_0$ | 15.63 | 15.78 | 15.91 |
| $c_1$ | 0 | 0 | 0 |
| $c_2$ | $-1.040\times10^4$ | $-9.736\times10^3$ | $-9.853\times10^3$ |
| $c_3$ | $-9.337\times10^4$ | $-1.832\times10^5$ | $-1.769\times10^5$ |
| $c_4$ | $7.034\times10^6$ | $2.622\times10^6$ | $3.564\times10^6$ |
| $B_{C2}^\rho(0,\varepsilon)$ (T) defined at: | $5\%\rho_N$ | $50\%\rho_N$ | $95\%\rho_N$ |
| $c_0$ | 26.53 | 27.08 | 27.48 |
| $c_1$ | 0 | 0 | 0 |
| $c_2$ | $-3.529\times10^4$ | $-3.908\times10^4$ | $-3.755\times10^4$ |
| $c_3$ | $-4.971\times10^5$ | $-8.122\times10^5$ | $-7.018\times10^5$ |
| $c_4$ | $1.876\times10^7$ | $1.192\times10^7$ | $1.364\times10^7$ |

**Table 5.6** Free parameters for the technical parameterisation of the upper critical field data for the Nb$_3$Al strand.
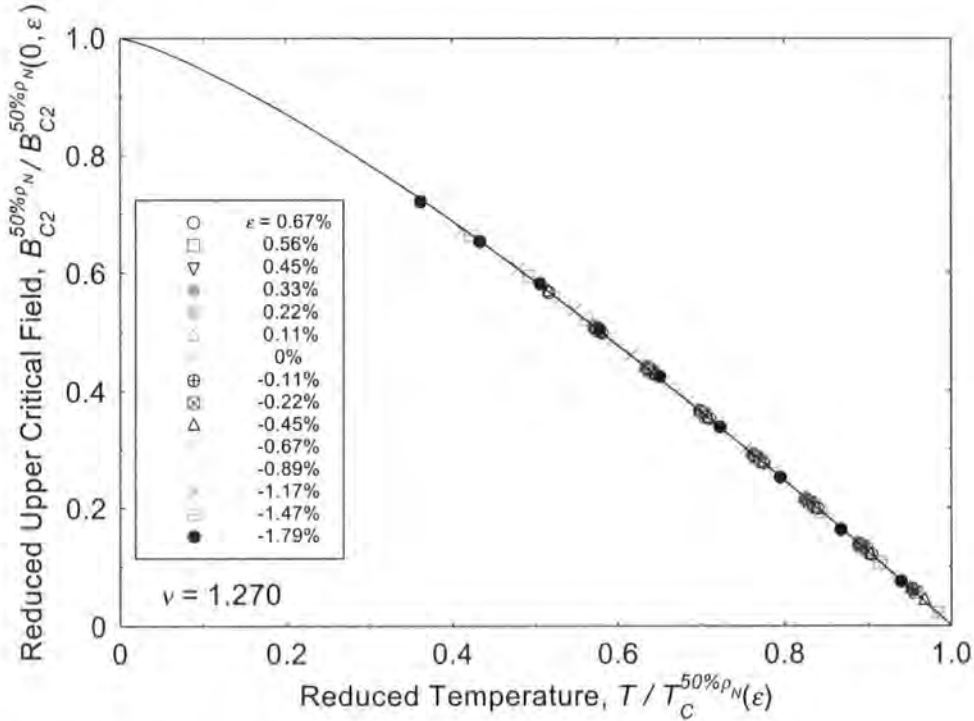


**Figure 5.16** A universal scaling law showing the reduced upper critical field as a function of reduced temperature and applied strain for the Nb$_3$Al strand.
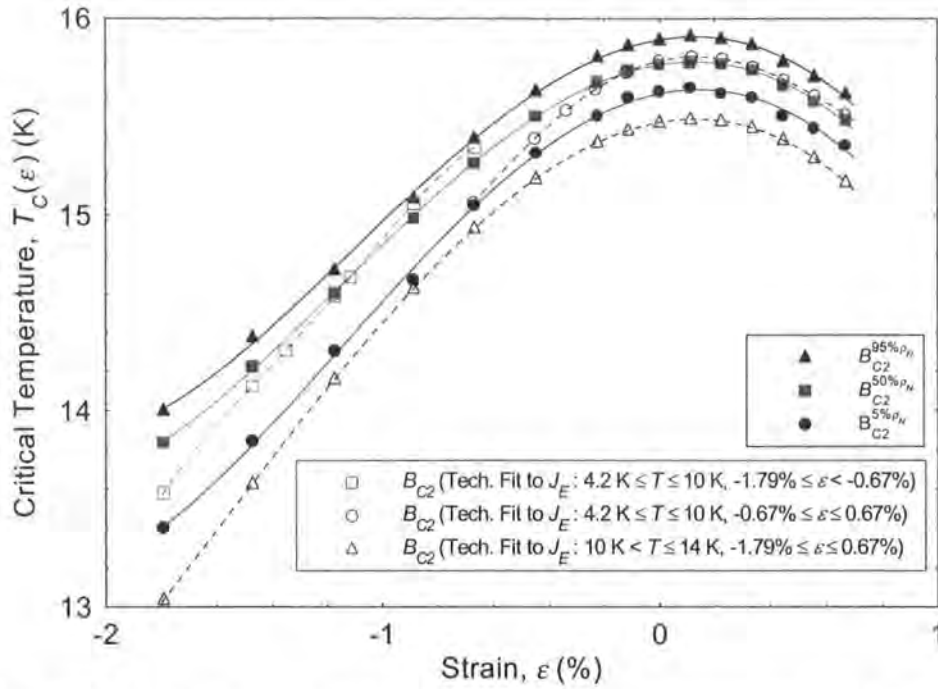
**Figure 5.17** Effective critical temperature as a function of applied strain for the Nb₃Al strand. The solid symbols represent data obtained from the ac resistivity measurement of $B_{C2}$. The open symbols are derived from the technological fit to the critical current data. The lines are 4th order polynomial fits that parameterise the data.
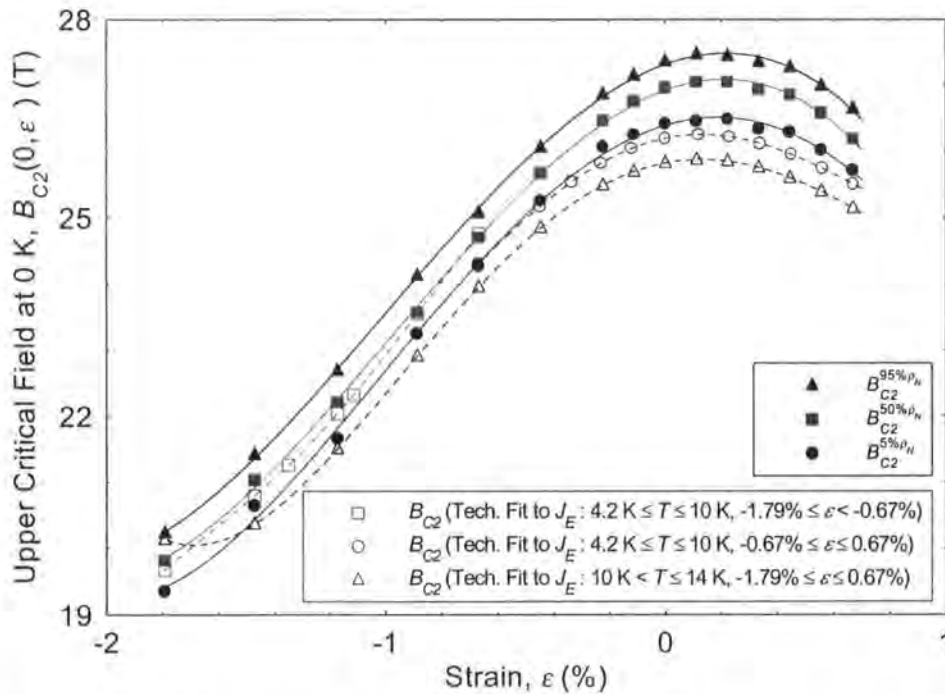


**Figure 5.18** Effective upper critical field at 0 K as a function of applied strain for the Nb₃Al strand. The solid symbols represent data obtained from the ac resistivity measurement of $B_{C2}$. The open symbols are derived from the technological fit to the critical current data. The lines are 4th order polynomial fits that parameterise the data.

The upper critical field that was determined from the resistivity data defined at 5%, 50% and 95% of the normal state resistivity has been parameterised using Eqn. (5.2). Values for $\nu$ are presented in table 5.5, along with the standard deviation of the fit to each data set. $B_{C2}^{\rho_N}(0,\varepsilon)$ and $T_C^{\rho_N}(\varepsilon)$ defined at 5%, 50% and 95% of the normal state resistivity have been also parameterised using $4^{th}$ order polynomial fits and the constants given in Table 5.6. Fig. 5.16 shows the scaling of the upper critical field defined at a criteria of $50\%\rho_N$. Good scaling of the data was also observed for $B_{C2}^{\rho_N}(T,\varepsilon)$ defined at $5\%\rho_N$ and $95\%\rho_N$. In Figs. 5.17 and 5.18, $T_C^{\rho_N}(\varepsilon)$ and $B_{C2}^{\rho_N}(0,\varepsilon)$ are plotted as a function of strain. Note that for these empirical fits to the data, the strain at which $T_C^{\rho_N}(\varepsilon)$ and $B_{C2}^{\rho_N}(0,\varepsilon)$ are maximum are found to be $\varepsilon_M = 0.13\%$ and $\varepsilon_M = 0.20\%$ respectively. Also shown are
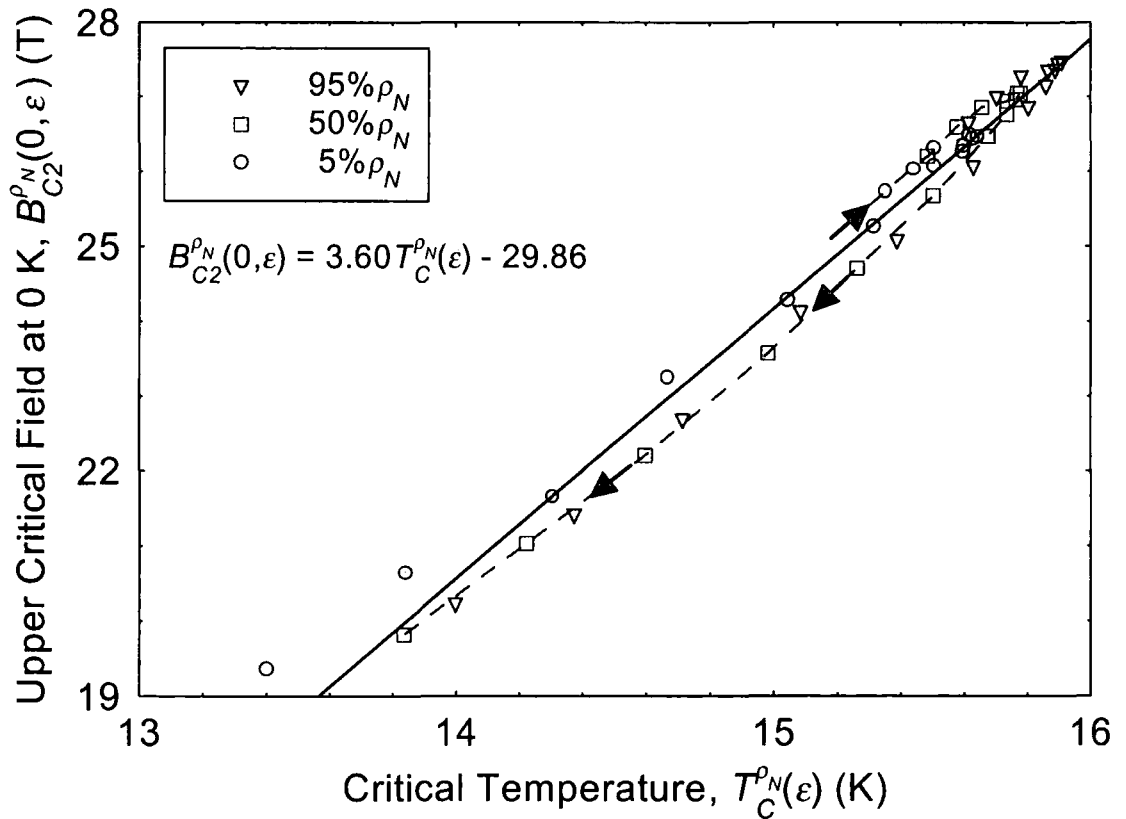


**Figure 5.19** Effective upper critical field at 0 K as a function of the effective critical temperature for the Nb₃Al strand. The internal variable is the applied strain. The dashed line indicates the double valued behaviour in the data with the arrows indicating decreasing strain.
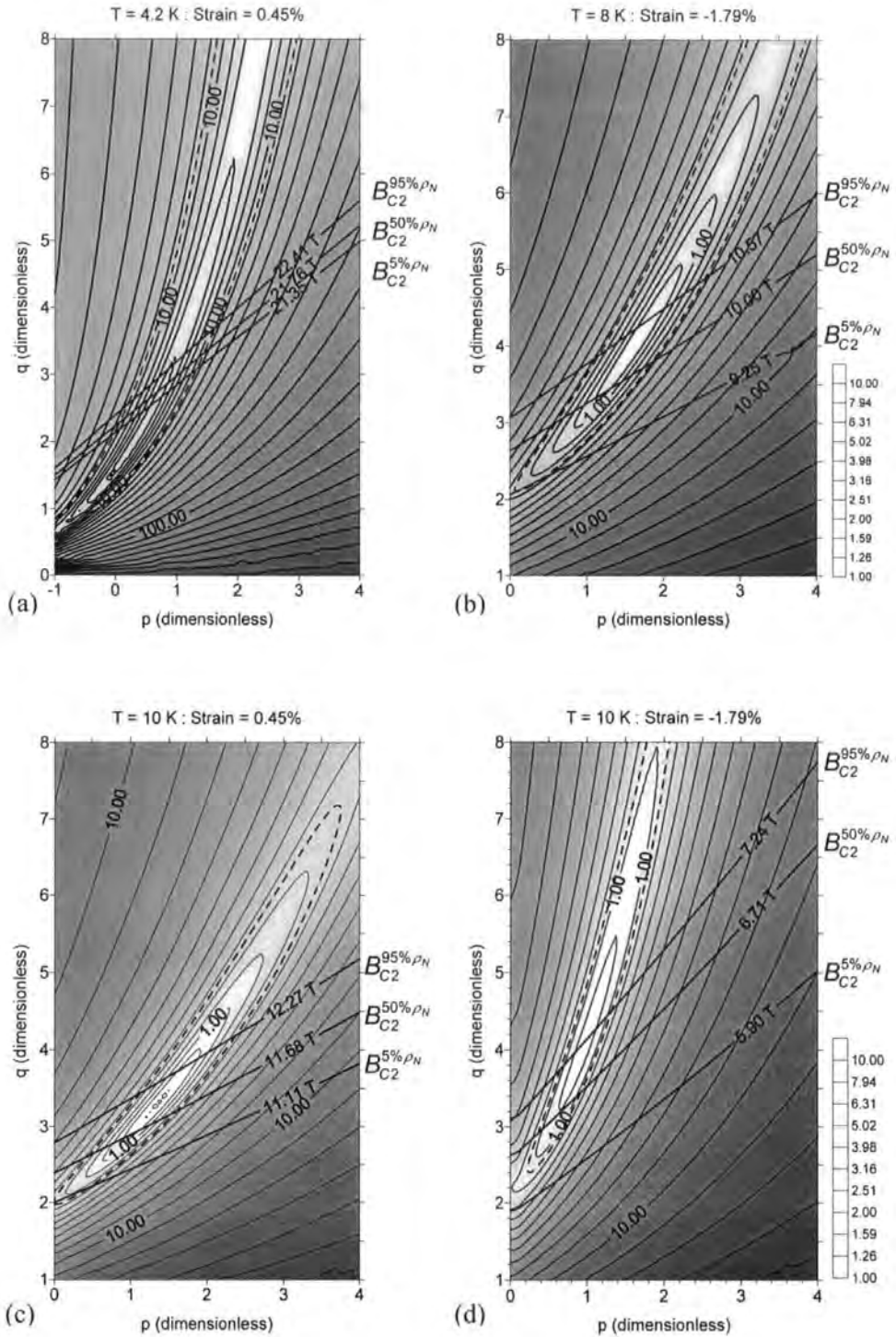
**Figure 5.20** RMS $I_CB$ error surface plots as a function of $p$ and $q$ from fitting to the data at (a) 4.2 K and $\varepsilon = 0.45\%$, (b) 8 K and $\varepsilon = -1.79\%$, (c) 10 K and $\varepsilon = 0.45\%$ and (d) 10 K and $\varepsilon = -1.79\%$ for the Nb$_3$Al strand. The dashed line indicates the maximum RMS error for an acceptable fit. The solid curves give $p$, $q$ pair-values when the upper critical field is constrained by $B_{C2}$ from the resistivity data. The contours on the error surface are logarithmically spaced per decade as indicated in the legend.

the effective $T_C^*(\varepsilon)$ and $B_{C2}^*(0,\varepsilon)$ that are derived from the technological fit. Figures 5.17 and 5.18 allow comparison between $B_{C2}^{\rho_N}(0,\varepsilon)$ and $T_C^{\rho_N}(\varepsilon)$ extracted from the parameterisation of the upper critical field data from the resistivity measurements and the technological fit to the critical current data. There is no simple relation between $B_{C2}$ derived from these different measurements.

The data from the resistivity measurements in Figs. 5.17 and 5.18 have been replotted in Fig. 5.19. The linearity and double-valued behaviour has also been observed in $Nb_3Sn$ (derived from extrapolating $J_E$ values to zero) [108]. In both cases a positive gradient and negative intercept was observed.

## 5.5    Physics and scaling laws

To proceed beyond the empirical scaling laws, we need to break the strong correlation between $p$, $q$ and $B_{C2}$. This can be done, in principle, by measuring $B_{C2}$ directly. However, technological conductors are not homogeneous. Inevitably the field at which the critical current density drops to zero represents the upper critical field for the percolative path through the material with the highest $B_{C2}$. This high $B_{C2}$ value is not representative of the material. Physical interpretation of the data is required to eliminate non-physical solutions, identify an characteristic value of $B_{C2}$ (where the critical current is not zero) and hence identify a scaling law that can be used to address the science that underlies the mechanism that determines the critical current density.

In Fig. 5.20, RMS $I_CB$ error surfaces are shown for $p$ and $q$ derived from the variable magnetic field data at 4.2 K for (a) $\varepsilon = 0.45\%$, at 8 K for (b) $\varepsilon = -1.79\%$ and at 10 K for (c) $\varepsilon = 0.45\%$ and (d) $\varepsilon = -1.79\%$. The range of fields over which these data were taken were a) 10.5 to 15 T, b) 8.5 to 15 T, c) 6 to 11.5 T, d) 2.5 to 7 T respectively. The solid contours are logarithmically separated for each decade as indicated in the legend and the dashed contour shows the approximate maximum RMS $I_CB$ error that still provides an acceptable fit that is within the errors of the data. From the fit to the data, $B_{C2}$ and $C$ values are also generated. The figure shows solid curves giving $p$-$q$ pair-values when $B_{C2}$ takes the value determined from the resistivity measurements at $5\%\rho_N$, $50\%\rho_N$ and
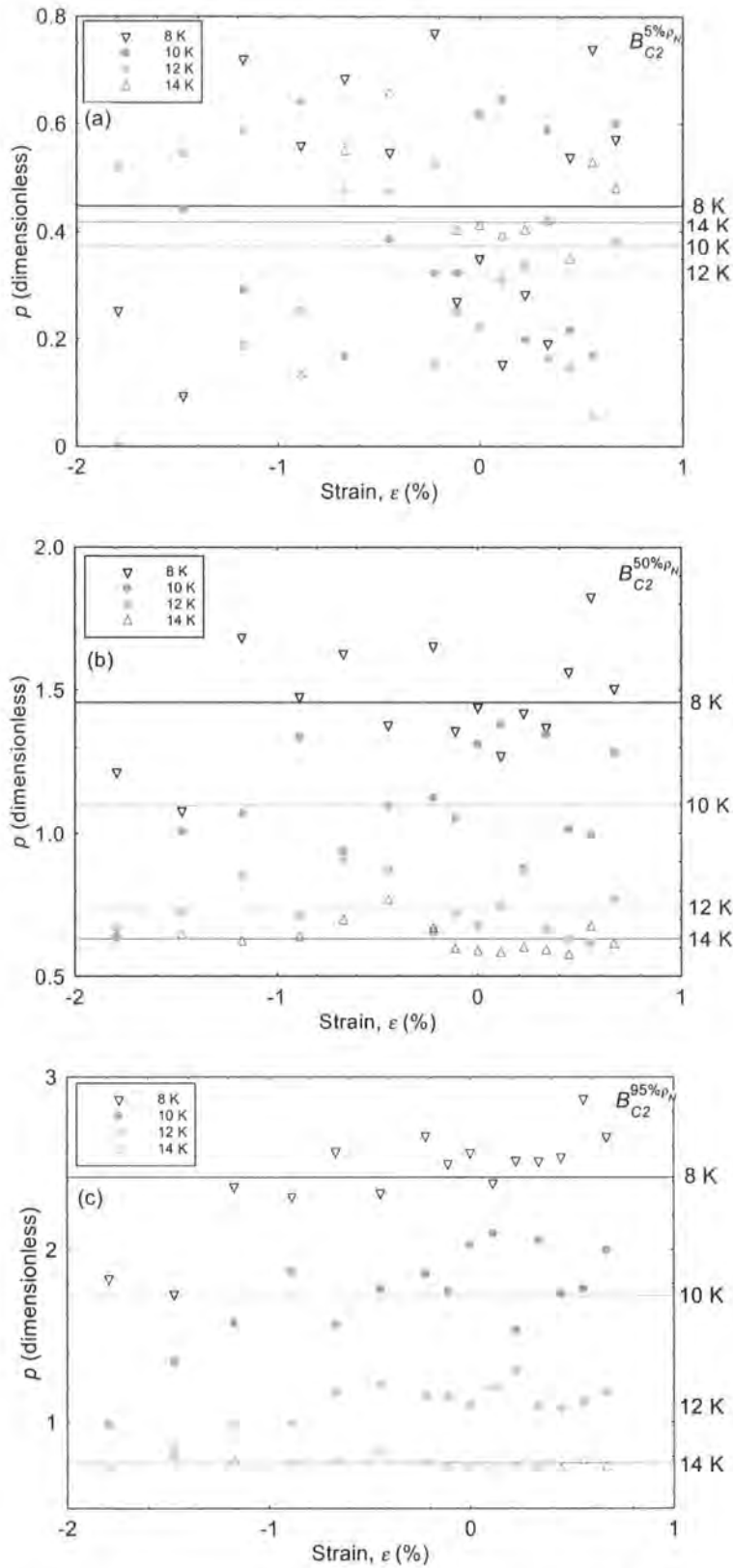
**Figure 5.21** Scaling law exponent, $p$, as a function of strain for the Nb$_3$Al strand. The data were obtained from a fit constraining $B_{C2}$ at a) 5%$\rho_N$, b) 50%$\rho_N$ and c) 95%$\rho_N$. The solid lines show fits to the data in the strain range $-1.8\% \le \varepsilon \le 0.7\%$.
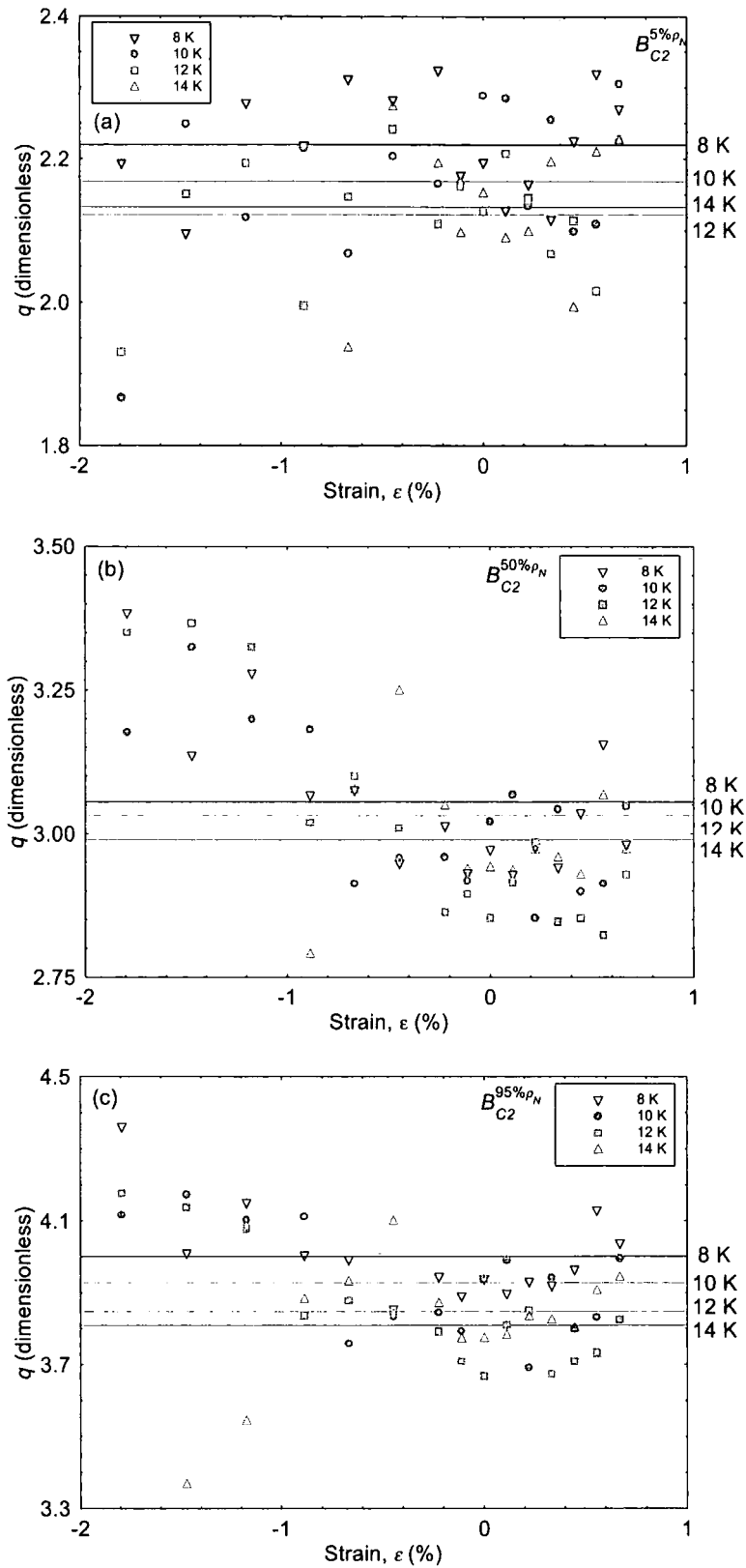
**Figure 5.22** Scaling law exponent, $q$, as a function of strain for the Nb$_3$Al strand. The data were obtained from a fit constraining $B_{C2}$ at a) 5%$\rho_N$, b) 50%$\rho_N$ and c) 95%$\rho_N$. The solid lines show fits to the data in the strain range $-1.8\% \leq \varepsilon \leq 0.7\%$.

| | $B_{C2}$ defined at 5%$\rho_N$ | | $B_{C2}$ defined at 50%$\rho_N$ | | $B_{C2}$ defined at 95%$\rho_N$ | |
|---|---|---|---|---|---|---|
| $T$ (K) | $p$ | $q$ | $p$ | $q$ | $p$ | $q$ |
| 8 | 0.45±0.23 | 2.22±0.08 | 1.46±0.19 | 3.06±0.13 | 2.42±0.30 | 4.00±0.13 |
| 10 | 0.37±0.21 | 2.17±0.11 | 1.10±0.21 | 3.03±0.14 | 1.73±0.30 | 3.93±0.15 |
| 12 | 0.32±0.17 | 2.12±0.09 | 0.74±0.09 | 3.01±0.19 | 1.08±0.15 | 3.85±0.16 |
| 14 | 0.42±0.14 | 2.13±0.10 | 0.63±0.05 | 2.99±0.11 | 0.76±0.04 | 3.81±0.18 |
| Global Fit | 0.39±0.19 | 2.16±0.10 | n/a | n/a | n/a | n/a |

**Table 5.7** Average values of $p$ and $q$ as a function of temperature for the Nb$_3$Al strand from the fits to the data in the strain range $-1.8\% \leq \varepsilon \leq 0.7\%$ where $B_{C2}$ is constrained by resistivity measurement.

95%$\rho_N$. The upper critical field values at 4.2 K are extrapolated values from the parameterisation detailed above (c.f. Eqn. (5.2)). Across the entire data set, a large shallow minimum in the error surface is found, leading to a wide range of acceptable $p$ and $q$ values consistent with the results shown in Fig. 5.15. The area of this shallow region is larger at 4.2 K and 6 K where it is not possible to measure close to $B_{C2}$. At higher temperatures, where measurement of $B_{C2}$ is possible, the minimum in the error surface tends to coincide with the upper critical field defined at 95%$\rho_N$, but the allowed range of $p$ and $q$ values is still very large.

The data from 8 K to 14 K, where the upper critical field was directly measured, were then refitted with $p$, $q$ and $C$ left unconstrained. $B_{C2}$ was constrained to the value at 5%$\rho_N$, 50%$\rho_N$ or 95%$\rho_N$. The values of $p$ and $q$ obtained from this fit to the data are shown in Figs. 5.21 and 5.22 respectively with averages denoted by the horizontal lines at each temperature. The data constrained at 5%$\rho_N$ is single valued – independent of temperature and strain within the errors of the measurement. The average values of $p$ and $q$ are $p = 0.39 \pm 0.19$ and $q = 2.16 \pm 0.10$. For $B_{C2}$ constrained at 50%$\rho_N$ and 95%$\rho_N$, $p$ and $q$ are both strong functions of temperature and $q$ is also a function of strain. The average values of $p$ and $q$ obtained for $B_{C2}$ constrained at 5%$\rho_N$, 50%$\rho_N$ or 95%$\rho_N$ at each temperature are shown in Table 5.7. We conclude that the value of $B_{C2}$ determined at 5%$\rho_N$ is required for $p$ and $q$ to be constant and hence for $F_P$ to scale accurately.
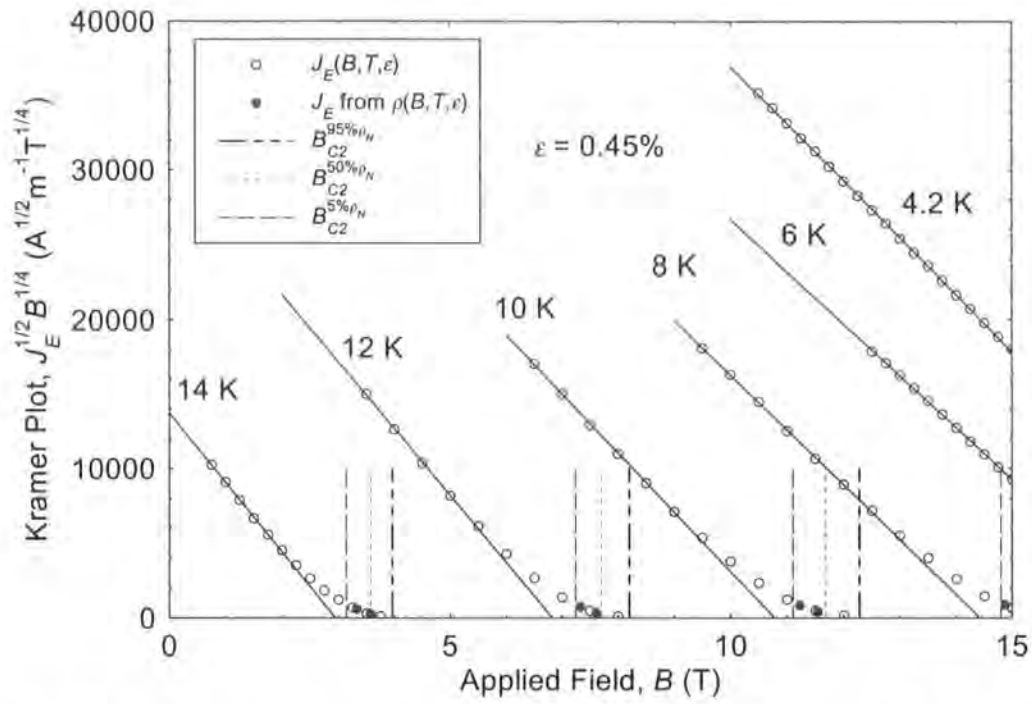
**Figure 5.23**Kramer plot as a function of temperature at $\varepsilon = 0.45\%$ for the Nb$_3$Al strand. The solid lines are fits to the data using a Kramer analysis of the data. The dashed lines indicate the upper critical field defined at $5\%\rho_N$, $50\%\rho_N$ and $95\%\rho_N$.
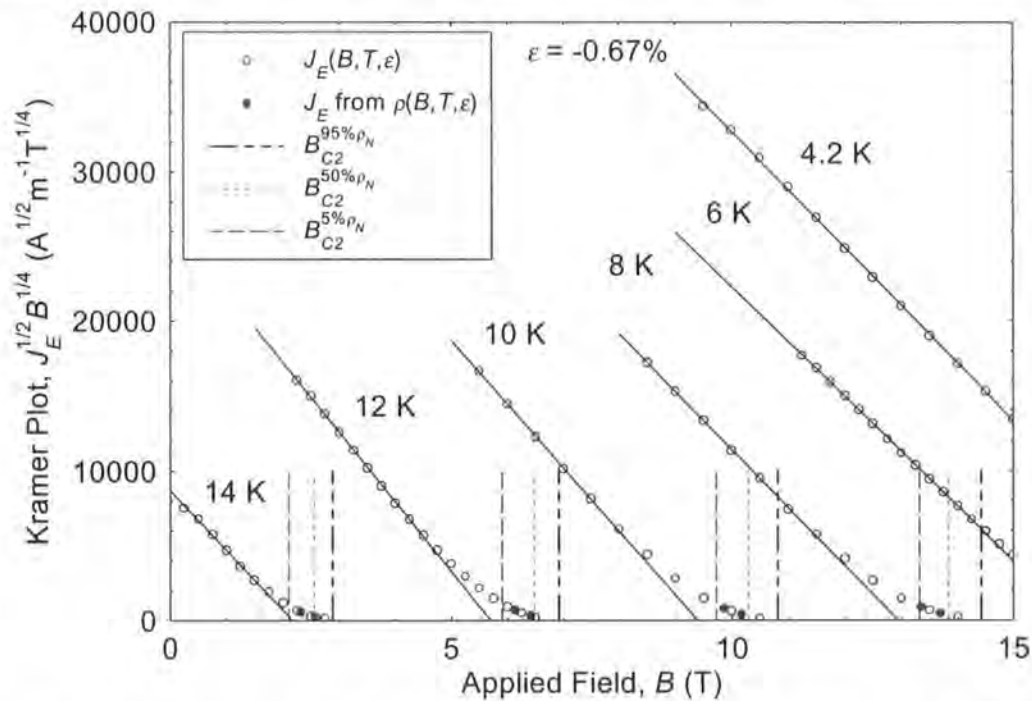


**Figure 5.24** Kramer plot as a function of temperature at $\varepsilon = -0.67\%$ for the Nb$_3$Al strand. The solid lines are fits to the data using a Kramer analysis of the data. The dashed lines indicate the upper critical field defined at $5\%\rho_N$, $50\%\rho_N$ and $95\%\rho_N$.

Since the values of $p$ and $q$ that produce good scaling are close to the Kramer values [95] of $p = 0.5$ and $q = 2$ that are very widely used [91, 97, 98, 128-130, 147, 148], this chapter also considers the implications of making the assumption that they are valid. The $J_E$ data presented in Figs. 5.10 and 5.11 have been replotted on a Kramer plot in Figs. 5.23 and 5.24. The straight line fits to the Kramer plots have been generated by ignoring the $I_C$ data below 5 A ($9.7 \times 10^6$ Am$^{-2}$). Also shown are the values for $B_{C2}$ obtained from the resistivity measurements. The extrapolated Kramer $B_{C2}$ value is typically 300 mT less than that defined at 5%$\rho_N$.

Using $p = 0.39$, $q = 2.16$ and constraining $B_{C2}^{\rho_N}(T, \varepsilon)$ at 5%$\rho_N$, the form of the prefactor can be determined from log-log plots of $C$ as a function of $B_{C2}^{\rho_N}$. Figure 5.25 plots $C(\varepsilon)$
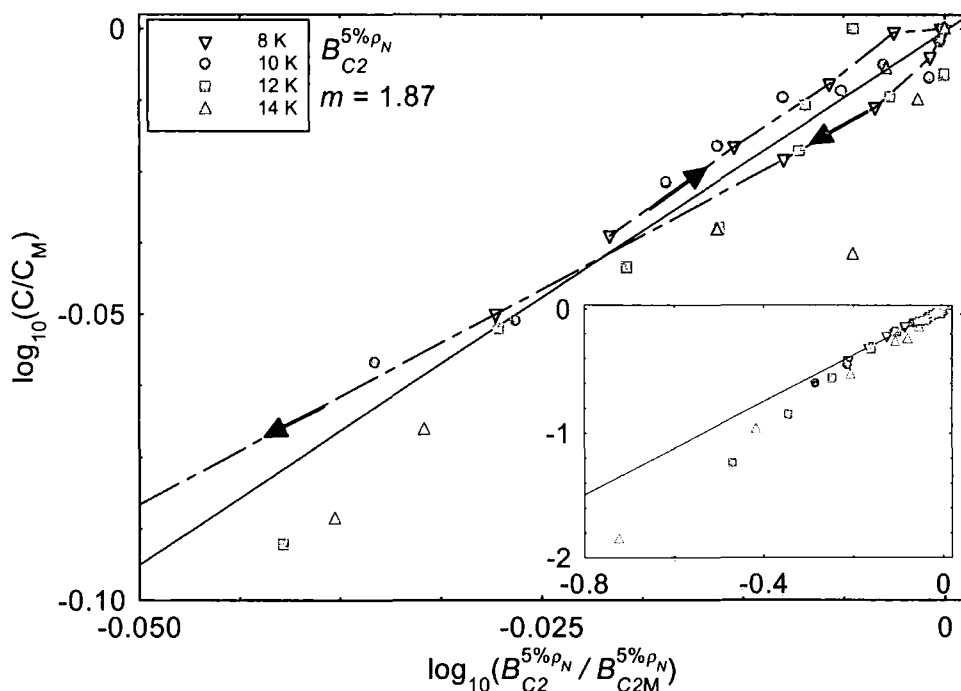


**Figure 5.25** Normalised log –log plot of the scaling law prefactor, $C$, against upper critical field as a function of strain at constant temperature for the Nb$_3$Al strand. The data were obtained from a fit constraining $B_{C2}$ at 5%$\rho_N$. $C_M$ and $B_{C2M}$ are the maximum values for the prefactor and upper critical field respectively. The main graph shows data typically in the strain range $-0.5 \leq \varepsilon \leq 0.7\%$ and the inset shows the entire data set. The solid line gives a global average for $m$. The dashed line indicates the hysteresis on the 8 K data. The arrows indicate decreasing strain.
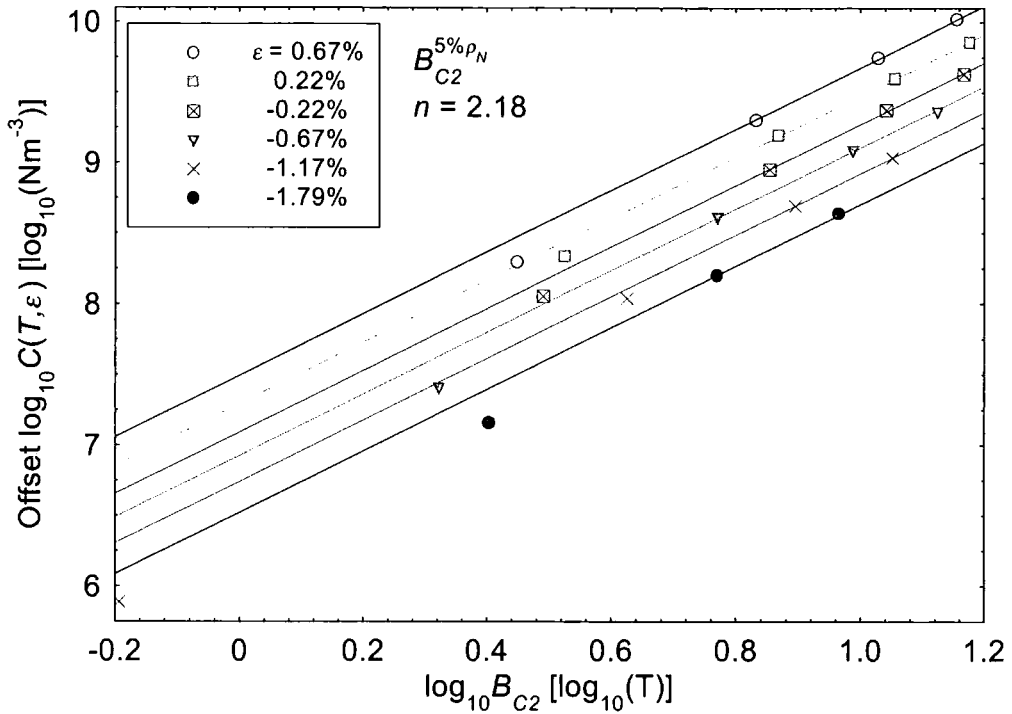
**Figure 5.26** Offset log –log plot of the scaling law prefactor, $C$, against upper critical field as a function of temperature at constant strain for the $Nb_3Al$ strand. The data were obtained from a fit constraining $B_{C2}$ at $5\%\rho_N$. Each curve is offset from the one above by 0.2. The solid lines give a global average for $n$.
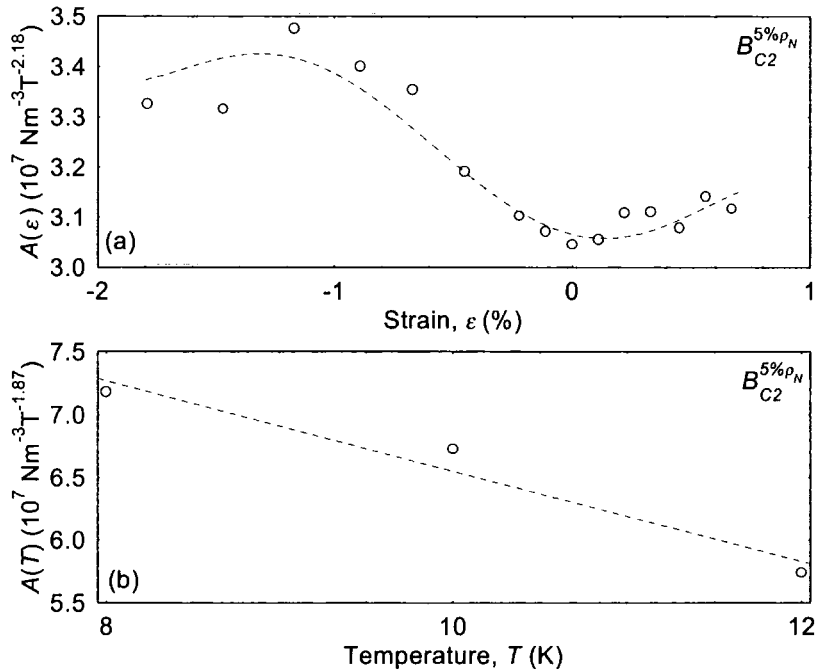


**Figure 5.27** Prefactor a) $A(\varepsilon)$ as a function of strain and b) $A(T)$ as a function of temperature from fits constraining upper critical field at $5\%\rho_N$ for the $Nb_3Al$ strand. The dashed lines are guides to the eye.
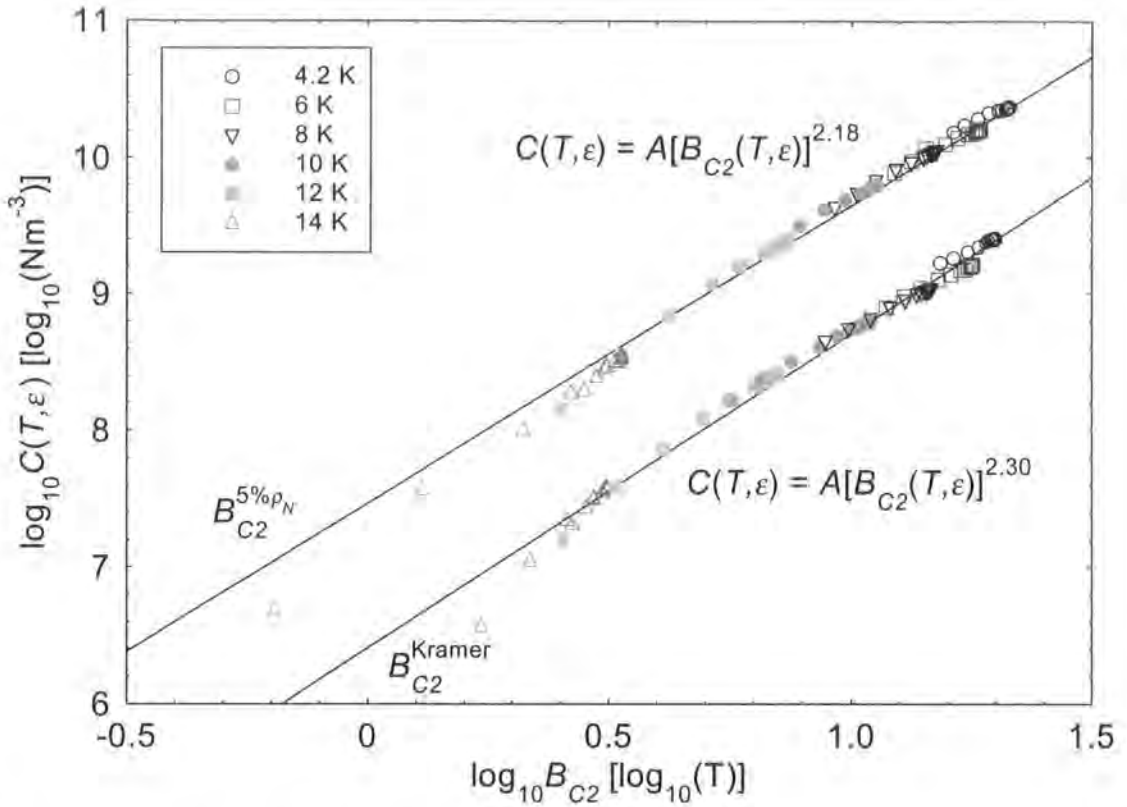
**Figure 5.28** Log –log plot of the scaling law prefactor, $C$, against upper critical field as a function of strain at constant temperature generated using $B_{C2}$ constrained at $5\%\rho_N$ and from a Kramer analysis of the data for the Nb$_3$Al strand. The solid lines are defined by the equations in the figure. The data from the Kramer analysis have been offset by $\log_{10}C = -1$.

as a function of $B_{C2}^{\rho_N}(\varepsilon)$ at constant temperatures to give $m$. The data has been normalised for clarity and show in detail the technologically important region from about $-0.5\% \le \varepsilon \le 0.7\%$. The inset graph shows the entire data set. Fig. 5.26 provides $C(T)$ as a function of $B_{C2}^{5\%\rho_N}(T)$ at constant strain which gives $n$. Here each data set is offset from the previous one by $\log_{10}(C) = -0.2$. In both figures, at high compressive strains and at 14 K linearity breaks down. It can be seen that $m$ and $n$ are almost independent of temperature. In the ranges $-0.5\% \le \varepsilon \le 0.7\%$ and $8\,\text{K} \le T \le 12$ K, $m = 1.87 \pm 0.08$ and $n = 2.18 \pm 0.02$. The associated parameters $A(\varepsilon)$ and $A(T)$ are presented in Fig. 5.27. The error in $m$ is a factor 4 higher than $n$. This occurs because at constant strain (when varying temperature) the prefactor $C$ is a unique function of $B_{C2}$,

whereas $C$ is a double-valued function of $B_{C2}$ (with varying strain) at constant temperature. Hence the parameterisation of the prefactor $C$ is most accurately achieved in the form of Eqn. (5.4) as found for $Nb_3Sn$ [108, 125]. In Fig. 5.28, a log-log plot of $C(T,\varepsilon)$ as a function of $B_{C2}(T,\varepsilon)$ is presented. The values of $B_{C2}$ at 4.2 K and 6 K are extrapolated values derived from the parameterisation using Eqn. (5.2). Equivalent data derived from the Kramer plots are also shown in Fig. 5.28 (offset by $\log_{10}(C) = -1$). This analysis therefore leads to a version of the flux pinning scaling law given by:

$$F_p = A(\varepsilon)\left[ B_{C2}^{5\%\rho_N}(T,\varepsilon) \right]^{2.18} b^{0.39} (1-b)^{2.16} \tag{5.7}$$

or for the Kramer parameterisation $n = 2.30 \pm 0.14$.

Although one can parameterise $C$ using Eqn. (5.7) or an equivalent Kramer form, it is clear that any complete description of $F_P$ must include the Ginzburg-Landau parameter, $\kappa(T,\varepsilon)$. Unfortunately $\kappa$ is not measured in transport measurements directly.
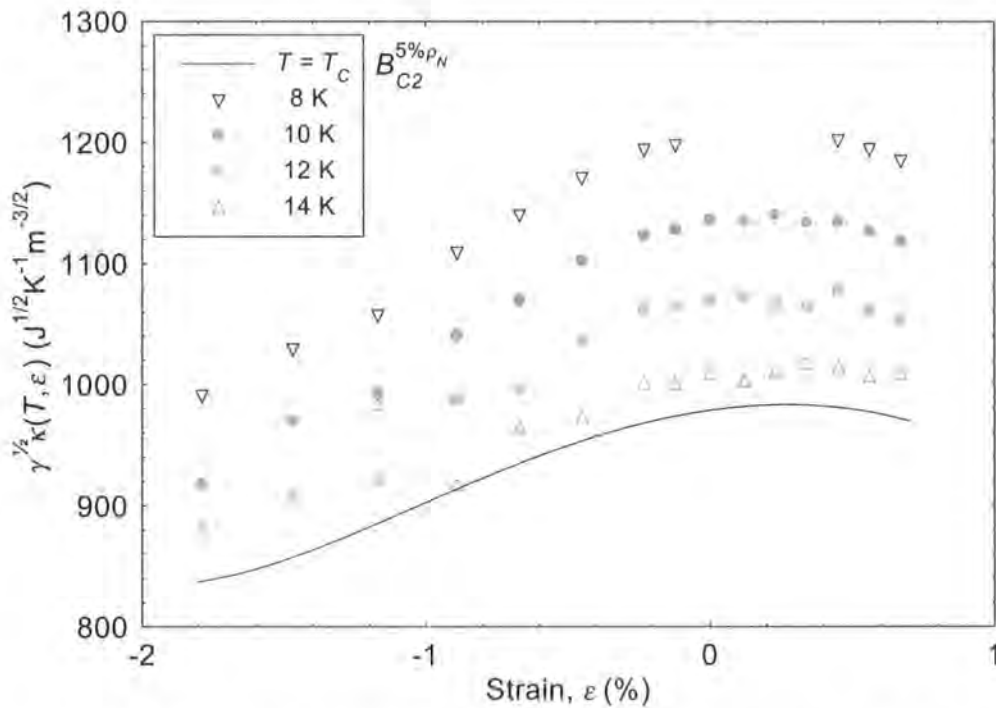


**Figure 5.29** The variation of the Ginzburg-Landau parameter $\kappa$ given by $\gamma^{1/2}\kappa$ as a function of strain and temperature for the $Nb_3Al$ strand when $B_{C2}$ is defined at $5\%\rho_N$. The solid line plots the calculated $\gamma^{1/2}\kappa$ at $T = T_C$.

Nevertheless we now consider how to incorporate $\kappa$ into the scaling law. Using the G-L equation for the thermodynamic critical field $B_C(0,\varepsilon) = 7.65 \times 10^{-4} \gamma^{\frac{1}{2}} T_C(\varepsilon)$ [26] with the two-fluid model for the temperature dependence $B_C(T,\varepsilon) = B_C(0,\varepsilon)\left[1 - t^2\right]$ and the G-L relation for the upper critical field $B_{C2}(T,\varepsilon) = \sqrt{2}\kappa(T,\varepsilon)B_C(T,\varepsilon)$, an empirical relation for $\kappa$ has been found of the form [128, 149]:

$$\kappa(T,\varepsilon) = \frac{B_{C2}(T,\varepsilon)}{\sqrt{2}B_C(T,\varepsilon)} = 924 \frac{B_{C2}(T,\varepsilon)}{\gamma^{\frac{1}{2}}(\varepsilon)T_C(\varepsilon)\left[1 - t^2\right]} \tag{5.8}$$

where $t = T/T_C(\varepsilon)$ and $\gamma$ is the electronic density of states. In Fig. 5.29, $\kappa\gamma^{\frac{1}{2}}$ is plotted as a function of strain. $T_C(\varepsilon)$ has been calculated from the fit to the $B_{C2}^{5\%\rho_N}(T,\varepsilon)$ data using Eqn. (5.2). There is a systematic dependence for $\kappa\gamma^{\frac{1}{2}}$ in the data as a function of strain and temperature except close to $T_C$. Equation (5.8) can be rewritten using Eqn. (5.2) and L'Hospital's rule [150] to give:
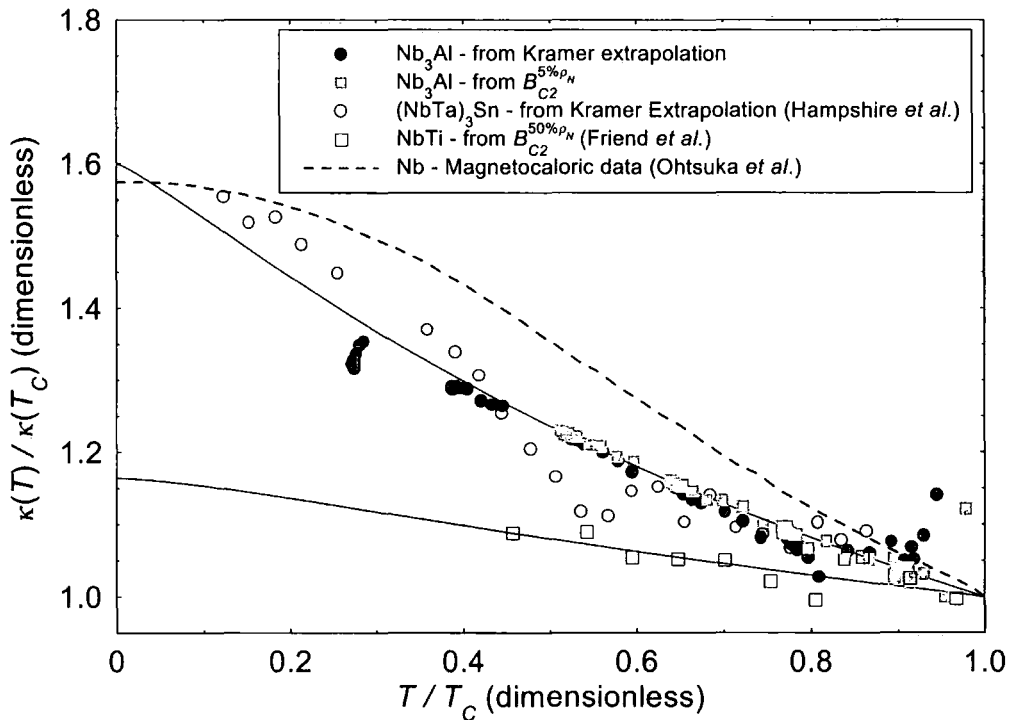


Figure 5.30 Normalised $\kappa$ as a function of reduced temperature for the Nb$_3$Al strand, a commercial NbTi strand [151], a commercial (NbTa)$_3$Sn [128] and a high purity Nb sample [152]. The solid lines show the different parameterisations of the data.

$$\frac{\kappa(T,\varepsilon)}{\kappa(T_C,\varepsilon)} = \frac{2}{\nu}\frac{\left[1-t^\nu\right]}{\left[1-t^2\right]}\tag{5.9}$$

To evaluate $\kappa$ at $T = T_C$, Eqn. (5.8) can be alternatively rewritten using L'Hospital's rule to give $\kappa(T_C,\varepsilon) = 924\dfrac{B_{C2}(0,\varepsilon)}{\gamma^{\frac{1}{2}}(\varepsilon)T_C(\varepsilon)}\dfrac{\nu}{2}$. Using the strain dependence of $B_{C2}(0,\varepsilon)$ and $T_C(\varepsilon)$ given in Table 5.6, and the value for $\nu$ in Table 5.5, the resulting dependence of $\kappa(T_C,\varepsilon)$ can be found. This has been plotted in Fig. 5.29 as a solid line. In order to calculate a value of $\kappa$, the density of states is required. Measurements on bulk Nb$_3$Al [153, 154] and thin films with varying stiochiometry [155] give a typical value for the electronic specific heat in Nb$_3$Al of $720 \pm 50$ JK$^{-2}$m$^{-3}$. This leads to value for $\kappa(T_C,\varepsilon = 0)$ calculated to be $36.5 \pm 1.3$ which can be compared to a value of $\sim 33$ for Nb$_3$Sn [156].
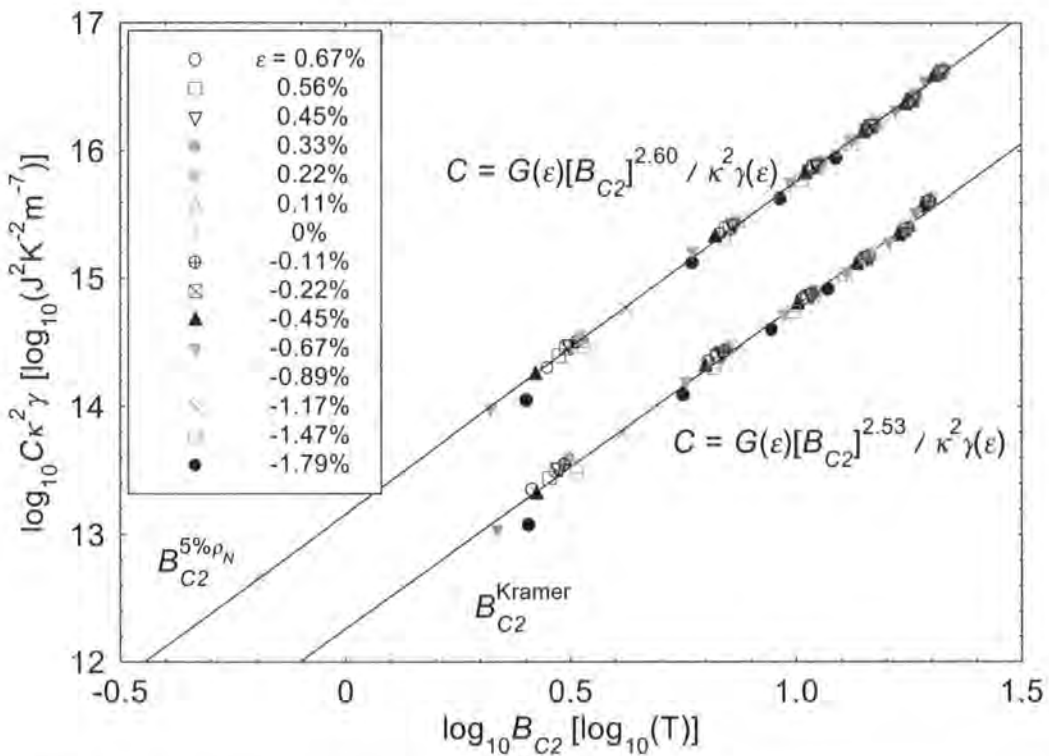


**Figure 5.31** Log-log plot of $C\gamma\kappa^2$ as a function of upper critical field and temperature at different strains generated using $B_{C2}$ constrained at 5%$\rho_N$ and from a Kramer analysis of the data for the Nb$_3$Al strand. The solid lines are lines of best fit to the entire data sets. The data from the Kramer analysis have been offset by log $C = -1$.

**$B_{C2}$ defined at 5%$\rho_N$**

| Strain, $\varepsilon$ (%) | -1.79 | -1.47 | -1.17 | -0.89 | -0.67 | -0.45 | -0.22 | -0.11 | 0 | 0.11 | 0.22 | 0.33 | 0.45 | 0.56 | 0.67 |
|---|---|---|---|---|---|---|---|---|---|---|---|---|---|---|---|
| $n$ | 2.77 | 2.67 | 2.59 | 2.57 | 2.62 | 2.60 | 2.56 | 2.58 | 2.58 | 2.58 | 2.57 | 2.60 | 2.55 | 2.57 | 2.60 |
| $G(\varepsilon)$ ($10^{13}$ J$^2$K$^{-2}$m$^{-7}$) | 0.888 | 1.14 | 1.47 | 1.63 | 1.41 | 1.45 | 1.59 | 1.52 | 1.51 | 1.51 | 1.59 | 1.47 | 1.65 | 1.56 | 1.41 |
| $T_C$ (K) | 13.40 | 13.84 | 14.30 | 14.67 | 15.05 | 15.31 | 15.50 | 15.59 | 15.63 | 15.64 | 15.61 | 15.59 | 15.50 | 15.43 | 15.35 |

**$B_{C2}$ defined from Kramer analysis**

| Strain, $\varepsilon$ (%) | -1.79 | -1.47 | -1.17 | -0.89 | -0.67 | -0.45 | -0.22 | -0.11 | 0 | 0.11 | 0.22 | 0.33 | 0.45 | 0.56 | 0.67 |
|---|---|---|---|---|---|---|---|---|---|---|---|---|---|---|---|
| $n$ | 2.78 | 2.60 | 2.52 | 2.81 | 2.61 | 2.56 | 2.48 | 2.48 | 2.47 | 2.47 | 2.47 | 2.47 | 2.46 | 2.45 | 2.44 |
| $G(\varepsilon)$ ($10^{13}$ J$^2$K$^{-2}$m$^{-7}$) | 0.728 | 1.13 | 1.41 | 0.708 | 1.18 | 1.38 | 1.70 | 2.15 | 2.19 | 2.22 | 2.25 | 2.18 | 2.27 | 2.20 | 2.26 |
| $T_C$ (K) | 13.44 | 13.83 | 14.25 | 14.82 | 15.06 | 15.29 | 15.42 | 15.49 | 15.51 | 15.52 | 15.51 | 15.48 | 15.41 | 15.36 | 15.24 |

**Table 5.8** The exponent of the flux pinning scaling law $n$, prefactor $G(\varepsilon)$ and $T_C$ as a function of strain when $B_{C2}$ is constrained at 5%$\rho_N$ and using a Kramer analysis for the Nb$_3$Al strand.

The data in Fig. 5.29 have been normalised at $T_C$ and replotted in Fig. 5.30. Figure 5.30 includes normalised kappa values derived using $B_{C2}$ from the Kramer plots for the $Nb_3Al$ strand; values derived from the literature for $(NbTa)_3Sn$ [128], and NbTi [151]; solid lines showing Eqn. (5.9) for different values of $v$, and experimental data for Nb from the literature [152]. The A15 compounds show reasonably constant values. In Fig. 5.31, $C\kappa^2\gamma$ is plotted as a function of the upper critical field and temperature at different strains on a log-log plot. The data at each strain were individually fitted using a linear function. The gradient was found to be $n = 2.60 \pm 0.06$ with an intercept of $C\kappa^2\gamma = (1.44 \pm 0.25) \times 10^{13}$ $J^2K^{-2}m^{-7}$. The equivalent data using the Kramer analysis has also been plotted on Fig. 5.31, but offset from the data where $B_{C2}$ is constrained at $5\%\rho_N$ by $\log_{10}(C\kappa^2\gamma) = -1$. This procedure was repeated for the Kramer analysis resulting in $n = 2.53 \pm 0.12$ and an intercept of $C\kappa^2\gamma = (1.62 \pm 0.70) \times 10^{13}$ $J^2K^{-2}m^{-7}$. The linearity in Fig. 5.31 implies that to a good approximation:

$$C(T,\varepsilon) = G(\varepsilon)\frac{\left[B_{C2}^{5\%\rho_N}(T,\varepsilon)\right]^{2.60}}{\kappa^2(T,\varepsilon)\gamma(\varepsilon)} \qquad (5.10)$$

Hence the temperature dependence of $C(T,\varepsilon)$ is accurately characterised by the factor $\dfrac{\left[B_{C2}^{5\%\rho_N}(T,\varepsilon)\right]^{2.60}}{\kappa^2(T,\varepsilon)}$. There is no need for any additional temperature dependent terms.

Uncertainty in the intercept values in Fig. 5.31 lead to a relatively large uncertainty in $G(\varepsilon)$ of about 15%. $G(\varepsilon)$, $n$ and $T_C(\varepsilon)$ are tabulated as a function of strain in Table 5.8 for the analysis where $B_{C2}$ is defined at $5\%\rho_N$ using $p = 0.39$ and $q = 2.16$ and the Kramer analysis using $p = 0.5$ and $q = 2$. $G(\varepsilon)$ is very broadly consistent with an inverse parabola with a value about 40% lower at strong compression than its peak value at 0.11% strain. To the author's knowledge, the uniaxial strain dependence of the density of states in $Nb_3Al$ has not been reported. However hydrostatic measurements on $Nb_3Sn$ [157], show that a change in $T_C$ of ~0.35 K produces a change in $\gamma(\varepsilon)$ of ~ 8%. In the strain measurements presented here on $Nb_3Al$, $T_C$ changed by about 2 K, so we tentatively attribute the 40% change in $G(\varepsilon)$ to the strain dependence of $\gamma(\varepsilon)$. Hence Eqn (5.7) becomes:

$$F_p = \frac{1}{337} \frac{\left[B_{C2}^{5\%\rho_N}(T,\varepsilon)\right]^{2.60}}{(2\pi\Phi_0)^{\frac{1}{2}} \mu_0 \kappa^2(T,\varepsilon)} b^{0.39} (1-b)^{2.16} \qquad (5.11)$$

or for the Kramer analysis in which $I_C$ values below 5 A are ignored, and $n$ is set to $\frac{5}{2}$ :

$$F_p \approx \frac{1}{249} \frac{\left[B_{C2}(T,\varepsilon)\right]^{\frac{5}{2}}}{(2\pi\Phi_0)^{\frac{1}{2}} \mu_0 \kappa^2(T,\varepsilon)} b^{\frac{1}{2}} (1-b)^2 \qquad (5.12)$$

Both Eqns. (5.11) and (5.12) provide expressions for $F_p$, which are only dependent on fundamental constants.

Figure 5.32 presents the RMS $I_C B$ error surface for the all of the data in the temperature range 8 K $\leq T \leq$ 14 K as a function of $p$ and $q$ when $B_{C2}$ is constrained at 5%$\rho_N$. The values of $p$ and $q$ used in the empirical fit are close to the minimum in the error surface
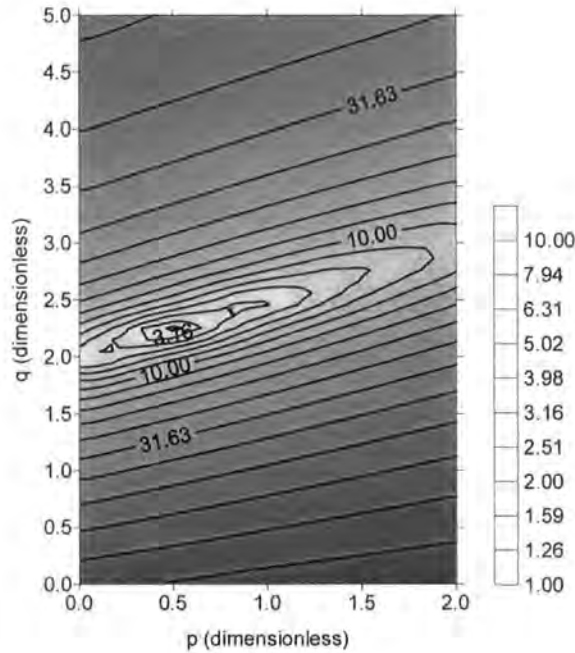


**Figure 5.32** RMS $I_C B$ error surface plot as a function of $p$ and $q$ for all data in the temperature range 8 K $\leq T \leq$ 14 K for the Nb$_3$Al strand. The upper critical field in the fitting procedure was constrained at 5%$\rho_N$. The contours on the error surface are logarithmically spaced per decade as indicated on the legend.

as expected and show a larger uncertainty in $p$ than $q$. The surface also shows that $p = 0.5$ and $q = 2$ (i.e. Kramer values) and $p = 1$, $q = 2.5$ can both reasonably well parameterise the data. In assuming half-integral values of $p$ and $q$, comparison can be made with theoretical models [144]. This work has followed through the implications of Kramer values to facilitate comparison with other measurements in the literature on $Nb_3Al$ where it has been assumed that the Kramer functional form holds [83, 126, 129, 130].

## 5.6 Discussion

There is natural concern about whether there is significant strain gradient across the wire cross-section during compressive measurements using short bending springs [158, 159]. The resistivity measurements of upper critical field to $\varepsilon = -1.8\%$ (c.f. Figs. 5.13, 5.17 and 5.18) show positive and negative curvature in compression, independently of the criterion used to define $T_C$ and $B_{C2}$ such that they cannot be described by an empirical power-law expression [99]. In general, the strain tolerance of $B_{C2}$ is dependent on the strain tolerance of the density of states, which is complex. It is clear that a more complete description of the strain state of conductor is needed [86, 146, 160] to progress beyond parameterisation to understanding. Nevertheless we suggest that there are three aspects to the data that suggest that strain non-uniformity in the sample is not significant and that the data are representative of the strain values quoted: the resistive transition width for these data (c.f. Fig. 5.12) was independent of strain for $-1\% \leq \varepsilon \leq 0.7\%$, and only increased slightly at higher strains when the spring was being plastically deformed to $-1.8\%$ from 1.0 T to $\sim$1.1 T. The data obtained on all samples to date are consistent with free-standing axial tension measurements (c.f. Fig. 5.14). Finally the parameterisation proposed, holds throughout the entire strain-temperature phase space until $B_{C2}$ is below about 2 T. Although it was not possible to check the reversibility of the strand after it was cycled to $-1.8\%$, the width of the resistivity transition, the systematic dependence of the $N$-value (Figs. 5.7 and 5.9) and the fact that the parameterisation holds over the entire strain-temperature phase space suggest that the sample was not damaged.

Previous measurements at zero strain on a powder-route $Nb_3Al$ wire [145] have been parameterised by assuming $p$ and $q$ are the Kramer values and treating $T_C(\varepsilon)$ and $B_{C2}(T,\varepsilon)$ as fitting parameters. This gave $\nu = 1.5$. Measurements at zero strain on a high temperature reacted jelly-roll $Nb_3Al$ wire [127], where $B_{C2}$ was defined at $B_{C2}^{50\%\rho_N}(0,\varepsilon)$, gave values of $p = 0.52$, $q = 2.7$, $n = 3.73$ and $\nu = 1.4$. Measurements of $J_E$ as a function of strain and temperature on a bronze route $Nb_3Sn$ conductor [108] made in high-fields until $J_E = 0$ (i.e. $J_E$ is parameterised into the tail of the $J_E(B)$ characteristic) gave $p = 0.5$, $q = 3.5$, $n = 3.1$ and $\nu = 1.5$. These sets of values are consistent with the higher values found for the technological fit in Table 5.1 compared to those derived from direct resistivity measurements in Table 5.5 and subsequent parameterisation (Eqns. (5.7), (5.11) and (5.12)) where $B_{C2}(T,\varepsilon)$ is defined near the onset of zero resistance from the resistivity data. This approach in fact gives values for the fitting parameters $B_{C2}(T,\varepsilon)$ close to those at $95\%\rho_N$. However it has been shown in this $Nb_3Al$ strand work, that $p$ and $q$ are strong functions of temperature (and strain) when the upper critical field is defined at $B_{C2}^{50\%\rho_N}$ and $B_{C2}^{95\%\rho_N}$ (c.f. Figs. 5.21(b, c) and 5.22(b, c)). Necessarily the parameterisation can only be an averaged value of this strong temperature dependence – unless one adds in the complexity of functional forms for $p$ and $q$. Furthermore it is well known that if there is a broad distribution in $B_{C2}$, and $J_E$ is parameterised in the tail, this tends to increase the value of $q$ [161]. Certainly, for materials with a unique value of $B_{C2}$, making measurements until $J_E$ is zero (i.e. up to $B_{C2}$) would be the natural way to identify $B_{C2}$ and break any correlation between $p$, $q$ and $B_{C2}$ in the fitting. However, in this inhomogeneous technological $Nb_3Al$ material, such an approach characterises the high $B_{C2}$ values in the distribution. This produces a breakdown in scaling and reduces the accuracy of the parameterisation. Furthermore the correlations between the fitting parameters (c.f. Fig. 5.20) mean that $p$, $q$, and $\nu$ are artificially increased to parameterise the tail.

Experimental values for $n$ for low temperature type-II superconductors such as NbTi [151], $V_3Ga$ [58], $Nb_3Al$ [83], $Nb_3Sn$ [128] and $PbMo_6S_8$ [147, 148, 162] are in the range $2 \le n \le 3$. Hence the values of $n$ obtained from constraining $B_{C2}$ at $5\%\rho_N$ are consistent with both the theoretical [144] and experimental values in the literature. Equally, variable strain measurements at 4.2 K on low temperature superconductors

gave $m$ = 1, 1.2, 1.4, 1.6 and 4 for Nb$_3$Sn, Nb$_3$Sn with Hf and Ga additions, V$_3$Ga, Nb$_3$Ge and NbTi respectively [163, 164]. There is a general trend that $m$ increases as the sensitivity of the normalised upper critical field to strain decreases. This correlation is consistent with the increase in $m$ from 0.86 to 2.14 for a Nb$_3$Sn conductor produced by an extra Hot Isostatic Pressing reaction which also reduced the strain sensitivity of normalised $B_{C2}$ as described in chapter 4 [91]. It is also consistent with the high value of $m$ observed here for the Nb$_3$Al strand.

Having concluded that measurements of $J_E$ in the tail included in the parameterisation contribute to a breakdown of scaling, the issue of how to identify a characteristic or average value for $B_{C2}$ of the bulk of the Nb$_3$Al remains. The approach of Kroeger et al. [124] has been adopted to find $B_{C2}$ from resistivity measurements. In the high current limit, Kroeger pointed out that the resistivity measurement maps out more of the $J_E$ surface. However at sufficiently low currents, we have found that the shape of the resistivity transition is reasonably independent of sample current. In this low current regime, we associate the width in the resistivity transition with the distribution in the upper critical field. In the limit that the width is independent of current we can also assume there are no flux creep effects [165, 166]. The onset of resistance ($\approx B_{C2}^{5\%\rho_N}(T,\varepsilon)$) means that there is no percolative superconducting path. Theoretical work on percolative networks show that in a 2 dimensional system this occurs when about 40% of the material is normal [167, 168]. In 3 dimensions, 70 – 75% must go normal before there is no percolative superconducting path and the resistive transition begins [168, 169]. Although these theoretical percentage values are dependent on how the connectivity of network is constructed, experimental support for these results has been observed in superconducting systems [170, 171]. Further work is required to model the percolative current path through the Nb$_3$Al filaments during the resistive transition. Information about compositional variations in Nb and Al across the filament and the properties of the grain boundaries will both be required. If the volumetric distribution and spatial distribution in $B_{C2}$ can be calculated, understanding the mechanism that determines $J_E$ will be required to identify the characteristic $B_{C2}$ value from the distribution for the scaling law. Despite these complexities, we interpret
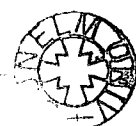
$B_{C2}^{5\%\rho_N}(T, \varepsilon)$ as the approximate field at which there are no superconducting percolative paths and equate it to the characteristic upper critical field in the scaling law.

From an engineering perspective where the most accurate description of $J_E$ is required for all possible $B$-$T$-$\varepsilon$ conditions, the technological fit provided is appropriate. For much of the temperature-strain phase space, this can be closely approximated by the empirical law (Eqn. (5.7)) that self-consistently describes variable-temperature and variable-strain data as was found for Nb$_3$Sn [108]. Kroeger et al. [124] found very different results on their high bronze-niobium ratio monofilament to those reported here. The strain at which the peak in $J_E$ and $B_{C2}$ occurred differed by about 0.3%; the index $n$ varied by about 25% and the prefactor $A(\varepsilon)$ varied by about a factor 3. In comparison, for the Nb$_3$Al reported here (and the Nb$_3$Sn multifilamentary conductor reported previously [108]) – the peak in $J_E$ and $B_{C2}$ occurred at about the same strain, the variation in $n$ as a function of strain is a few percent and $A(\varepsilon)$ changes by ~ 10% in the equivalent strain range. Further work would be required to determine to what degree these marked differences are due to the different materials investigated and/or due to the different limit in which the resistivity data have been measured from which $B_{C2}$ has then been extracted.

The empirical law has also been rewritten in terms of fundamental constants including $\kappa$. The magnitude and temperature dependence of the functional form accurately describe the $J_E$ data at all strains as shown in Fig. 5.31 and is consistent with zero-strain variable-temperature $J_E$ data on (NbTa)$_3$Sn [128]. The strain dependence is not explicitly confirmed because it is not possible from transport measurements alone to determine the strain dependence of $\kappa$. Nevertheless, agreement between the functional form and data is consistent with a reasonable strain dependence for the electronic density of states (from which the strain dependence of $\kappa$ can be calculated – Eqn. (5.8)). The denominator in $F_P$ given by Eqns. (5.11) and (5.12) has a $\kappa^2$ term. If it is replaced by $\kappa$, one can only obtain agreement if the electronic density of states, $\gamma(\varepsilon)$, increases as $T_C$ decreases which is unphysical. If it is replaced by $\kappa^3$ (or higher powers), one has to postulate an unreasonably strong strain dependence for $\gamma(\varepsilon)$. In this context the difference between $n$ and $m$ in the prefactors for the scaling law (Eqns. (5.3) and (5.4))

is attributed to the strain dependence of kappa and the exponent value for $\kappa$ of 2 is required.

An interesting feature of the functional form is that the primary multiplicative constant (i.e. 1/337 and 1/249 in Eqns (5.11) and (5.12) respectively) is dimensionless. This implies that there is no requirement to add a constant grain size factor into the functional form. It is well established that in low fields, $J_E$ is approximately inversely proportional to the grain size [172]. Nevertheless Kramer pointed out in the 1970's that the high field functional form of many superconductors approaches a limiting value that
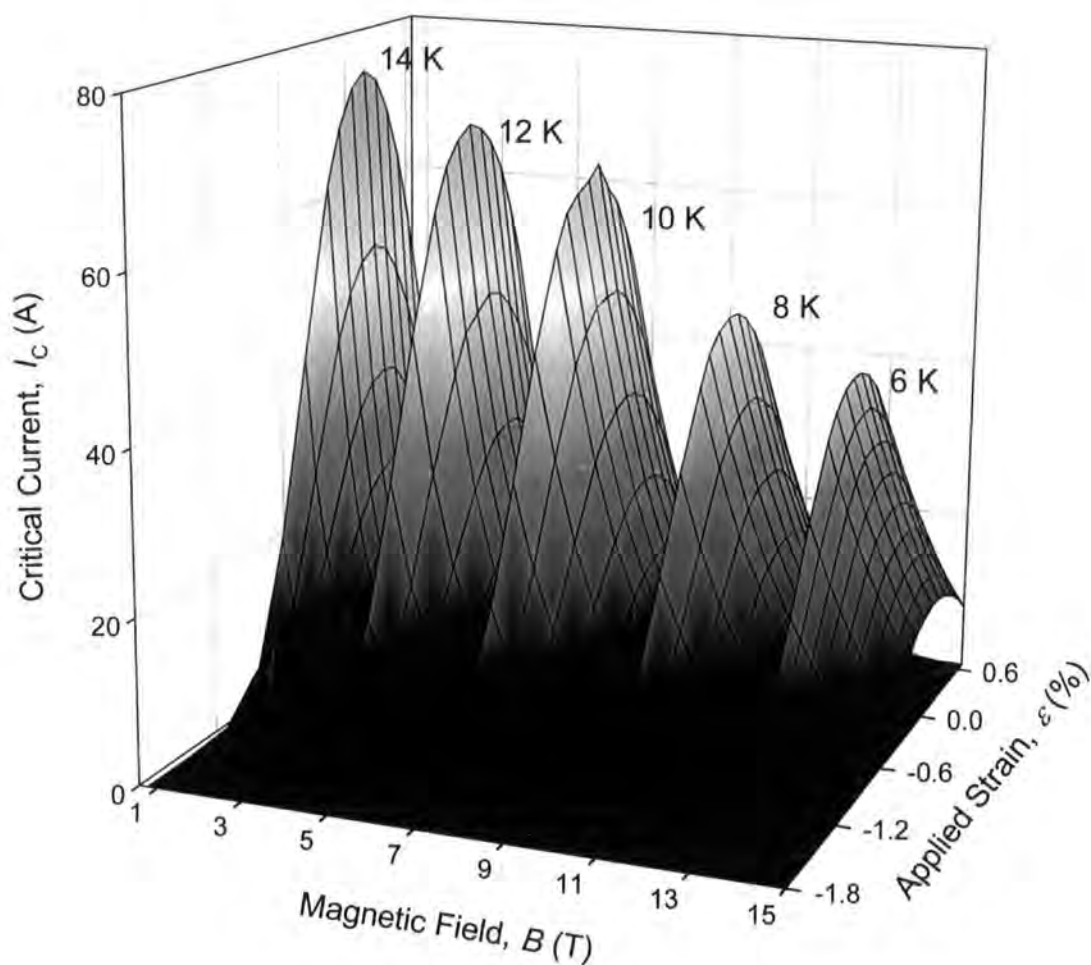


**Figure 5.33** The four-dimensional critical current surface as a function of magnetic field, temperature and strain for the Nb$_3$Al strand.

is well below (typically a few percent [156] of) the depairing current [173, 174]. For example comparison between Nb₃Sn material with different grain sizes [175] or the Chevrel phase $SnMo_6S_8$ [176] shows a clear saturation at the highest fields. There is no consensus explanation for saturation [156, 173, 174]. However we conclude that in high fields, the functional form of $F_P$ suggests that $J_E$ is not dependent on grain-size, consistent with $J_E$-microstructure correlations in other A15 and Chevrel phase superconducting materials.

## 5.7) Summary and Conclusions

Detailed, accurate measurements of critical current density and upper critical field have been made on a technological Nb₃Al conductor in magnetic fields up to 15 T, temperatures from 4.2 K up to the critical temperature and in the strain range from -1.8% to 0.7% as shown in Fig. 5.33. Improvements to the design of the probe mean that the uncertainty in temperature above 4.2 K is equivalent to an uncertainty of ± 100 mK with a stability during the measurements of < 5 mK. The limiting current at 4.2 K is 200 A and from 6 to 14 K is 80 A. The typical noise level on these measurements has been reduced to 1 µVm⁻¹ allowing $J_E$ to be defined at 10 µVm⁻¹. These improvements have also allowed reliable measurements of the index of transition, $N$, throughout the temperature range. Complementary resistivity measurements were taken, to determine the upper critical field ($B_{C2}(T,\varepsilon)$) and the critical temperature ($T_C(\varepsilon)$) directly. At low currents the shape of the resistivity curve is only weakly dependant on the sample current. In this regime, when $B_{C2}(T,\varepsilon)$ is defined at 5%$\rho_N$, 50%$\rho_N$ or 95%$\rho_N$,

an empirical relation is found where $B_{C2}^{\rho_N}(T,\varepsilon) = B_{C2}^{\rho_N}(0,\varepsilon)\left[1 - \left(\frac{T}{T_C^{\rho_N}(\varepsilon)}\right)^\nu\right]$ and an

approximate relation $B_{C2}^{\rho_N}(0,\varepsilon) = 3.60 \times T_C^{\rho_N}(\varepsilon) - 29.86$ holds. The $J_E$ data have been parameterised using the volume pinning force ($F_P$) where: $F_P = J_E B = A(\varepsilon)B_{C2}^n(T,\varepsilon)b^p(1-b)^q$ and $b = B/B_{C2}(T,\varepsilon)$. $J_E$ is reversible in the strain range $-0.5\% < \varepsilon < 0.7\%$. To achieve an accuracy of ~1 Amp, $B_{C2}(T,\varepsilon)$ was described by the empirical relation and three different ranges of temperature-strain were considered. The constants $p$, $q$, $n$ and $\nu$ and the strain-dependant variables $A(\varepsilon)$, $B_{C2}(0,\varepsilon)$ and $T_C(\varepsilon)$ have been treated as free-parameters and determined in each range.

When $B_{C2}(T, \varepsilon)$ is constrained to be the value at 50%$\rho_N$ or 95%$\rho_N$, the scaling law for $F_P$ breaks down such that $p$ and $q$ are strong functions of temperature and $q$ is also a strong function of strain. However when $B_{C2}(T, \varepsilon)$ is defined at 5%$\rho_N$, there is good scaling where $p$ and $q$ are constants – independent of temperature and strain. If low $J_E$ values in the high-field tail of the $J_E$-$B$ relations are ignored, $v = 1.25$, $n = 2.18$, $p = 0.39$ and $q = 2.16$. $F_P$ can also be approximated by a Kramer form

$$F_P = \frac{1}{249} \frac{[B_{C2}(T, \varepsilon)]^{\frac{5}{2}}}{(2\pi\Phi_0)^{\frac{1}{2}} \mu_0 \kappa^2(T, \varepsilon)} b^{\frac{1}{2}} (1-b)^2, \text{ where } \kappa(T, \varepsilon) = 924 \frac{B_{C2}(T, \varepsilon)}{\gamma^{\frac{1}{2}}(\varepsilon) T_C(\varepsilon)(1-t^2)} \propto \frac{2(1-t^v)}{v(1-t^2)}, \gamma$$

is the density of states and $t = T / T_C(\varepsilon)$.


Good scaling implies that $B_{C2}^{5\%\rho_N}(T, \varepsilon)$ provides the characteristic (or average) upper critical field of the bulk material although $J_E$ is non-zero above $B_{C2}^{5\%\rho_N}(T, \varepsilon)$ and the current flow is percolative. Furthermore since $J_E$ is described using a scaling law that incorporates fundamental constants alone, it suggests that in high fields $J_E$ is not dependant on grain-size, consistent with $J_E$-microstructure correlations in other superconducting phase materials.

# Chapter 6

# Future Work

This thesis has presented comprehensive measurements of $J_E$ as a function of magnetic field, temperature and strain for state-of-the-art technological $Nb_3Sn$ and $Nb_3Al$ strands. These data have suggested that there is one unified temperature and strain scaling law for describing the mechanism for $J_E$ in these materials. Future studies for developing the work presented in this thesis are outlined below.

In fitting the $J_E$ data to obtain the unified scaling law, the high field tail in the $J_E$ data has been ignored. It is assumed that the tail is due to a reduced cross-sectional area of the superconductor carrying a percolative supercurrent because of a distribution in $B_{C2}$ in the strand. The measurements presented in this thesis are for $J_E$ defined at 10 $\mu Vm^{-1}$, and are the lowest for this type of measurement in the literature but ideally the values of $J_E$ should be criteria independent. In order to explain the tail in the $J_E$ data, measurements of $E$-$J$ characteristics at lower $E$-field sensitivity are required so that the $E$-field criteria dependence in defining $J_C$ is removed. This should be coupled with measurements at lower critical current densities so that a more accurate determination of $B_{C2}$ from an extrapolation of the $J_C$ data is possible. These improvements should also determine whether or not there is a presence of an irreversibility field in $Nb_3Sn$ and $Nb_3Al$.

Measurements should also be extended to lower magnetic fields. The mechanism for flux pinning, and therefore $J_E$, has found to be different for certain materials in the low field regime compared to the high field regime. This has been previously possible at high temperatures such as 12 K and 14 K, but needs to be extended to lower temperatures. In order to expand the range over which the data was taken, information obtained from the three independent thermometers measuring the temperature gradient along the spring can be used. It was seen that there was heating at the top and bottom of the spring probably due to current transfer and resistive heating in the copper sections of the current leads. This heating limits the maximum current attainable during the

measurement. Relocation and completely independent control of the heaters will allow a significant improvement in the range of data attainable. Methods of further reducing the current transfer/resistive heating should also be investigated. This will provide important information about the materials in low magnetic fields, and test the applicability of the unified scaling law in terms of fundamental constants as presented in chapter 5 in such a regime.

At the moment, the unified scaling law has just been tested on one $Nb_3Al$ strand. These measurements need to be extended to different to different types of $Nb_3Al$ conductor such as the high stiochiometry $Nb_3Al$ conductors, as well as to other low temperature superconductors. NbTi is an ideal material for testing as it has a high tolerance to strain, is ductile, and does not have the problems with voids that are seen in $Nb_3Sn$ due to the diffusion reaction required to prepare the material. Single filaments can also be extracted from commercial strands relatively easily which is not possible for $Nb_3Sn$ or $Nb_3Al$. Other $A15$ materials such as $Nb_3Sn$ and the Chevrel Phase $PbMo_6S_8$ should also be tested, however care must be taken to provide high quality samples so that the intrinsic properties of the superconductor are studied and not any extrinsic properties.

As stated in chapter 4, the measurements performed on the hot isostatic pressed (HIP'ed) $Nb_3Sn$ were preliminary measurements that yielded an interesting result. The $J_E$ data taken at 4.2 K as a function of strain, and the exponent of upper critical field in the flux pinning scaling law $F_P = A[B_{C2}]^n f(b)$ was found to increase from 0.86 for the unHIP'ed sample to 2.14 for the HIP'ed sample. It should be noted that the value obtained for the unHIP'ed sample is consistent with other $Nb_3Sn$ samples, whereas the value for the HIP'ed samples is consistent with measurements on $Nb_3Sn$ as a function of temperature at constant strain. This change is attributed to a microstructural change is the wire by closing the voids in the $Nb_3Sn$ strand. Measurements on HIP'ed $Nb_3Sn$ need to be extended to compressive strains and as a function of temperature to $T_C$. A similar analysis can then be performed to the $Nb_3Al$ data presented in chapter 5 to investigate if the HIP reaction leads to one unified scaling law in $Nb_3Sn$ as suggested by the result at 4.2 K. Comparison with similar measurements on unHIP'ed $Nb_3Sn$ samples will help illuminate the role of intrinsic and extrinsic properties with respect to a unified scaling law.

An interesting extension to this work would be to measure the fundamental parameters of bulk $Nb_3Al$ (following Lim *et al.* for $Nb_3Sn$ [157]) as a function of hydrostatic strain, temperature and magnetic field. Measurement of the normal state resistivity, upper critical field and critical temperature would be fairly straight forward, and measurement of the superconducting energy gap should be possible using a technique such as infrared absorption. These measurements will allow calculation of the electronic specific heat of the material, as well as fundamental parameters such as the Ginzburg-Landau parameter $\kappa$ and the thermodynamic critical field $H_C$ as a function of strain, and so may provide information on the mechanism for superconductivity on a more theoretical level. Comparison of the critical temperature and upper critical field measured on the bending spring and under hydrostatic strain will also be possible and may provide insight into the tensorial strain state of the samples measured on the bending spring.

# References

[1]    Onnes H K 1908 The liquefaction of helium *Comm. Leiden* **108** 168-185

[2]    Onnes H K 1911 Further experiments with liquid helium. G. On the electrical resistance of pure metals VI. On the sudden change in the rate at which the resistance of mercury disappears. *Comm. Leiden* **124c** 21-26

[3]    Poole C F, Jr., Farach H A and Creswick R J 1995 *Superconductivity* (Academic Press Inc.)

[4]    Wu M K, Ashburn J R, Torng C J, Hor P H, Meng R L, Gao L, Huang Z J, Wang Y Q and Chu C W 1987 Superconductivity at 93 K in a new mixed-phase Y-Ba-Cu-O compound system at ambient pressure *Phys. Rev. Lett.* **58** 908-910

[5]    Quinn D J, III and Ittner W B, III 1962 Resistance in a superconductor *J. Appl. Phys.* **33** 748-749

[6]    Meissner W and Ochenfeld R 1933 Ein neuer effekt bei eintritt der supraleitfähigkeit *Naturwissenschaften* **21** 787-788

[7]    London F and London H 1935 The electromagnetic equations of the supraconductor *Proc. Roy. Soc.* **A149** 71-88

[8]    Ginzburg V L and Landau L D 1950 On the theory of superconductivity *Zh. Eksp. Theor. Fiz.* **20** 1064-1082

[9]    Abrikosov A A 1957 On the magnetic properties of superconductors of the second group *Sov. Phys. JETP* **5** 1174-1182

[10]   Tinkham M 1996 *Introduction to Superconductivity* 2nd edition (McGraw-Hill Book Co.)

[11]   Kliener W H, Roth L M and Autler S H 1964 Bulk solution of Ginzburg-Landau equations for type II superconductors: Upper critical field region *Phys. Rev.* **133** A1226-A1227

[12]   Essmann U and Träuble H 1967 The direct observation of individual flux lines in type II superconductors *Phys. Lett.* **24A** 526-527

[13]   Hess H F, Robinson R B, Dynes R C, Valles J M, Jr. and Waszczak J V 1989 Scanning-Tunnelling-Microscope observation of the Abrikosov flux lattice and the density of states near and inside a fluxoid *Phys. Rev. Lett.* **62** 214-216

[14]   Bardeen J, Cooper L N and Schrieffer J R 1957 Theory of Superconductivity *Phys. Rev.* **108** 1175-1204

[15]     Cooper L N 1956 Bound electron pairs in a degenerate fermi gas *Phys. Rev.* **104** 1189-1190

[16]     Maxwell E 1950 Isotope effect in the superconductivity of mercury *Phys. Rev.* **78** 477

[17]     Reynolds C A, Serin B, Wright W H and Nesbitt L B 1950 Superconductivity of isotopes of mercury *Phys. Rev.* **78** 487

[18]     Morel P and Anderson P W 1962 Calculation of the superconducting state parameters with retarded electron-phonon interaction *Phys. Rev.* **125** 1263-1271

[19]     Giaever I and Megerle K 1961 Study of superconductors by electron tunnelling *Phys. Rev.* **122** 1101-1111

[20]     Biondi M A, Forrester A T, Garfunkel M P and Satterthwaite C B 1958 Experimental evidence for an energy gap in superconductors *Rev. Mod. Phys.* **30** 1109-1136

[21]     Gor'kov L P 1959 Microscopic derivation of the Ginzburg-Landau equations in the theory of superconductivity *Sov. Phys. JETP* **36** 1364-1367

[22]     Keys S A and Hampshire D P Testing of Conductors *Handbook of Superconducting Materials* (Institute of Physics) in press

[23]     Tachikawa K 1995 Critical current measurement method for $Nb_3Sn$ multifilamentary composite conductors - Foreward *Cryogenics* **35** S5-S6

[24]     Gould D and Wada H 1995 Introduction *Cryogenics* **35** S7-S8

[25]     Keys S A, Koizumi N and Hampshire D P The strain and temperature scaling law for the critical current density of a jelly-roll $Nb_3Al$ strand in high magnetic fields submitted to *Supercond. Sci. Technol.*

[26]     Wilson M 1998 *Superconducting magnets* (Oxford:Oxford University Press)

[27]     Goodrich L F and Fickett F R 1982 Critical current measurements : a compendium of experimental results *Cryogenics* **22** 225-241

[28]     Grasso G and Flükiger R 1997 Development of rectangular Bi(2223) wires with reduced anisotropy *Supercond. Sci. Technol.* **10** 223-226

[29]     Goodrich L F and Bray S L 1989 Integrity tests for high-$T_c$ and conventional critical-current measurement systems *Adv. Cryo. Eng. (Mater.)* **36A** 43-50

[30]     Herrmann P F 1998 Current leads *Handbook of Applied Superconductivity* ed. B Seeber (Bristol:Institute of Physics) 801-843

[31]    White G K 1987 *Experimental techniques in low-temperature physics* 3rd edition (Oxford:Oxford University Press)

[32]    White G K 1998 Thermal expansion *Handbook of Applied Superconductivity* ed. B Seeber (Bristol:Institute of Physics Publishing) 1107-1119

[33]    Meingast C, Kraut O, Wolf T, Wühl H, Erb A and Müller-Vogt G 1991 Large $a$-$b$ anisotropy of the expansivity anomaly at $T_C$ in untwinned YBa$_2$Cu$_3$O$_{7-d}$ *Phys. Rev. Lett.* **67** 1634-1636

[34]    Clark A F, Fujii G and Ranney M A 1981 The thermal expansion of several materials for superconducting magnets *IEEE Trans. Mag.* **17** 2316-2319

[35]    Okaji M, Nara K, Kato H, Michishita K and Kubo Y 1994 Thermal expansion of some advanced ceramics applicable as specimen holders of high $T_c$ superconductors *Cryogenics* **34** 163-165

[36]    Yamada N, Nara K, Okaji M, Hikata T, Kaneko T and Sadakata N 1998 Effect of thermal cycles on thermal expansion of silver-sheathed Bi2223 tape at 10-310 K *Cryogenics* **38** 397

[37]    Clark A F 1983 Thermal expansion *Materials at low temperatures* ed R P Reed and A F Clark (Ohio:American Society of Metals)

[38]    Pobell F 1992 *Matter and methods at low temperatures* (Berlin:Springer-Verlag)

[39]    Cheggour N and Hampshire D P 2000 A probe for investigating the effect of magnetic field, temperature and strain on transport critical currents in superconducting tapes and wires *Rev. Sci. Instrum.* **71** 4521-4530

[40]    Kirchmayr H, Siddall M B and Smathers D B 1995 Effects of mandrel materials *Cryogenics* **35** S93-S94

[41]    Goodrich L F and Srivastava A N 1995 Thermal contraction of materials used in Nb$_3$Sn critical current measurements *Cryogenics* **35** S29-S32

[42]    Ekin J W 1978 Current transfer in multifilamentary superconductors. I. Theory *J. Appl. Phys.* **49** 3406-3409

[43]    Polak M, Zhang W, Parrell J, Cai X Y, Polyanskii A, Hellstrom E E, Larbalestier D C and Majoros M 1997 Current transfer lengths and the origin of linear components in the voltage-current curves of Ag-sheathed BSCCO components *Supercond. Sci. Technol.* **10** 769-777

[44]    Ekin J W 1989 Offset criterion for determining superconductor critical current *Appl. Phys. Lett.* **55** 905-907

[45]    Goodrich L F, Ekin J W and Fickett F R 1982 Effect of twist pitch on short-sample V-I characteristics of multifilamentary wires *Adv. Cryo. Eng. (Mater.)* **28** 571-580

[46]    Goodrich L F and Srivastava A N 1990 Software techniques to improve data reliability in superconductor and low-resistance measurements *J. Res. Natl. Inst. Stand. Technol.* **95** 575-589

[47]    Goodrich L F 1991 High $T_C$ superconductor voltage-current simulator and the pulse method of measuring critical current *Cryogenics* **31** 720-727

[48]    Goodrich L F, Wiejaczka J A, Srivastava A N, Stauffer T C and Medina L T 1995 USA interlaboratory comparison of superconductor simulator critical current measurements *IEEE Trans. Appl. Supercon.* **5** 548-551

[49]    VAMAS Technical Working Party for Superconducting Materials 1995 Recommended standard method for determination of d.c. critical current of Nb$_3$Sn multifilamentary composite superconductor *Cryogenics* **35** S105-S112

[50]    Clark R G and Jones H 1986 The combination of dilution refrigerators and superconducting/hybrid magnets on physics research *Proc. 11$^{th}$ International Cryogenic Engineering Conference* 414-418

[51]    Willén D W A, Zhu W and Cave J R 1997 Selection of the offset-criterion voltage parameter and its relation to the second differential of a superconductor's voltage-current curve *Institute of Physics Conference Series No.* **158** 1013-1016

[52]    Itoh K, Tanaka Y and Osamura K 1996 Round robin test for the method of critical current measurement of Nb$_3$Sn composite conductors *Proc. 16$^{th}$ International Cryogenic Engineering Conference* 1787-1790

[53]    Baixeras J and Fournet G 1967 Pertes par deplacement de vortex dans un supraconductor de type II non ideal *J. Phys. Chem. Solids* **28** 1541-1547

[54]    Hampshire D P and Jones H 1985 Critical current of a NbTi reference material as a function of field and temperature *Proc. Magnet Technology 9* 531-534

[55]    Cai X Y, Polyanskii A, Li Q, Riley Jr G N and Larbalestier D C 1998 Current-limiting mechanisms in individual filaments extracted from superconducting tapes *Nature* **392** 906-909

[56]   Hampshire D P and Jones H 1987 Analysis of the general structure of the *E-I* characteristic of high current superconductors with particular reference to a Nb-Ti SRM wire *Cryogenics* **27** 608-616

[57]   Hampshire D P and Jones H 1987 A detailed investigation of the *E-J* characteristic and the role of defect motion within the flux-line lattice for high-current-density, high-field superconducting compounds with particular reference to data on $Nb_3Sn$ throughout its entire field-temperature phase space *J. Phys. C. : Solid State Phys.* **20** 3533-3552

[58]   Hampshire D P, Clark A F and Jones H 1989 Flux pinning and scaling laws for superconducting $V_3Ga$ *J. Appl. Phys.* **66** 3160-3167

[59]   Edelman H S and Larbalestier D C 1993 Resistive transitions and the origin of the *n* value in superconductors with a Gaussian critical-current distribution *J. Appl. Phys.* **74** 3312-3315

[60]   Ryan D T 1997 Critical currents of commercial superconductors in the picovolt per metre electric field regime *Ph.D Thesis* University of Oxford

[61]   Warnes W H and Larbalestier D C 1986 Critical current distributions in superconducting composites *Cryogenics* **26** 643-653

[62]   Goodrich L F, Srivastava A N, Yuyama M and Wada H 1993 n-value and second derivative of the superconductor voltage-current characteristic *IEEE Trans. Appl. Supercon.* **3** 1265-1268

[63]   Yamafuji K and Kiss T 1997 Current-voltage characteristics near the glass-liquid transition in high-$T_c$ superconductors *Physica C* **290** 9-22

[64]   Cheggour N and Hampshire D P 1997 The role of vortex melting and inhomogenieties in the transport properties of $Nb_3Sn$ superconducting wires *Institute of Physics Conference Series No.* **158** 1275-1278

[65]   Lide D R 1992 *CRC Handbook of Chemistry and Physics* (Boca Raton:CRC Press)

[66]   Goodrich L F, Bray S L and Stauffer T C 1990 Thermal contraction of fibreglass-epoxy sample holders used for $Nb_3Sn$ critical-current measurements *Adv. Cryo. Eng. (Mater.)* **36** 117-124

[67]     Wiejaczka J A and Goodrich L F 1997 Interlaboratory comparison on high-temperature superconductor critical-current measurements *J. Res. Natl. Inst. Stand. Technol.* **102** 29-52

[68]     Marti F, Grasso G, Huang Y and Flükiger R 1997 High critical current densities in long lengths of mono- and multifilamentary Ag-sheathed Bi(2223) tapes *IEEE Trans. Appl. Supercon.* **7** 2215-2218

[69]     Goodrich L F  Critical-current measurement methods for oxide superconductor tapes and wires. Part 1 : Transport current method *Submitted to Cryogenics*

[70]     Küpfer H and Gey W 1977 Dependence of the critical current density of superconductors on the past history of the magnetic field and the temperature *Phil. Mag.* **36** 859-884

[71]     Goodrich L F, Vecchia D F, Pittman E S, Ekin J W and Clark A F 1984 Critical current measurements on an NbTi superconducting wire standard reference material *NBS Special Publication 260-91*

[72]     Goodrich L F and Srivastava A N 1995 Critical current measurement methods : quantitative evaluation *Cryogenics* **35** S19-S23

[73]     Ogawa R, Kubo Y, Tanaka Y, Itoh K, Ohmatsu K, Kumano T, Sakai S and Osamura K 1996 Standardization of the test method for critical current measurement of Cu/Cu-Ni/Nb-Ti composite superconductors *Proc. 16th International Cryogenic Engineering Conference* 1799-1802

[74]     VAMAS Technical Working Party for Superconducting Materials 1995 Second intercomparison of critical current measurements *Cryogenics* **35** S65-S80

[75]     Kirchmayr H 1995 Effects of specimen bonding materials *Cryogenics* **35** S95-S97

[76]     Sneary A B, Friend C M, Vallier J C and Hampshire D P 1999 Critical current density of Bi-2223/Ag multifilamentary tapes from 4.2 K up to 90 K in magnetic fields up to 23 T *IEEE Trans. Appl. Supercon.* **9** 2585-2588

[77]     International Electrotechnical Commision 1999 Critical current measurement - dc critical current of Ag-sheathed Bi-2212 and Bi-2223 oxide superconductors IEC61788-3

[78]     Goodrich L F and Srivastava A N 1992 Comparison of transport critical current measurement methods *Adv. Cryo. Eng. (Mater.)* **38** 559-566

[79]    Hole C R J 1995 Pulsed magnetic field characterisation of technological high temperature superconductors *Ph.D Thesis* University of Oxford

[80]    Ryan D T, Jones H, Timms W and Killoran N 1997 Critical current measurements at electric fields in the pV m$^{-1}$ regime *IEEE Trans. Appl. Supercon.* **7** 1455-1458

[81]    Friend C M and Hampshire D P 1995 A probe for the measurement of the transport critical current density of superconductors in high magnetic fields and at temperatures between 2 and 150 K *Meas. Sci. Technol.* **6** 98-106

[82]    Frost A J, Jones H and Belenli I 1992 Design, construction and development of an apparatus for the transport-current characterization of high-temperature superconductors at a range of temperatures and magnetic fields *Cryogenics* **32** 1014-1018

[83]    Kuroda T, Murakami Y, Itoh K, Yuyama M, Wada H and Mao D 1998 Temperature dependence of critical current density of $Nb_3Al$ multifilamentary wires fabricated by Nb-tube and its improved processes *Cryogenics* **38** 785-789

[84]    Goodrich L F, Medina L T and Stauffer T C 1997 High critical-current measurements in liquid and gaseous helium *Adv. Cryo. Eng. (Mater.)* **44** 873-880

[85]    Kamata K, Suzuki Y, Moriai H, Inoue K, Itoh K, Takeuchi T, Tachikawa K, Watanabe K, Muto Y, Katagiri K, Noto K and Okada T 1992 Superconducting properties and strain effects in high fields for bronze processed multifilamentary $(Nb,Ti)_3Sn$ wires and composite processed ultrafine $Nb_3Al$ wires *Science Report - Research Institute Tohoku University - Series A - Physics, Chemistry and Metallurgies A* **37** 99-107

[86]    ten Haken B 1994 Strain effects on the critical properties of high-field superconductors *Ph.D Thesis* Technical University of Twente

[87]    Ekin J W 1987 Effect of transverse compressive stress on the critical current and upper critical field of $Nb_3Sn$ *J. Appl. Phys.* **62** 4829-4834

[88]    ten Kate H H J, Weijers H W and van Oort J M 1993 Critical current degradation in $Nb_3Sn$ cables under transverse pressure *IEEE Trans. Appl. Supercon.* **3** 1334-1337

[89]    Jakob B, Pasztor G, Bona M and Asner A 1991 Reduced sensitivity of $Nb_3Sn$ epoxy-impregnated cable to transverse stress *Cryogenics* **31** 390-391

[90]   Ochiai O, Osamura K and Watanabe K 1993 Estimation of strength distribution of Nb$_3$Sn in multifilamentary composite wire from change in superconducting current due to preloading *J. Appl. Phys.* **74** 440-445

[91]   Keys S A, Cheggour N and Hampshire D P 1999 The effect of hot isostatic pressing on the strain tolerance of the critical current density found in modified jelly roll Nb$_3$Sn wires *IEEE Trans. Appl. Supercon.* **9** 1447-1450

[92]   McDonald W K, Curtis C W, Scanlan R M, Larbalestier D C, Marken K and Smathers D B 1983 Manufacture and evaluation of Nb$_3$Sn conductors fabricated by the MJR method *IEEE Trans. Mag.* **19** 1124-1127

[93]   Fukutsuka T, Horiuchi T, Monju Y, Tatara I, Maeda Y and Moritoki M 1984 Effects of hot isostatic pressing on the superconducting properties of Nb$_3$Sn multifilamentary wires *Adv. Cryo. Eng.* **30** 891-898

[94]   Nourbakhsh S, Hascicek Y S, Goringe M J and Martin J W 1982 On the presence of voids in bronze-route multi-filamentary Nb$_3$Sn superconducting wires *J. Mater. Sci.* **17** 3204-3210

[95]   Kramer E J 1973 Scaling laws for flux pinning in hard superconductors *J. Appl. Phys.* **44** 1360-1370

[96]   Fietz W A and Webb W W 1969 Hysteresis in superconducting alloys - temperature and field dependence of dislocation pinning in niobium alloys *Phys. Rev.* **178** 657-667

[97]   ten Haken B, Godeke A and ten Kate H H J 1999 The strain dependence of the critical properties of Nb$_3$Sn conductors *J. Appl. Phys.* **85** 3247-3253

[98]   Godeke A, Krooshoop H J G, Knoopers H G, ten Haken B and ten Kate H H J 2001 Experimental verification of the temperature and strain dependence of the critical properties in Nb$_3$Sn wires *IEEE Trans. Appl. Supercon.* **11** 1526-1529

[99]   Ekin J W 1980 Strain scaling law for flux pinning in practical superconductors. Part 1 : Basic relationship and application to Nb$_3$Sn conductors *Cryogenics* **20** 611-624

[100]   McKinnell J C, Smathers D B, Siddall M B and O'Larey P M 1995 Improved superconducting critical current density in modified jelly roll Nb$_3$Sn by the application of niobium (Nb) diffusion barriers *IEEE Trans. Appl. Supercon.* **5** 1768-1772

[101]   Katagiri K, Okada T, Walters C R and Ekin J W 1995 Effects of stress/strain *Cryogenics* **35** S85-S88

[102]  Iijima Y, Kikuchi A and Inoue K 2000 New $Nb_3Al$-based A15 multifilamentary wires with high $J_C$ in high fields *Cryogenics* **40** 345-348

[103]  Kikuchi A, Iijima Y, Inoue K, Kosuge M and Itoh K 2001 $Nb_3(Al,Ge)$ multifilamentary wires made by the rapidly-heating/quenching process *IEEE Trans. Appl. Supercon.* **11** 3984-3987

[104]  Takeuchi T 2000 $Nb_3Al$ conductors for high field applications *Supercond. Sci. Technol.* **13** R101-119

[105]  Takeuchi T, Banno N, Fukuzaki T and Wada H 2000 Large improvement in high-field critical current densities of $Nb_3Al$ conductors by the transformation-heat-based-up-quenching method *Supercond. Sci. Technol.* **13** L11-L14

[106]  Glowacki B A 1999 Niobium aluminide as a source of high-current superconductors *Intermetallics* **7** 117-140

[107]  Kuroda T, Wada H, Iijima Y and Inoue K 1989 Strain effects on superconducting properties in $Nb_3Al$ multifilamentary wires *J. Appl. Phys.* **65** 4445-4447

[108]  Cheggour N and Hampshire D P The strain and temperature scaling law for the critical current density of bronze-route $Nb_3Sn$ in high magnetic fields *submitted to Cryogenics*

[109]  Zeritis D, Ando T, Takahashi Y, Nishi M, Nakajima H and Shimamoto S 1990 Transverse stress effect on the critical current of jelly-roll multifilamentary $Nb_3Al$ wires *Appl. Phys. Lett.* **57** 506-507

[110]  Specking W, Ando T, Tsuji H, Mikumo A and Yamada Y 1996 Effect of static and cyclic strain on $J_C$ of $Nb_3Al$ CIC conductors: A comparison with $Nb_3Sn$ *Proc. 16th International Cryogenic Engineering Conference* 1661-1664

[111]  Takeuchi T, Iijima Y, Inoue K, Wada H, ten Haken B, ten Kate H H J, Fukuda K, Iwaki G, Sakai S and Moriai H 1997 Strain effects in $Nb_3Al$ multifilamentary conductors prepared by phase transformation from bcc supersaturated-solid solution *Appl. Phys. Lett.* **71** 122-124

[112]  Weber H W 1998 Radiation effects on superconducting fusion magnet components *Handbook of Applied Superconductivity* ed. B Seeber (Bristol:Institute of Physics) 573-600

[113]   Yamada Y, Ayai N, Mikumo A, Ito M, Hayashi K, Takahashi K, Sato K, Koizumi N, Ando T, Matsui K, Sugimoto M, Tsuji H and Okuno K 1999 Development of $Nb_3Al$ superconductors for International Thermonuclear Experimental Reactor (ITER) *Cryogenics* **39** 115-122

[114]   Koizumi N, Ando T, Sugimoto M, Takahashi Y, Tsuji H, Shimamoto S, Yamada Y, Mikumo A and Ayai N 1998 Development of a 13-T and 40-kA $Nb_3Al$ conductor for toroidal coils of fusion reactors *Fusion Eng. Des.* **41** 277-281

[115]   Ekin J W, Fickett F R and Clark A F 1975 Effect of stress on the critical current of NbTi multifilamentary composite wire *Adv. Cryo. Eng.* **22** 449-452

[116]   Ekin J W 1977 Mechanisms for critical-current degradation in NbTi and $Nb_3Sn$ multifilamentary wires *IEEE Trans. Mag.* **13** 127-130

[117]   Ekin J W, Yamashita T and Hamasaki K 1985 Effect of uniaxial strain on the critical current and critical field of Chevrel phase $PbMo_6S_8$ superconductors *IEEE Trans. Mag.* **21** 474-477

[118]   Goldacker W, Specking W, Weiss F, Rimikis G and Flükiger R 1989 Influence of transverse compressive and axial tensile stress on the superconductivity of $PbMo_6S_8$ and $SnMo_6S_8$ wires *Cryogenics* **29** 955-960

[119]   Thieme C L H, Fleshler S, Buczek D M, Jowett M, Fritzmeier L G, Arendt P N, Foltyn S R, Coulter J Y and Willis J O 1999 Axial strain dependence at 77 K of the critical current of thick YBaCuO films on Ni-Alloy substrates with IBAD buffer layers *IEEE Trans. Appl. Supercon.* **9** 1494-1497

[120]   Ekin J W, Finnemore D K, Li Q, Tenbrink J and Carter W 1992 Effect of axial strain on the critical current of Ag-sheathed Bi-based superconductors in magnetic fields up to 25 T *Appl. Phys. Lett.* **61** 858-860

[121]   Goldacker W, Keßler J, Ullmann B, Mossang E and Rikel M 1995 Axial tensile, transverse compressive and bending strain experiments in Bi(2223)/AgMg single core tapes *IEEE Trans. Appl. Supercon.* **5** 1834-1837

[122]   Richens P E, Jones H, van Cleemput M and Hampshire D P 1997 Strain dependence of critical currents in commercial high temperature superconductors *IEEE Trans. Appl. Supercon.* **7** 1315-1318

[123]   Hamid H A and Hampshire D P 1998 Critical current density of superconductors as a function of strain in high magnetic fields *Cryogenics* **38** 1007-1015

[124]  Kroeger D M, Easton D S, DasGupta A, Koch C C and Scarbrough J O 1980 The effect of strain upon the scaling law for flux pinning in bronze process $Nb_3Sn$ *J. Appl. Phys.* **51** 2184-2192

[125]  Cheggour N and Hampshire D P 1999 Unifying the strain and temperature scaling laws for the pinning force density in superconducting niobium-tin multifilamentary wires *J. Appl. Phys.* **86** 552-555

[126]  Ando T, Nunoya Y, Koizumi N, Sugimoto M, Tsuji H, Sato K and Yamada Y 1997 Dependence of critical current density on temperature and magnetic field in multifilamentary $Nb_3Al$ strands made by the jerry (sic.) roll process *IEEE Trans. Appl. Supercon.* **7** 1568-1571

[127]  Banno N, Takeuchi T, Tagawa K, Itoh K, Wada H and Nakagawa K 2000 Field and temperature dependencies of critical current density in rapid quenched and transformed $Nb_3Al$ multifilamentary conductors *IEEE Trans. Appl. Supercon.* **10** 1026-1029

[128]  Hampshire D P, Jones H and Mitchell E W J 1985 An in depth characterization of $(NbTa)_3Sn$ filamentary superconductors *IEEE Trans. Mag.* **21** 289-292

[129]  Itoh K, Kuroda T, Yuyama M, Iijima Y, Wada H, Murakami Y and Mao D 1997 Field and tempertaure dependencies of critical current in direct-heated Nb-tube processed $Nb_3Al$ wires *IEEE Trans. Appl. Supercon.* **7** 1576-1579

[130]  Mao D, Itoh K, Kuroda T, Yuyama M, Wada H and Murakami Y 1998 Magnetization measurement for a nearly stoichiometric $Nb_3Al$ wire *Physica C* **301** 272-276

[131]  Walters C R, Davidson I M and Tuck G E 1986 Long sample high sensitivity critical current measurements under strain *Cryogenics* **26** 406-412

[132]  Specking W, Nyilas A, Klemm M, Kling A and Flükiger R 1989 The effect of axial stresses on $I_C$ of subsize net $Nb_3Sn$ conductors *Proc. 11th Conference on Magnet Technology* 1009-1014

[133]  Ayai N, Yamada N, Mikumo A, Ito M, Ohmatsu K, Sato K, Koizumi N, Ando T, Matsui K, Sugimoto M, Tsuji H and Okuno K 1999 Development of $Nb_3Al$ superconductors for ITER *IEEE Trans. Appl. Supercon.* **9** 2688-2691

[134]  Taylor D M J, Keys S A and Hampshire D P *E-J* characteristics and *n*-values of a niobium-tin superconducting wire as a function of magnetic field, temperature and strain *submitted to Physica C*

[135]  Seeber B 2001 Private communication

[136]  Mathu F and Meijer H C 1982 Some electrical feedthroughs to be used at low temperatures *Cryogenics* **22** 428

[137]  Brandt B L, Liu D W and Rubin L G 1999 Low temperature thermometry in high magnetic fields. VII. Cernox™ sensors to 32 T *Rev. Sci. Instrum.* **70** 104-110

[138]  Ramsbottom H D, Ali S and Hampshire D P 1996 Response of a new ceramic-oxynitride (Cernox) resistance temperature sensor in high magnetic fields *Cryogenics* **36** 61-63

[139]  Heine G and Lang W 1998 Magnetoresistance of the new ceramic "Cernox" thermometer from 4.2 K to 300 K in magnetic fields up to 13 T *Cryogenics* **38** 377-379

[140]  Koizumi N 2001 Private communication

[141]  ten Haken B, Godeke A, ten Kate H H J and Specking W 1996 The critical current of $Nb_3Sn$ wires for ITER as a function of the axial tension and compression *IEEE Trans. Mag.* **32** 2739-2742

[142]  Taylor D M J and Hampshire D P The scaling law for the field, temperature and strain dependence of the current density in $Nb_3Sn$ wires *in progress*

[143]  Campbell A M and Evetts J E 1972 Flux vortices and transport currents in type II superconductors *Adv. Phys.* **21** 199-428

[144]  Dew-Hughes D 1974 Flux pinning mechanisms in type II superconductors *Phil. Mag.* **30** 293-305

[145]  Cicchelli O, Bottura L, Gilson P and Spadoni M 1995 Alternative strand material for the toroidal field coils of the ITER magnetic system: Assessment of $Nb_3Al$ *IEEE Trans. Appl. Supercon.* **5** 901-904

[146]  Godeke A, ten Haken B and ten Kate H H J The deviatoric strain description of the critical properties of $Nb_3Sn$ conductors *submitted to Physica C*

[147]  Zheng D N, Ramsbottom H D and Hampshire D P 1995 Reversible and irreversible magnetisation of the Chevrel-phase superconductor $PbMo_6S_8$ *Phys. Rev. B* **52** 12931-12938

[148] Ramsbottom H D and Hampshire D P 1999 Flux penetration measurements and the harmonic magnetic response of hot isostatically pressed $(Pb,Gd)Mo_6S_8$ *J. Appl. Phys.* **85** 3732-3739

[149] Kuroda T, Itoh K, Wada H and Togano K 2000 A study on the relation between the strain scaling law and the temperature scaling law on flux pinning in $Nb_3Sn$ superconducting wires *Cryogenics* **40** 287-294

[150] Jeffery A 1992 *Mathematics for engineers and scientists* 4th edition (London:Chapman and Hall)

[151] Friend C M 1994 Transport critical current density measurements on high and low temperature superconductors in magnetic fields up to 15 T *Ph.D Thesis* University of Durham

[152] Ohtsuka T and Takano N 1967 Magnetocaloric effect and the upper critical field of superconducting niobium *J. Phys. Soc. Japan* **23** 983-998

[153] Willens R H, Geballe T H, Gossard A C, Maita J P, Menth A, Hull G W, Jr. and Soden R R 1969 Superconductivity of $Nb_3Al$ *Solid State Commun.* **7** 837-841

[154] Knapp G S, Bader S D and Fisk Z 1976 Phonon properties of *A*-15 superconductors obtained from heat capacity measurements *Phys. Rev. B* **13** 3783-3789

[155] Kwo J, Orlando T P and Beasley M R 1981 Microscopic superconducting parameters of $Nb_3Al$: Importance of the band density of states *Phys. Rev. B* **24** 2506-2514

[156] Hampshire D P 1998 A barrier to increasing the critical current density of bulk untextured polycrystalline superconductors in high magnetic fields *Physica C* **296** 153-166

[157] Lim K C, Thompson J D and Webb G W 1983 Electronic density of states and $T_C$ in $Nb_3Sn$ under pressure *Phys. Rev. B* **27** 2781-2787

[158] Ekin J W and Bray S L 1996 High compressive axial strain effect on the critical current and field of $Nb_3Sn$ superconductor wire *Adv. Cryo. Eng.* **42** 1407-1414

[159] ten Haken B, Godeke A and ten Kate H H J 1995 The influence of compressive and tensile axial strain on the critical properties $Nb_3Sn$ conductors *IEEE Trans. Appl. Supercon.* **5** 1909-1912

[160] Welch D O 1980 Alteration of the superconducting properties of A15 compounds and elementary composite superconductors by nonhydrostatic elastic strain *Adv. Cryo. Eng.* **26** 48-65

[161] Wördenweber R 1999 Mechanism of vortex motion in high-temperature superconductors *Rep. Prog. Phys.* **62** 187-236

[162] Cheggour N, Decroux M, Fischer Ø and Hampshire D P 1998 Irreversibility line and granularity in Chevrel phase superconducting wires *J. Appl. Phys.* **84** 2181-2183

[163] Ekin J W 1981 Strain scaling law for flux pinning in NbTi, Nb₃Sn, Nb-Hf/Cu-Sn-Ga, V₃Ga and Nb₃Ge *IEEE Trans. Mag.* **17** 658-661

[164] Ekin J W 1984 Strain effects in superconducting compounds *Adv. Cryo. Eng.* **30** 823-836

[165] Sun J Z, Eom C B, Lairson B, Bravman J C and Geballe T H 1991 Magnetic relaxation, current-voltage characteristics, and possible dissipation mechanisms for high-$T_C$ superconducting films of Y-Ba-Cu-O *Phys. Rev. B* **43** 3002-3008

[166] Yeshurun Y and Malozemoff A P 1988 Giant flux creep and irreversibility in an Y-Ba-Cu-O crystal: An alternative to the superconducting-glass model *Phys. Rev. Lett.* **60** 2202-2205

[167] Zallen R 1983 *The physics of amorphous solids* (New York:Wiley)

[168] Lorenz C D and Ziff R M 2001 Precise determination of the critical percolation threshold for the three-dimensional "Swiss cheese" model using a growth algorithm *J. Chem. Phys.* **114** 3659-3661

[169] Gingold D B and Lobb C J 1990 Percolative conduction in three dimensions *Phys. Rev. B* **42** 8220-8224

[170] Lobb C J, Tinkham M and Skocpol W J 1978 Percolation in inhomogeneous superconducting composite wires *Solid State Commun.* **27** 1273-1275

[171] Harris D C, Herbert S T, Stroud D and Garland J C 1991 Effect of random disorder on the critical behaviour of Josephson junction arrays *Phys. Rev. Lett.* **67** 3606-3609

[172] Schauer W and Schelb W 1981 Improvement of Nb₃Sn high field critical current by a two stage reaction *IEEE Trans. Mag.* **17** 374-377

[173] Kramer E J 1975 Microstructure - critical current relationships in hard superconductors *Electron. Mater.* **4** 839-880

[174]   Osborne K E and Kramer E J 1974 The influence of plastic deformation on the peak effect in a type II superconductor *Phil. Mag.* **29** 685-694

[175]   Enstrom R E and Appert J R 1973 Preparation, microstructure and high-field superconducting properties of $Nb_3Sn$ doped with group-III, -IV, -V, and -VI elements *J. Appl. Phys.* **43** 1915-1923

[176]   Bonney L A, Willis T C and Larbalestier D C 1995 Dependence of critical current density on microstructure in the $SnMo_6S_8$ chevrel phase superconductor *J. Appl. Phys.* **77** 6377-6387

# Appendix 1

# Publications

1.  The strain and temperature scaling law for the critical current density of a jelly-roll $Nb_3Al$ strand in high magnetic fields

    Keys S A, Koizumi N and Hampshire D P

    *Submitted for publication in Superconductor Science and Technology*

2.  Characterisation of $Nb_3Sn$ and $Nb_3Al$ strands for model coils

    Hampshire D P, Taylor D M J, Foley P and Keys S A

    Technical report - *Report No. : Durham SC06/01*, June 2001

3.  Testing of Conductors

    Keys S A and Hampshire D P

    *Handbook of Superconducting Materials* edited by D Cardwell and D Ginley, Institute of Physics Publishing, Bristol

    Accepted for publication September 1999

4.  The effect of hot isostatic pressing on the strain tolerance of the critical current density found in modified jelly roll $Nb_3Sn$ wires

    Keys S A, Cheggour N and Hampshire D P

    *IEEE Transactions on Applied Superconductivity*, **9**, 1447-1450 (1999)

# Appendix 2

## Conferences and Courses

### Conferences Attended

| April 2001 | University of Birmingham | Superconductivity Meeting |
| December 1999 | University of Leicester | CMMP'99 |
| December 1998 | UMIST | CMMP '98 |
| September 1998 | Palm Desert, California | ASC '98 |
| December 1997 | University of Exeter | CMMP '97 |

### Courses Attended

| June 1999 | Brunel University (Uxbridge) | CRAC Research Councils' Graduate Schools Program |
| April 1998 | University of Durham | Mechanical Workshop Course |
| November 1997 | University of Aston | Low Temperature Techniques |

# Appendix 3

## Computer Programs

Most measurements presented in this thesis were computer controlled so that the data could be stored digitally. The programs used to control the experiments were written in ASYST v.4 (Keithley). The main programs used are detailed below along with a brief description summarising their operation. Loading the underlined program loads the other components.

### *V-I* based programs

120trace.sk1, 120trace.var

> *V-I* characteristics measured up to 120 A using the Oxford Instruments IPS (IPS-120) power supply at a single field and temperature. No temperature control is written into this program.

120field.sk1, 120field.var

> *V-I* characteristics measured up to 120 A using the IPS-120 at different fields. There is no temperature control written into this program.

500trace.sk1, 120trace.var

> *V-I* characteristics measured up to 500 A using the in-house 500 A power supply at a single field and temperature. No temperature control is written into this program. The IPS-120 is used to control the 500 A supply.

500field.sk1, 120field.var

> *V-I* characteristics measured up to 500 A using in-house 500 A power supply at different fields. There is no temperature control written into this program. The IPS-120 is used to control the 500 A supply.

<u>120btrun.sk2</u>, 120field.vr2, cx_cal_e.dat, cx_cal_e.run, 120field.sk2, 120fiel2.sk2

> *V-I* characteristics measured up to 120 A using the IPS-120 at different fields.
> The temperature is actively controlled using a Cernox thermometer as described in
> chapter 5.

## Resistivity based programs

<u>res_brun.vti</u>, res_bvar.vti, cx_cal_e.dat, cx_cal_e.run, res_b1.vti, res_b2.vti, res_b3.vti,
res_b4.vti, res_b5.vti, res_b6.vti, res_b_go.vti

> Resistivity as a function of field at fixed temperature. Three separate excitation
> currents are used to measure the resistivity. The temperature is actively controlled
> using a Cernox thermometer as described in chapter 5.

<u>resisrun.sak</u>, resisvar.sak, cx_cal_e.var, cx_cal_e.dat, cx_cal_e.run, resist1.sak,
resist2.sak, resist3.sak, resist4a.sak, resist4b.sak, resist4c.sak, resistgo.sak

> Resistivity as a function of temperature at fixed field. Three separate excitation
> currents are used to measure the resistivity. The temperature is actively controlled
> using a Cernox thermometer as described in chapter 5.

<u>cxcalrun.vti</u>, cxcalvar.vti, cxcal1.vti, cxcal2.vti, cxcal3.vti, cxcal4.vti, cxcal5.vti,
cxcal6.vti, cxcalgo.vti

> Used for calibrating Cernox thermometer in the VTI. Allows measurement of
> various voltmeters and a capacitance thermometer. There is no temperature
> control associated with this program, as the VTI was controlled manually.